Hybrid particle-in-cell simulations of relativistic plasmas

Inaugural-Dissertation

zur Erlangung des Doktorgrades
der Mathematisch-Naturwissenschaftlichen Fakultät
der Heinrich-Heine-Universität Düsseldorf

vorgelegt von

Tobias Tückmantel
aus Haan

Juli 2012

Aus dem Institut für Theoretische Physik I
der Heinrich-Heine-Universität Düsseldorf

Gedruckt mit der Genehmigung
der Mathematisch-Naturwissenschaftlichen Fakultät der
Heinrich-Heine-Universität Düsseldorf

Referent: Prof. Dr. Alexander Pukhov
Koreferent: Prof. Dr. Achim Schädle

Tag der mündlichen Prüfung: 12.10.2012

Contents

CHAPTER 1

Introduction

With the beginning of the 21^{st} century, modern physics is split into a great many, highly specialized disciplines. Each of them comes with a variety of thrilling questions, fascinating discoveries and technological promises. Solid state physics has provided great insight into the mechanisms of cristalline many-body systems, and given modern society the gift of tremendous computing power. Plasma physics studies the inner stucture of stars, illuminates the streets at night and upholds the half-century old dream of civil nuclear fusion, the sun on earth. Atomic and molecular physics are interwoven with modern chemistry and have had such remarkable outcomes as Bose-Einstein condensation or the laser. The list could be extended for many pages, and there are unnumbered potential applications within the grasp of a lifetime.

From this point of view, high energy or particle physics was always like a faint glimpse into the distant future. Exploring the very foundation of all matter, its potent experimental approach is the particle accelerator. Per-particle energies far ahead of any other physical field have always been the only way to expand the horizon of the knowledge about matter's inner structure. The Large Hadron Collider located at CERN is the most prominent particle accelerator experiment. Here, interdisciplinary knowledge and cutting-edge technology manifest in the largest machine ever built by man. In a 27 km circumference underground ring, protons or lead ions are pushed to up to 7 TeV energy before collision. Particle accelerators are also present in many smaller applications, e.g. material testing or nuclide generation for medical applications.

Unfortunately, the electro-magnetic accelerator concept comes with a number of problems. When built as a linear accelerator without curvature, the travelling distance and therefore the final energy of the particles is limited. When designed as a ring, it is a lot more economic. But as particles with curved trajectories lose energy through synchrotron radiation, there is an upper boundary to their final energy. On the other hand, materials interacting with high fields eventually become destroyed by break-down and ionization, which limits the accelerating fields to a few MV/m. It is evident that, to keep up with the need for ever increasing particle energies, accelerators must soon enter a new technological stage. Additionally, devices for medical or industrial applications are expensive, which gives rise to the question for a cheaper alternative.

A very interesting new accelerator concept comes from plasma physics. In a quasineutral plasma, a displacement of electrons against the heavier ion background leads to formation of strong electric fields. While the (at least 1836 times heavier) ions do not move much, the electrons are drawn back, exciting new fields. This

effect is known as plasma oscillation, and it happens with the plasma frequency

$$\omega_p = \sqrt{\frac{4\pi e^2 n_e}{m_e}}.$$

This equation is given in cgs units, with the electron number density n_e, elementary charge e and electron mass m_e. There is another process closely related to plasma oscillations. If the electron displacement is caused by some driver moving with a velocity close to c, local oscillations are excited along its path. The longitudinal electric field takes on the structure of a travelling wave; this effect is called a wake field. What makes it that interesting is the fact that its phases travel with about the driver's speed, and that amplitudes of 100 GV/m can be obtained. This means it can be used as an accelerator by injecting other particles into it. [**1, 2, 3, 4, 5, 6, 7**] Since its electric field is orders of magnitude higher, it can be far more efficient than conventional electromagnetic accelerator devices. The drivers for wake fields can be relativistic laser pulses, electron or proton bunches [**8, 9, 10**] as short as the plasma wave length

$$\lambda_p = \frac{2\pi c}{\omega}.$$

Particle bunches excite wake fields directly through their surrounding fields. Laser pulses with relativistic intensities

$$a_0 = \frac{eA}{m_e c} > 1$$

push the background electrons via ponderomotive forces. By now, this technique is regularly used to accelerate electrons to GeV energies [**11, 6, 7, 12, 13, 14, 2**].

The Laser wake-field accelerator (LWFA) concept is an active field of research. Since the invention of the Chirped Pulse Amplification [**15**], high power laser systems are present in many research facilities. They reach intensities $> 10^{20}\mathrm{W/cm^2}$, and pulse lengths in the range of a few femtoseconds. These systems can be built with relatively small sizes, often filling just a room. Hence, they promise to become an efficient alternative to the bulky and expensive electromagnetic accelerators.

Since its first proposal [**1**], the LWFA scheme has seen great progress: Electrons can be externally injected into the wake [**16**], or even become self-injected due to wave-breaking [**12**]. With even higher intensities ($a_0 \gtrsim 5$), the wake field enters a new regime, where a region behind the pulse becomes entirely free of electrons. This situation is called the bubble regime [**11**], involving heavy wave-breaking and the possibility of strong self-injection. Additionally, the efficiency of the energy transfer from the driver to the accelerated particles, known as the transformer ratio [**17**], has been investigated.

A main drawback of laser wake-field accelerators is the fact that dispersion makes the pulse slightly slower than c. It causes the injected particles to eventually leave the accelerating field phase of the wake, and become decelerated instead. This limiting effect is known as dephasing; it puts an upper bound to the acceleration length.

Particle beams as drivers do not suffer from dispersion, but also steadily lose their energy because of the wake field. Because of this transformer ratio limit[**4, 18**], the accelerated particles cannot gain more energy than the driver initially had. Since protons can be pushed towards high energies easier than electrons, proton driven plasma wake field acceleration can be used to accelerate electrons [**3, 19, 20**].

Such an experiment is currently being built up at CERN, using 450 GeV proton bunches from the Super Proton Synchrotron (SPS) in order to drive the wake field.

However, there is a big challenge, which also greatly dominates the research presented in this thesis: Even for thin plasmas of density $7 \cdot 10^{14}\mathrm{cm}^{-3}$, the proton bunches achievable today are much longer than a plasma wave length $\lambda_p = 1.2\mathrm{mm}$. A way out of this problem is self-modulation. In the 80's of the twentieth century, the problem for laser wake field acceleration was very much the same. Here, the self-modulation of long laser pulses was utilized to resonantly drive wake fields[**21**]. A long proton beam propagating through plasma is also subject to the self-modulation instability [**22, 23, 19**]. It works as follows: Even a slight wake field will impose a force on the protons, slowly shifting them aside. Because of this, the proton beam becomes longitudinally modulated, driving the wake field even stronger. This effect can be utilized to make proton driven wake field acceleration feasible; it has the easily recognizable name self-modulated proton driven plasma wake field acceleration (SM-PDPWFA)[**24**]. The main part of this thesis will focus on the SM-PDPWFA effect and the challenges in simulating it. To avoid the dephasing problem, it is crucial to know - and control - the velocity of the accelerating phases of the wake field. It turns out that this phase velocity is strongly connected to the growth rate of the instability. Also, it can be modified by introducing a slight longitudinal gradient into the plasma density. However, reliable simulations of this regime are very difficult.

As most other physical fields, modern plasma physics relies heavily on computer simulations. Between analytical theories with their limited area of validity, and experiments with their few accessible measurable quantities, they fill the gap, giving access to every quantity at all times. With the advent of TFlop/s scale parallel computers commonly available, they can handle problems of fluid dynamics, quantum physics, many-body systems, and even molecular biology and chemistry. The most important simulation concept for non-equilibrium plasmas (and wake fields in particular) is the Particle-in-cell (PIC) method (see e.g. [**25, 26**]). Going one step further than hydrodynamics approaches, it constitutes a way to solve Vlasov's equation

$$\frac{\partial}{\partial t} f + \mathbf{v} \nabla_x f + \frac{q}{m} \left(\mathbf{E} + \mathbf{v} \times \mathbf{B} \right) \nabla_v f = 0$$

directly. This equation describes the temporal evolution of the phase space density of a particle species in the collisionless limit. While the simplified fluid equations reduce the dimension of the problem, failing e.g. in modeling wave-breaking, the Vlasov equation works on the full six-dimensional phase space. The problem of this partial differential equation is that maintaining a 6D grid with reasonable resolution is hardly possible even on the largest supercomputers available. Here, the PIC algorithm provides an elegant way to greatly reduce the computational effort. Instead of the 6D mesh, a large number of so-called macroparticles is defined which represent the plasma. These particles are moved by solving kinetic equations of motion for their center of mass. At the same moment, Maxwell's equations are solved on a 3D grid. A moving particle acts back on the fields by creating currents on the cell boundaries, and the momentum of a particle is updated according to Lorentz forces. This simulation concept has been implemented in the form of a great many codes like OSIRIS[**27**], OOPIC[**28**], WARP[**29**], VORPAL[**30**], LSP[**31**], VLPL[**32**] and

many more. It is successfully used for computations in laser-plasma and plasma-plasma interaction, magnetic and inertial confinement fusion, particle accelerator and electron gun design (e.g. [**33**]), just to name a few. This work is mainly based on the particle-in-cell method and its variations, namely the Virtual Laser Plasma Laboratory (VLPL) code.

However, the numerical error of PIC can significantly influence the quality of simulations: There is numerical dispersion of electromagnetic waves, artificial noise due to sub-optimal phase space sampling, and diffusion effects because of interpolation errors. Also, as most PIC codes use explicit time integrators, their time steps most obey a Courant-Friedrichs-Levy (CFL) stability condition, which can cause problems e.g. in the presence of high plasma densities. PIC simulations of the abovementioned SM-PDPWFA effect are particularly difficult, because the length of the driver corresponds to 200-500 plasma wave lengths. Repeated grid-to-particle interpolations cause a continuous loss of information. This manifests as numerical dispersion, unphysical broadening of the wake and damping. In its early stage, the self-modulation instability is very sensitive, and these problems of PIC can falsify the result entirely. On the other hand, methods of computational fluid dynamics can be designed to avoid these issues.

The most auspicious solution is to combine the best of both worlds, by implementing a PIC-hydrodynamic hybrid code[**34, 31, 35**]. Here, a plasma can be represented by two means: First, as PIC macroparticles, with all the known benefits and shortcomings. Second, as a fluid, storing the relevant variables on a grid and using the computational methods for hyperbolic differential equations. At the expense of physical generality, fluid schemes are usually much faster and more accurate.

Within this work, two hybrid code concepts are presented. The first one uses a linearized fluid model, which models local plasma oscillations. It employs a special time integration scheme, a so-called mollified impulse method exponential integrator. This integrator is unconditionally stable regardless of the plasma frequency, and can be used for the simulation of high density plasmas. It is demonstrated that it is well suited e.g. for the Target Normal Sheath Acceleration (TNSA) effect[**36**]. The latter is a promising idea for laser-based proton acceleration: A highly intense laser pulse is incident onto a specially prepared foil, heats electrons from the front surface and makes them propagate through that foil. Leaving the back surface, they create strong electric fields, which then dissolve protons from the surface. Since the foil has a relatively high density, the stability condition

$$\Delta t \leq \frac{2}{\omega_p}$$

causes unnessecary computational load, and can be avoided with the exponential integrator.

The second hybrid module uses a non-linear cold-fluid model, whose geometry and spatial schemes have been designed for lossless wake field modeling. After explaining the technical difficulties (sec. 6.4, [**37**]) its implementation details will be presented, and its correctness is demonstrated using numerical analysis and a variety of physical examples. This hybrid module gives VLPL the capability to accurately simulate the SM-PDPWFA effect. Multiple large-scale hybrid SM-PDPWFA simulations have been carried out, and given insights into the spatio-temporal evolution of the wake phase velocity. We show that the phase velocity

develops in a way beneficial to particle injection, and how it can even be optimized. Also, we demonstrate that electron side injection into the wake works very robustly and efficiently.

This work can be viewed as consisting of one medium-sized and one large-sized project. The first one is the development, implementation, and benchmark of the exponential integrator-based linear hybrid module (chap.5). The second, largest project consists of the design, implementation and testing of the non-linear H-VLPL3D hybrid module (shown in chap.6); afterwards, this code is used for the investigation of the self-modulated proton driven wake field acceleration (chap.7).

CHAPTER 2

Principles of plasma physics

In this chapter, the basic equations of classical, ideal, relativistic plasma dynamics are derived and explained. We will briefly show the six-dimensional Vlasov equation in an intuitive manner, and depict how its integral moments lead to the well-known fluid equations. Both sets of equations will be of fundamental importance later in this thesis.

2.1. The Vlasov equation

For a wide range of setups, collisions between particles can be neglected, so one can derive a macroscopical plasma model.

For a particle species j, let $f_j : \Gamma \to \mathbb{R}$ be its phase space distribution function, that is to say, the particle density defined on the 6-dimensional (in 3D geometry) vector space $\Gamma := \{(\mathbf{x}, \mathbf{v}) : \mathbf{x} \in \mathbb{R}^3, \mathbf{v} \in \mathbb{R}^3\}$ consisting of positions and momenta. We denote the per-particle mass with m_j, and the per-particle charge with q_j. Although the time evolution for this distribution function can be derived from kinetic equations of motion, we will follow a more intuitive approach here.

Without taking into account effects like ionisation or recombination, we can assume that the total number of particles

$$N_j(t) := \int_\Gamma f_j(\mathbf{x}, \mathbf{v}, t) d^3x \, d^3v$$

is a constant. Thus, there has to be a conservation law, a phase space continuity equation, governing the time behaviour of f_j. Conservation laws always take the form

$$\frac{\partial}{\partial t} U + \nabla \cdot (F(U)) = 0,$$

with $U : \Omega \times [t_0, t_1] \to \mathbb{R}^n$ and $F : \mathbb{R}^n \to \mathbb{R}^{d \times n}$ being a flux vector field. For the case of the function f_j, it reads

$$\frac{\partial}{\partial t} f_j + \nabla_x \cdot (F_x(f_j)) + \nabla_v \cdot (F_v(f_j)) = 0. \tag{2.1.1}$$

Now, needing an expression for the fluxes F_x and F_v, we consider the equations of motion for a single particle, which read

$$\begin{aligned} \dot{\mathbf{x}} &= \mathbf{v} \\ \dot{\mathbf{v}} &= \frac{q_j}{m_j} (\mathbf{E} + \mathbf{v} \times \mathbf{B}) . \end{aligned} \tag{2.1.2}$$

This means that the material is advected by equation (2.1.1). The velocity field for this advection process must be $\mathbf{v}$ for the spatial directions and $(q_j/m_j)(\mathbf{E}+\mathbf{v}\times\mathbf{B})$ for the momentum directions, see figure 2.1.1.

So, the flux fields can be written as follows:

$$F_x(f_j) = \mathbf{v} f_j, \tag{2.1.3}$$

$$F_v(f_j) = \frac{q_j}{m_j}(\mathbf{E}+\mathbf{v}\times\mathbf{B}) f_j \tag{2.1.4}$$

Inserting into 2.1.1 yields the Vlasov equation

$$\begin{aligned} &\frac{\partial}{\partial t} f_j + \nabla_x \cdot (\mathbf{v} f_j) + \nabla_v \cdot \left(\frac{q_j}{m_j}(\mathbf{E}+\mathbf{v}\times\mathbf{B}) f_j \right) \\ =&\frac{\partial}{\partial t} f_j + \mathbf{v}\nabla_x f_j + \frac{q_j}{m_j}(\mathbf{E}+\mathbf{v}\times\mathbf{B})\nabla_v f_j = 0 \end{aligned} \tag{2.1.5}$$

This is the equation describing the behaviour of a collisionless fluid under the influence of electromagnetic fields. It says that for each dynamical trajectory $(\mathbf{x}(t), \mathbf{v}(t))$ obeying the equations of motion (2.1.2), $f_j(\mathbf{x}(t), \mathbf{v}(t), t)$ is a constant. The Vlasov equation, together with Maxwell's equations, gives a complete description of the behaviour of a plasma in the collisionless limit.

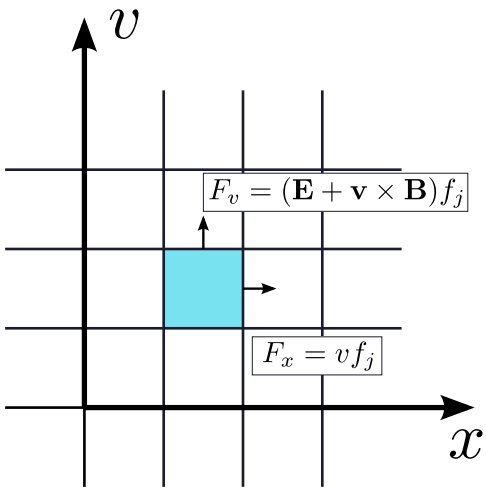

FIGURE 2.1.1. Illustration of the fluxes of the Vlasov Conservation Law

It shall be pointed out that this equation is defined on a 6-dimensional phase space. This makes analytical calculations as well as numerical approaches very difficult. In theory, it is possible to implement so-called Vlasov codes, which solve (2.1.5) numerically. Unfortunately, the high dimension of the problem renders all direct grid-based efforts, using state-of-the-art CPUs, hopeless. This major difficulty gives rise to the particle-in-cell (PIC) method and fluid dynamical treatments, which will both be discussed comprehensively in this thesis.

Nevertheless, a large number of effects in plasma physics can be understood using moment equations of (2.1.5), which are much simpler to handle. Also, since one of the main parts of this thesis focuses on numerical fluid dynamics for plasmas, these moment equations will be derived in the next chapter.

2.2. Moment equations

For many distributions on the measure space $(\Omega, \mathcal{A}, \lambda)$, $\Omega \subset \mathbb{R}^n$, moments can be defined. Well known distribution moments include the center of mass and inertia tensor for solid objects, or the expected value and the covariance matrix for probability distributions.

For phase space distributions, computing integral moments of just the $\mathbf{v}$ part leads to equations for characteristic densities: The particle density ρ, the local mean velocity density $\rho\mathbf{u}$, and even more. This way, the dimensionality of the problem can be greatly reduced.

We start with the Vlasov equation for a particle species j,

$$\frac{\partial}{\partial t} f_j + \mathbf{v}^T \nabla_x f_j + \frac{q_j}{m_j} (\mathbf{E} + \mathbf{v} \times \mathbf{B}) \nabla_v f_j = 0,$$

defined on the vector space $\Gamma =: \Gamma_x \times \Gamma_v$, where the Γ_x denotes the spatial part, and Γ_v is for the velocity subspace.

Let us define the densities mentioned above, namely

- the density $\rho_j := \int\limits_{\Gamma_v} f_j \, d^3v$,
- the local mean velocity $(\rho\mathbf{u})_j := \int\limits_{\Gamma_v} \mathbf{v} f_j \, d^3v$ and
- the pressure tensor $P_j := m_j \int\limits_{\Gamma_v} (\mathbf{v} - \mathbf{u}_j)(\mathbf{v} - \mathbf{u}_j)^T f_j \, d^3v$.

First, by averaging the Vlasov equation over velocities, we get the continuity equation

$$\frac{\partial}{\partial t} \rho_j + \nabla \cdot (\rho \mathbf{v})_j = 0$$

as the zeroth moment of the Vlasov equation.

For the first moment, we must compute the integral

$$\int\limits_{\Gamma_v} \mathbf{v} \left[\frac{\partial f_j}{\partial t} + \mathbf{v}^T \nabla_x f_j + \frac{q_j}{m_j} (\mathbf{E} + \mathbf{v} \times \mathbf{B})^T \nabla_v f_j \right] d\mathbf{v} = 0. \tag{2.2.1}$$

We get the conservation law for the velocity density of a charged fluid,

$$\frac{\partial}{\partial t} (\rho \mathbf{u})_j + \nabla_x \cdot (\rho_j \mathbf{u}_j \mathbf{u}_j^T) = \frac{\rho_j q_j}{m_j} (\mathbf{E} + \mathbf{u}_j \times \mathbf{B}) - \nabla_x \cdot \frac{P_j}{m_j}. \tag{2.2.2}$$

In most cases, one works with the assumption of isotropic pressure. This means that

$$P_j \approx I p_j,$$

where I denotes the unit tensor. Eq. (2.2.2) can then be simplified to

$$\frac{\partial}{\partial t} (\rho \mathbf{u})_j + \nabla_x \cdot \left(\rho_j \mathbf{u}_j \mathbf{u}_j^T \right) = \frac{\rho_j q_j}{m_j} (\mathbf{E} + \mathbf{u}_j \times \mathbf{B}) - \frac{1}{m_j} \nabla_x p_j.$$

This is the conservative form of the momentum equation. It can also be formulated using so-called primitive variables:

$$\frac{\partial}{\partial t} \mathbf{u}_j + (\mathbf{u}_j \cdot \nabla_v) \mathbf{u}_j = \frac{q_j}{m_j} (\mathbf{E} + \mathbf{u}_j \times \mathbf{B}) - \frac{1}{\rho_j m_j} \nabla_x p_j.$$

These derivations can also be found in [**38**].

CHAPTER 3

Principles of the particle-in-cell method

3.1. Concept

The field of plasma physics offers a huge richness of interesting effects, complex phenomena and useful technical applications. In high energy density plasma research, one studies e.g. the interaction of extremely intense laser pulses ($I > 10^{18}\mathrm{W/cm^2}$) and particle bunches with plasma. In the presence of laser intensities of more than 10^{15}-10^{16} $\mathrm{W/cm^2}$, effects like barrier suppression ionization **[39]** or multiphoton ionization **[40]** cause a gas to immediately enter plasma state.

Such scenarios typically involve large numbers of electrons and highly nonlinear effects - pure analytical models are possible, but very difficult, involving severe approximations and restrictions. In order to gain a deep understanding of the phenomena, simulations are indispensable.

Within the problems investigated in this thesis, collective electromagnetic phenomena are dominant. Densities are too low for quantum effects to be important, and collisions can be included in a simplified fashion, if necessary.

Therefore, the relevant physical laws are the dimensionless Maxwell equations,

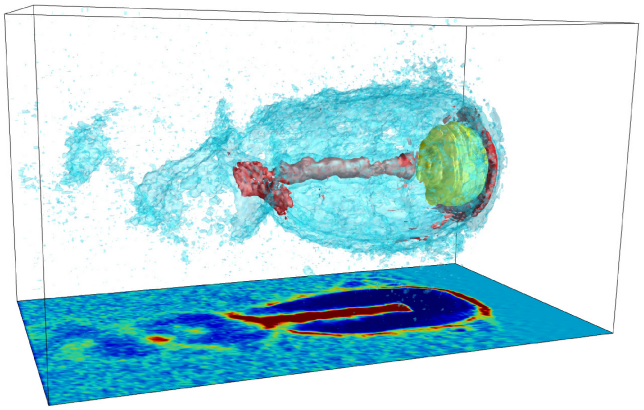

FIGURE 3.1.1. Three-dimensional particle-in-cell simulation of the bubble regime of laser wake field acceleration. The yellow isosurface represents the high intensity laser pulse, which completely pushes all electrons away (blow-out regime), creating a bubble (blue isosurface). This extremely nonlinear effect requires powerful simulation tools, which can self-consistently treat non-equilibrium phenomena.

$$\nabla \cdot \mathbf{E} = \rho \tag{3.1.1}$$

$$\nabla \cdot \mathbf{B} = 0 \tag{3.1.2}$$

$$\frac{\partial}{\partial t}\mathbf{E} = \nabla \times \mathbf{B} - \mathbf{J} \tag{3.1.3}$$

$$\frac{\partial}{\partial t}\mathbf{B} = -\nabla \times \mathbf{E} \tag{3.1.4}$$

and the relativistic version of Vlasov's equation,

$$\frac{\partial}{\partial t} f_j + \mathbf{v}^T \nabla_x f_j + q_j \left(\mathbf{E} + \mathbf{v} \times \mathbf{B}\right) \nabla_p f_j = 0, \tag{3.1.5}$$

where

$$\mathbf{v}(\mathbf{p}) := \frac{\mathbf{p}}{\gamma} = \frac{\mathbf{p}}{\sqrt{1 + \mathbf{p}^2}},$$

and $\mathbf{p}$ is the relativistic momentum, given in units of $m_j c$.

Eqs. (3.1.1)-(3.1.2) can be simplified even more: As it is generally known, putting together (3.1.1) and (3.1.3) yields the charge continuity equation

$$\frac{\partial}{\partial t}\rho + \nabla \cdot \mathbf{J} = 0. \tag{3.1.6}$$

Conversely, if the simulation system we will use satisfies (3.1.6), thus conserving the charges, it holds

$$\frac{\partial}{\partial t}\nabla \cdot \mathbf{E} = -\nabla \cdot \mathbf{J} = \frac{\partial}{\partial t}\rho,$$
$$\frac{\partial}{\partial t}\nabla \cdot \mathbf{B} = 0.$$

This means that it is not necessary to repeatedly solve (3.1.1) and (3.1.2). If they were fulfilled at the very beginning of the simulation, and our scheme satisfies (3.1.6), they will always be fulfilled. We end up with

$$\frac{\partial}{\partial t}\mathbf{E} = \nabla \times \mathbf{B} - \mathbf{J} \tag{3.1.7}$$

$$\frac{\partial}{\partial t}\mathbf{B} = -\nabla \times \mathbf{E} \tag{3.1.8}$$

$$\frac{\partial}{\partial t} f_j = -\mathbf{v}^T \nabla_x f_j - q_j \left(\mathbf{E} + \mathbf{v} \times \mathbf{B}\right) \nabla_p f_j. \tag{3.1.9}$$

In many setups of laser-plasma and plasma-plasma interaction, local thermal equilibrium cannot be assumed, i.e. in general, momentum distributions are non-gaussian. Eq. 3.1.9 could in theory be solved using finite-volume fluid methods [**41, 42, 43, 44, 45**] or semi-Lagrange schemes [**46**], but requires a six-dimensional mesh for 3D physics. Apart from being highly inefficient, even the most powerful supercomputers available today will fail at simulating such a mesh with realistic resolution.

How can this computational problem be reduced?

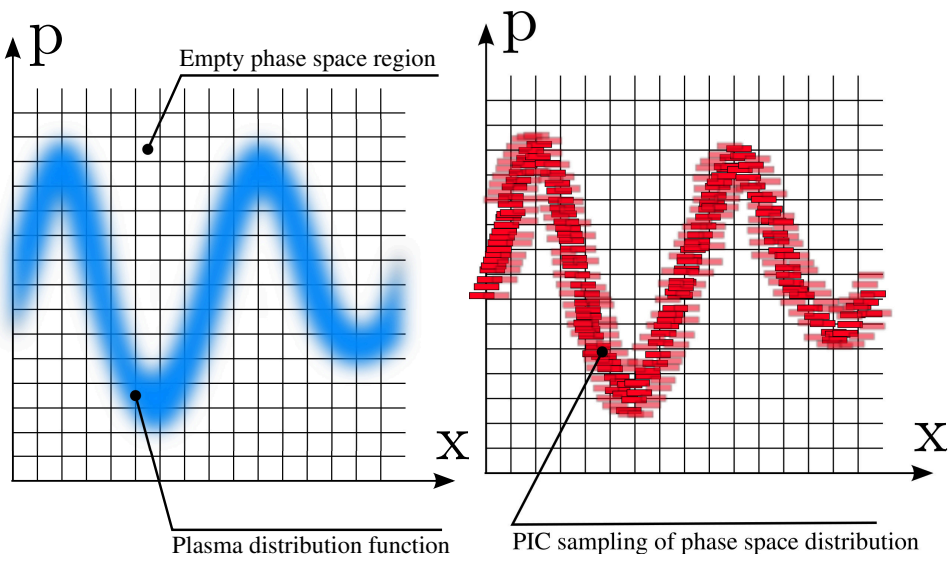

FIGURE 3.1.2. The left picture shows a typical phase space distribution of a 1D wake field. This distribution is then represented by finite sized macroparticles (right picture).

Looking closely at typical phase space diagrams reveals a possible solution: The actual plasma covers only a very tiny subset of the phase space. An equidistant grid on a rectangular fraction of $\Gamma = \Gamma_x \times \Gamma_v$ is not necessary at all.

The idea of the particle-in-cell method is to represent the plasma with *macroparticles*, statistically populating the phase space with a finite number of samples.

This approach can be viewed as a lagrangian model, in contrast to eulerian models: Instead of discretizing partial differential equations for the phase space distribution functions, we track trajectories of small charge bunches. Thus, the function f_j is approximated as

$$f_j \approx \sum_{n=1}^{N_j} W_n^{ph} S^{ph}(\mathbf{x} - \mathbf{x}_n, \mathbf{p} - \mathbf{p}_n),$$

where N_j is the total number of macroparticles of the species j, W_n^{ph} is a weighting coefficient, and S^{ph} specifies the shape function of a particle. In the widely used *cloud-in-cell* approach, we set

$$S^{ph}(\mathbf{x}, \mathbf{p}) : \quad = \delta(\mathbf{p}) \quad \begin{cases} 1, & \text{if } |x_\alpha| < \frac{\Delta x_\alpha}{2}, \alpha = x, y, z \\ 0 & \text{otherwise} \end{cases}. \tag{3.1.10}$$

The Dirac delta distribution in (3.1.10) simply means that one particle only has one momentum. At the same time, it is smeared out in the spatial coordinates, with a rectangular shape. In the actual PIC implementation, we store $\mathbf{x}_n, \mathbf{p}_n$ and the weight W_n^{ph} for each particle. Plasma movement is then modeled by solving the equations of motion for each particle:

$$\frac{\partial}{\partial t}\mathbf{x}_n = \frac{\mathbf{p}_n}{m_j\sqrt{1+\mathbf{p}_n^2}} \tag{3.1.11}$$

$$\frac{\partial}{\partial t}\mathbf{p}_n = q_j\left(\mathbf{E}+\mathbf{v}\times\mathbf{B}\right). \tag{3.1.12}$$

This is done by interpolating the electric and magnetic field onto the particles' center of mass, and using them in order to update $\mathbf{p}_n$. With the new momentum information, the particle is then pushed to a new position, creating a current density

$$\mathbf{J}_n := \int_{\Gamma_X} q_j W_n^{ph} S^{ph}(\mathbf{x}-\mathbf{x}_n(t), \mathbf{p}-\mathbf{p}_n(t)).$$

That current density acts back on the grid-represented electric field.

Although the basic concept of the PIC algorithm can be depicted quickly, it is necessary to explain its components with more detail. In the next chapter, we will see how the self-consistent grid-based EM field solver works. Chapter 3.7 then explains how particles are arranged, pushed, moved and how their currents must be computed.

3.2. The Finite Difference Time Domain (FDTD) method

Full electromagnetic Particle-in-Cell simulation codes always feature a self-consistent description of electric and magnetic fields involved. This means that the full Maxwell's equations are solved in the time domain. There are no simplifications, or steady-state solutions such as Coulombs law for particle-particle interactions.

This self-consistent modeling is one of the features making the PIC method that powerful and versatile. It enables precise simulations of few-cycle laser pulses, non-equilibrium electrical and magnetic phenomena, microwave devices and many more.

In this section, we will focus on the FDTD method used in the VLPL code. It is the most prominent, important, and by far most widely used electromagnetic solution technique available. Since the scientific community working with FDTD counts thousands of contributors, the method is well estabilished and tested with good mathematical foundation, and offers a wide range of possible extensions. Some of these extensions will also be discussed in this thesis.

The basic concept of FDTD was first proposed by Kane Yee in 1966 [**47**]. It addresses solving the equations

$$\frac{\partial}{\partial t}\mathbf{E} = \nabla\times\mathbf{B}$$

$$\frac{\partial}{\partial t}\mathbf{B} = -\nabla\times\mathbf{E}. \tag{3.2.1}$$

The design takes into account the fact that the right-hand side only involves curls of vector fields, and that the right-hand side for the **E**-components does not depend on**E** itself. This suggests the use of numerical splitting schemes as well as staggered and leap-frog schemes. So, the algorithm consists of

(1) Defining the computational domain and creating a rectangular grid.
(2) Storing the full **E**- and **H**-fields for each grid cell.

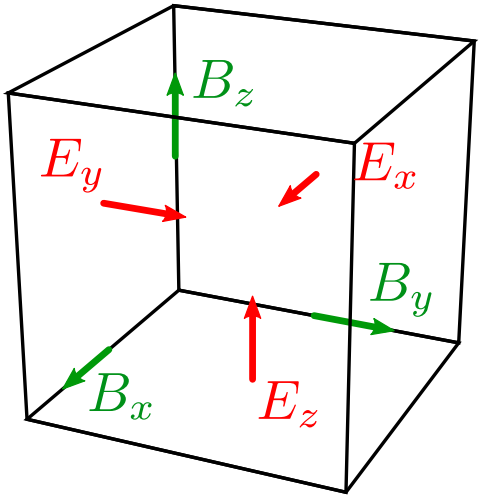

FIGURE 3.2.1. Structure of the Yee grid, where electric field components are defined on the cell faces, while magnetic fields point along the edges.

(3) Employing a special staggered space discretization scheme for the field components.
(4) Using a Strang splitting or leap-frog scheme for time integration.

Modern Particle-in-Cell simulation codes always feature a self-consistent description of electric and magnetic fields involved. This means that the full Maxwell's equations are solved in time. There are no simplifications, or steady-state solutions such as Coulombs law for particle-particle interactions.

This self-consistent modeling is one of the features making the PIC method that powerful and versatile. It enables precise simulations of few-cycle laser pulses, non-equilibrium electrical and magnetic phenomena, microwave devices and many more.

In this section, we will focus on the FDTD method used in the VLPL code. It is the most prominent, important, and by far most widely used electromagnetic solution technique available. Since the scientific community working with FDTD counts thousands of contributors, the method is well estabilished and tested with good mathematical foundation, and offers a wide range of possible extensions. Some of these extensions will also be discussed in this thesis.

3.3. Spatial discretization

The basic spatial discretization of the Yee FDTD scheme works as depicted in figure 3.2.1. Intuitively, it might seem convenient to put all the fields at the same position in the cell center. Unfortunately, such a scheme would lead to large numerical errors and dispersion.

Instead, the field components are separated, with **E** components located at the cell faces, and **B** components at the edges. Regarding those virtual positions, one

often writes the discretized field components as follows:

$$E_x|_{i,\,j+\frac{1}{2},\,k+\frac{1}{2}},\ E_y|_{i+\frac{1}{2},\,j,\,k+\frac{1}{2}},\ E_z|_{i+\frac{1}{2},\,j+\frac{1}{2},\,k},$$
$$B_x|_{i+\frac{1}{2},\,j,\,k},\ B_y|_{i,\,j+\frac{1}{2},\,k},\ B_z|_{i,\,j,\,k+\frac{1}{2}}.$$

These quantities are defined on a rectangular grid

$$\mathcal{G} := \{0...n_x - 1\} \times \{0...n_y - 1\} \times \{0...n_z - 1\} \subset \mathbb{Z}^3.$$

Note that the shifted indices represent the field component's position in the cell. This configuration must not be mistaken with the setup in the actual implementation: The choice of the virtual grid configuration has no impact on the way the variables are stored in memory. It just serves as a necessary convention for the numerical schemes employed.

For these variables, we can now easily define a symmetric, second order approximation for the curl operators.

$$\nabla \times \mathbf{B} = \begin{pmatrix} \partial_y B_z - \partial_z B_y \\ \partial_z B_x - \partial_x B_z \\ \partial_x B_y - \partial_y B_x \end{pmatrix}$$

$$\downarrow$$

$$\begin{aligned}(\tilde{\nabla} \times \mathbf{B})_x|_{i,\,j+\frac{1}{2},\,k+\frac{1}{2}} &:= \frac{B_z|_{i,\,j+1,\,k+\frac{1}{2}} - B_z|_{i,\,j,\,k+\frac{1}{2}}}{\Delta y} - \frac{B_y|_{i,\,j+\frac{1}{2},\,k+1} - B_y|_{i,\,j+\frac{1}{2},\,k}}{\Delta z} \\ &= \hat{d}_y B_z|_{i,\,j+\frac{1}{2},\,k+\frac{1}{2}} - \hat{d}_z B_y|_{i,\,j+\frac{1}{2},\,k+\frac{1}{2}},\end{aligned} \tag{3.3.1}$$

with the other components defined analogously.

The symmetric finite difference operators $\hat{d}_\alpha$ are defined as follows:

$$\begin{aligned}\hat{d}_x f|_{a,b,c} &= \frac{1}{\Delta x}\left(f|_{a+\frac{1}{2},b,c} - f|_{a-\frac{1}{2},b,c}\right) \\ \hat{d}_y f|_{a,b,c} &= \frac{1}{\Delta y}\left(f|_{a,b+\frac{1}{2},c} - f|_{a,b-\frac{1}{2},c}\right) \\ \hat{d}_z f|_{a,b,c} &= \frac{1}{\Delta z}\left(f|_{a,b,c+\frac{1}{2}} - f|_{a,b,c-\frac{1}{2}}\right).\end{aligned}$$

Using this appoximation for the other components similarly leads to the semi-discrete Maxwell's equations:

$$\partial_t \begin{pmatrix} E_x|_{i,\,j+\frac{1}{2},\,k+\frac{1}{2}} \\ E_y|_{i+\frac{1}{2},\,j,\,k+\frac{1}{2}} \\ E_z|_{i+\frac{1}{2},\,j+\frac{1}{2},\,k} \end{pmatrix} = \begin{pmatrix} \hat{d}_y B_z|_{i,\,j+\frac{1}{2},\,k+\frac{1}{2}} - \hat{d}_z B_y|_{i,\,j+\frac{1}{2},\,k+\frac{1}{2}} \\ \hat{d}_z B_x|_{i+\frac{1}{2},\,j,\,k+\frac{1}{2}} - \hat{d}_x B_z|_{i+\frac{1}{2},\,j,\,k+\frac{1}{2}} \\ \hat{d}_x B_y|_{i+\frac{1}{2},\,j+\frac{1}{2},\,k} - \hat{d}_y B_x|_{i+\frac{1}{2},\,j+\frac{1}{2},\,k} \end{pmatrix} - \begin{pmatrix} J_x|_{i,\,j+\frac{1}{2},\,k+\frac{1}{2}} \\ J_y|_{i+\frac{1}{2},\,j,\,k+\frac{1}{2}} \\ J_z|_{i+\frac{1}{2},\,j+\frac{1}{2},\,k} \end{pmatrix} \tag{3.3.2}$$
$$=: \tilde{\nabla} \times \mathbf{B} - \mathbf{J}$$

$$\partial_t \begin{pmatrix} B_x|_{i+\frac{1}{2},\,j,\,k} \\ B_y|_{i,\,j+\frac{1}{2},\,k} \\ B_z|_{i,\,j,\,k+\frac{1}{2}} \end{pmatrix} = - \begin{pmatrix} \hat{d}_y E_z|_{i+\frac{1}{2},\,j,\,k} - \hat{d}_z E_y|_{i+\frac{1}{2},\,j,\,k} \\ \hat{d}_z E_x|_{i,\,j+\frac{1}{2},\,k} - \hat{d}_x E_z|_{i,\,j+\frac{1}{2},\,k} \\ \hat{d}_x E_y|_{i,\,j,\,k+\frac{1}{2}} - \hat{d}_y E_x|_{i,\,j,\,k+\frac{1}{2}} \end{pmatrix} =: -\tilde{\nabla} \times \mathbf{E}. \tag{3.3.3}$$

Note that, when computing a discretized curl, the scheme applies a symmetric finite difference using a stencil involving only two cells. This is not possible with a non-staggered grid, as symmetric finite differences would 'jump' over the middle cell

of a three-cell stencil. This fact has major consequences for the behaviour of the scheme, as will be shown later.

3.4. Time discretization

As soon as one has obtained a stable semi-discrete scheme for a partial differential equation, the latter transform into an ordinary differential equation (ODE) with just a very large dimension. Thus, one can try to use any stable ODE solver on it, e.g. Runge-Kutta methods or multistep methods. This is a common practice in the numerical solution of PDEs.

However, looking closely at formulas (3.3.2,3.3.3) shows an interesting feature: The right-hand side for $\mathbf{E}$ does not depend on $\mathbf{E}$ itself, while the right-hand side for $\mathbf{B}$ again does not depend on $\mathbf{B}$. If we could ignore the second line, which means $\mathbf{B} = const$, we could solve (3.3.2) exactly, and vice versa.

This means that Maxwell's equations offer an excellent opportunity for *Operator Splitting schemes.* These schemes can constitute elegant solvers for ODEs, exhibiting many advantages. Although a complete description is not possible here (please see, e.g. [**48**]), we shall briefly summarize the concept.

Let there be an initial value problem

$$y' = f(y) + g(y),\ y(0) = y_0 \tag{3.4.1}$$

which can not be solved analytically for the given conditions, but whose right-hand side can be separated as above. We define the *exact flow*

$$\Phi_t(y_0) := y(t);$$

in other words, the mapping $\Phi_t : \mathbb{R}^n \to \mathbb{R}^n$ turns some initial condition y_0 into the exact solution at time t.

In order to introduce the operator splitting approach, we split (3.4.1) into two different equations, ignoring either $f(y)$ or $g(y)$:

$$y' = f(y),\ y(0) = y_0 \tag{3.4.2}$$

$$y' = g(y),\ y(0) = y_0 \tag{3.4.3}$$

Then we can define exact flows Φ_t^f, Φ_t^g analogously for (3.4.2) and (3.4.3).

Splitting methods are most useful for the case where there is no exact solution for (3.4.1), but exact solutions for (3.4.2,3.4.3) are easy. One can then construct numerical solvers by concatenating the exact flows of the split equations, e.g.

$$\Phi_t(y_0) \approx \varphi_t^{LT}(y_0) := \Phi_t^f(\Phi_t^g(y_0)). \tag{3.4.4}$$

This method is called the Lie-Trotter splitting. It can be shown to be 1st order convergent, being just of academic interest at the moment.

A more important alternative, which will turn out to be VLPL's Maxwell solver, is the *Strang splitting*:

$$\Phi_t(y_0) \approx \varphi_t^{STR}(y_0) := \Phi_{t/2}^f(\Phi_t^g(\Phi_{t/2}^f(y_0))) = \Phi_{t/2}^f \circ \Phi_t^g \circ \Phi_{t/2}^f(y_0). \tag{3.4.5}$$

It is one of the most important methods in computational physics, having many names in different fields of research. In molecular dynamics, it takes the form of the Störmer-Verlet scheme, while it can also be rewritten as the well-known Leap-Frog scheme. Its order of convergence is 2, and one of its useful properties is its symmetry, meaning that if

$$y_1 = \varphi_t^{STR}(y_0)$$

then

$$y_0 = \varphi_{-t}^{STR}(y_1).$$

In other words, the Strang splitting is a reversible scheme. This yields important consequences for its energy conservation.

Let us come back to the Maxwell equations. We take the semi-discrete formulation (3.3.2,3.3.3) and apply the Strang splitting, obtaining

$$\mathbf{B}^{n+\frac{1}{2}} = \mathbf{B}^n - \frac{1}{2}\Delta t\tilde{\nabla} \times \mathbf{E}^n \tag{3.4.6}$$

$$\mathbf{E}^{n+1} = \mathbf{E}^n + \Delta t\tilde{\nabla} \times \mathbf{B}^{n+\frac{1}{2}} - \Delta t\, \mathbf{J}^{n+\frac{1}{2}} \tag{3.4.7}$$

$$\mathbf{B}^{n+\frac{1}{2}} = \mathbf{B}^{n+\frac{1}{2}} - \frac{1}{2}\Delta t\tilde{\nabla} \times \mathbf{E}^{n+1}. \tag{3.4.8}$$

This is one of the most widely used FDTD electromagnetic field solvers, and, at the same time, the field solver of the PIC code VLPL.

At this point, it appears convenient to characterize this scheme and investigate its properties. Since it is explicit, one can expect it to have some stability condition. Furthermore, we might want to quantify its approximation error. These questions shall be answered by linear stability and dispersion analysis in the next chapter.

3.5. Properties of the FDTD Yee scheme: Stability

As is generally known, plain waves like

$$\mathbf{E}(\mathbf{x}, t) = \mathbf{E}_0 e^{i(\mathbf{k}\cdot\mathbf{x} - \omega t)}$$
$$\mathbf{B}(\mathbf{x}, t) = \mathbf{B}_0 e^{i(\mathbf{k}\cdot\mathbf{x} - \omega t)},$$

$\mathbf{E}_0 \perp \mathbf{k}$, $\mathbf{B}_0 \perp \mathbf{k}$,with arbitrarily large wave vectors $\mathbf{k}$ are solutions to (3.2.1) in vacuum, with the dispersion relation

$$\omega^2 \quad = \quad c^2\mathbf{k}^2.$$

Waves, apart from standing waves, always mean local coupled oscillations. Experience tells us that explicit time integrators will either resolve these oscillations or explode. Hence, we expect the stability of the scheme to be connected to the highest wave vector which can occur. In the semi-discrete scheme (3.3.2,3.3.3), the set of possible $\mathbf{k}$ is, fortunately, bounded, but grows with decreasing grid steps $\Delta x, \Delta y, \Delta z$.

The Courant-Friedrichs-Levy (CFL) stability condition can be derived via the tool of Von Neumann linear stability analysis. It works as a sufficient stability condition only for linear PDEs, and the orders of derivatives must not exceed two,

but the problem at hand satisfies these requirements. In this chapter, we will perform a Von Neumann linear stability analysis of the Maxwell solver, and derive a stability condition.

Without the current term $\mathbf{J}^{n+\frac{1}{2}}$, and using periodic boundary conditions, the Strang splitting step (3.4.6)-(3.4.8) can be viewed as a linear operator $S : \mathbb{R}^{6n_x n_y n_z} \to \mathbb{R}^{6n_x n_y n_z}$ on the field vector $(\mathbf{E}^n, \mathbf{B}^n)$ such that

$$\begin{bmatrix} E_x^{n+1}|_{i,\,j+\frac{1}{2},\,k+\frac{1}{2}} \\ E_y^{n+1}|_{i+\frac{1}{2},\,j,\,k+\frac{1}{2}} \\ E_z^{n+1}|_{i+\frac{1}{2},\,j+\frac{1}{2},\,k} \\ B_x^{n+1}|_{i+\frac{1}{2},\,j,\,k} \\ B_y^{n+1}|_{i,\,j+\frac{1}{2},\,k} \\ B_z^{n+1}|_{i,\,j,\,k+\frac{1}{2}} \end{bmatrix}_{(i,j,k)\in\mathcal{G}} = S \begin{bmatrix} E_x^{n}|_{i,\,j+\frac{1}{2},\,k+\frac{1}{2}} \\ E_y^{n}|_{i+\frac{1}{2},\,j,\,k+\frac{1}{2}} \\ E_z^{n}|_{i+\frac{1}{2},\,j+\frac{1}{2},\,k} \\ B_x^{n}|_{i+\frac{1}{2},\,j,\,k} \\ B_y^{n}|_{i,\,j+\frac{1}{2},\,k} \\ B_z^{n}|_{i,\,j,\,k+\frac{1}{2}} \end{bmatrix}_{(i,j,k)\in\mathcal{G}}.$$

For stability, we require the numerical solution to be bounded for all times, which is fulfilled if the operator norm$\|S\|_2$ is less than one.

Every field $F \in \mathbb{R}^{6n_x n_y n_z}$ can be decomposed into plane waves by discrete 3D fourier transform (which form an orthonormal basis on $\mathbb{R}^{6n_x n_y n_z}$). Thus, without loss of generality, we will now investigate what effect the operator S has on a plane wave

$$\begin{aligned} B_x|^n_{i+\frac{1}{2},j,k} &:= \hat{B}_x^n(\mathbf{k}) e^{I\mathbf{k}\cdot\mathbf{r}_{i+\frac{1}{2},j,k}}, \\ B_y|^n_{i,j+\frac{1}{2},k} &:= \hat{B}_y^n(\mathbf{k}) e^{I\mathbf{k}\cdot\mathbf{r}_{i,j+\frac{1}{2},k}}, \\ E_x|^n_{i,j+\frac{1}{2},k+\frac{1}{2}} &:= \hat{E}_x^n(\mathbf{k}) e^{Ik\cdot\mathbf{r}_{i,j+\frac{1}{2},k+\frac{1}{2}}}, \end{aligned} \tag{3.5.1}$$

with the other components defined analogously. The positions are defined as

$$\mathbf{r}_{i,\,j,\,k} := \begin{bmatrix} i\Delta x \\ j\Delta y \\ k\Delta z \end{bmatrix}.$$

From Lemma 5 in the Appendix, we see that the operator S has the eigenvalues

$$\lambda_S = [-2\sqrt{\alpha^4 - \alpha^2} - 2\,\alpha^2 + 1, 2\sqrt{\alpha^4 - \alpha^2} - 2\,\alpha^2 + 1, 1],$$

with $\alpha = \alpha_x^2 + \alpha_y^2 + \alpha_z^2$, $\alpha_j = \frac{\Delta t}{\Delta x}$.

For $\alpha^2 < 1$, the term $\sqrt{\alpha^4 - \alpha^2}$ becomes purely imaginary, while $-2\alpha^2 + 1$ is always real, hence

$$\begin{aligned} |\lambda_{S,1,2}|^2 &= 4\left(\alpha^2 - \alpha^4\right) + \left(2\alpha^2 + 1\right)^2 \\ &= 1. \end{aligned}$$

This is the important stability result for the Strang-split Yee EM algorithm. It tells us that, given the condition

$$\Leftrightarrow \quad \Delta t^2 \leq \left(\left(\tfrac{1}{\Delta x}\right)^2 + \left(\tfrac{1}{\Delta y}\right)^2 + \left(\tfrac{1}{\Delta y}\right)^2 \right)^{-1}, \tag{3.5.2}$$

the operator S is an isometry.

The implications of this feature are exact energy conservation (except for round-off errors), and stability of the scheme (because the solution norm is constant, thus bounded).

3.6. Properties of the FDTD Yee scheme: Dispersion

In the last chapters, we have seen that the Yee FDTD scheme is 2nd order convergent in space and time and it conserves the electromagnetic field energy. Furthermore, a plane wave with a wave vector $\mathbf{k}$ will be mapped onto a plane wave with the same wave vector.

One might ask: Where is the numerical error?

It turns out that the error of the scheme lies not in the amplitudes of solutions, but in their phases. The error manifests itself solely through *numerical dispersion.* It causes the speed of light in vacuum to be smaller than c in the simulation. For the 3D Yee scheme, the dispersion relation of a plane wave with wave vector $\mathbf{k}$ is

$$\left[\frac{\sin\left(\frac{\omega\Delta t}{2}\right)}{c\Delta t}\right]^2 = \left[\frac{\sin\left(\frac{k_x\Delta x}{2}\right)}{\Delta x}\right]^2 + \left[\frac{\sin\left(\frac{k_y\Delta y}{2}\right)}{\Delta y}\right]^2 + \left[\frac{\sin\left(\frac{k_z\Delta z}{2}\right)}{\Delta z}\right]^2,$$

which is shown e.g. in [**49**].

3.7. Particle-in-cell numerics

In the last chapter, we have learned about the electromagnetic foundations of the PIC method: How EM fields are handled, stored, and advanced in time, and what are the advantages and shortcomings of the Yee scheme. This is the first essential component of a self-consistent PIC code.

The second important component is the particle system. It has to solve the equations

$$\frac{\partial}{\partial t}\mathbf{x}_n = \frac{\mathbf{p}_n}{m_j\sqrt{1+\mathbf{p}_n^2}} \tag{3.7.1}$$

$$\frac{\partial}{\partial t}\mathbf{p}_n = \frac{q_j}{m_j}\left(\mathbf{E}+\mathbf{v}_n\times\mathbf{B}\right). \tag{3.7.2}$$

for the particles, and, while advancing them in space, write the right currents to the grid.

We start with the algorithm for particle kinetics. Typical simulations contain 10^8- 10^9particles; therefore the integration of their equations of motion will take a considerable part of the total CPU time. Additionally, such high numbers of macroparticles will constitute the largest part to the total memory consumption. If we just had to solve this part of the overall problem, namely tracking the particles' trajectories with fixed EM fields, we could use high-order integration methods like Runge-Kutta or multistep schemes. However, multistep algorithms would force us to store a particle's $(\mathbf{x}_n, \mathbf{p}_n)$ multiple times. On the other hand, Runge-Kutta methods require us to evaluate the right-hand sides too often.

It turns out that falling back to the fastest, and least memory-consuming integrators available is the most efficient choice. Looking at (3.7.1) and (3.7.2), one observes that the right-hand side of (3.7.1) does not depend on $\mathbf{x}_n$, while the right-hand side of (3.7.2) only depends on $\mathbf{p}_n$ via the $\mathbf{v}_n\times\mathbf{B}$ term. Again, this makes

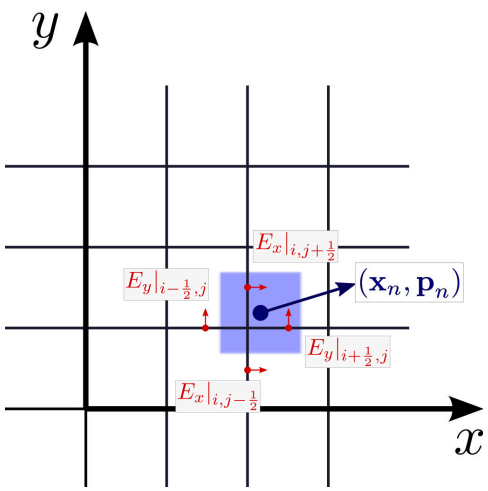

FIGURE 3.7.1. PIC particle in 2D geometry. The surrounding electric field components are linearly interpolated onto the macroparticle's center of mass, pushing its momentum.

the use of splitting methods advisable. It will be shown that a leap-frog method works very effectively here.

Let $(\mathbf{x}_n^m, \mathbf{p}_n^{m-\frac{1}{2}})$ be the phase space coordinates at time $m\Delta t$ of a macroparticle n belonging to species j. Following the leap-frog idea, the momentum is stored for a time $(m-\frac{1}{2})\Delta t$ shifted with respect to the time of the position $m\Delta t$.

The momentum push for the particle looks as follows:

(1) Interpolate $\mathbf{E}^m$ and $\mathbf{B}^m$ linearly onto the particle's center of mass.
(2) Advance $\mathbf{p}_n^{m-\frac{1}{2}} \to \mathbf{p}_n^{m+\frac{1}{2}}$ using the interpolated values $\mathbf{E}_{int}^m$ and $\mathbf{B}_{int}^m$.

Unfortunately, step (2) is not trivial. We can apply another splitting and subdivide step (2) into

(1) $\mathbf{p}_n^- = \mathbf{p}_n^{m-\frac{1}{2}} + \frac{\Delta t}{2}\frac{q_j}{m_j}\mathbf{E}_{int}^m$
(2) $\mathbf{p}_n^- \to \mathbf{p}_n^+$ (somehow for the $\mathbf{v}_n \times \mathbf{B}_{int}^m$ term)
(3) $\mathbf{p}_n^{m+\frac{1}{2}} = \mathbf{p}_n^+ + \frac{\Delta t}{2}\frac{q_j}{m_j}\mathbf{E}_{int}^m$,

taking again advantage of the splitting concept for the electric lorentz force. The intermediate push (2) can e.g. be done using some 2nd order accurate Runge-Kutta method. However, this would have unpleasant consequences for the PIC code's energy conservation. The problem can be understood easily:

Set $\mathbf{E} = 0$, $\mathbf{B} = B_0\mathbf{e}_z$. Then the analytic solution for $\mathbf{v}_n$ is

$$\begin{bmatrix} v_{nx}^{m+1} \\ v_{ny}^{m+1} \\ v_{nz}^{m+1} \end{bmatrix} = \begin{bmatrix} \cos\omega_c\Delta t & \sin\omega_c\Delta t & 0 \\ -\sin\omega_c\Delta t & \cos\omega_c\Delta t & 0 \\ 0 & 0 & 1 \end{bmatrix} \begin{bmatrix} v_{nx}^m \\ v_{ny}^m \\ v_{nz}^m \end{bmatrix},$$

where $\omega_c = (q_j/m_j)B_0$ is the well-known cyclotron frequency. Under these conditions the particle undergoes cyclotron motion with constant amplitude $\|\mathbf{v}_n^m\|_2$. Most explicit, non-symmetric integration schemes will make this amplitude grow

instead, causing unphysical *numerical heating*. With in-simulation time passing, the plasma will heat up itself under the influence of a magnetic field.

Since this has to be prevented, a physically reasonably algorithm will keep this amplitude constant. The method which is actually used in the VLPL PIC code has been proposed by Boris [**50**]. We will follow here the description given in [**25**]. Basically, it computes the rotation caused by the $\mathbf{v}_n \times \mathbf{B}^m_{int}$ term. We know that the velocity $\mathbf{v}$ rotates around the magnetic field component perpendicular to it, $\mathbf{B}^m_{int,\perp}$, by an angle of

$$\theta = \Delta t \frac{q_j \mathbf{B}^m_{int,\perp}}{m_j}.$$

This rotation can be constructed in a simple way without the need to resolve trigonometric functions.

We denote the initial velocity by $\mathbf{v}^-$ and the rotated velocity by $\mathbf{v}^+$. In order to compute $\mathbf{v}^+$, we first want to find a $\mathbf{t} \in \mathbb{R}^3$ such that $\mathbf{v}' := \mathbf{v}^- + \mathbf{v}^- \times \mathbf{t}$ is perpendicular to $(\mathbf{v}^+ - \mathbf{v}^-)$ and $\mathbf{B}^m_{int,\perp}$. The angle between $\mathbf{v}'$ and $\mathbf{v}^-$must be $\theta/2$, so we see from figure 3.7.2 that $\mathbf{t}$ is

$$\mathbf{t} = -\hat{\mathbf{b}} \tan \frac{\theta}{2} = \frac{q_j \mathbf{B}^m_{int}}{m_j} \frac{\Delta t}{2}.$$

Since $\mathbf{v}^+ - \mathbf{v}^-$ is perpendicular to $\mathbf{v}'$, we have $\mathbf{v}^+ = \mathbf{v}^- + \mathbf{v}' \times \mathbf{s}$, where $\mathbf{s}$ is parallel to $\mathbf{B}^m_{int}$, being chosen such that $\|\mathbf{v}^+\|^2 = \|\mathbf{v}^-\|^2$,

$$\mathbf{s} = \frac{2\mathbf{t}}{1+t^2}.$$

It can be shown that this step for $\mathbf{v}^+ \to \mathbf{v}^-$exactly solves for the cyclotron rotation. Putting the components together, the momentum push for a particle n reads

(1) Interpolate $\mathbf{E}^m$ and $\mathbf{B}^m$ linearly onto the particle's center of mass
(2) $\mathbf{p}_n^- = \mathbf{p}_n^{m-\frac{1}{2}} + \frac{\Delta t}{2} \frac{q_j}{m_j} \mathbf{E}^m_{int}$, $\mathbf{v}^- := \frac{\mathbf{p}_n^-}{m_j}$
(3) $\mathbf{v}' := \mathbf{v}^- + \mathbf{v}^- \times \mathbf{t}$ with $\mathbf{t} := \frac{q\mathbf{B}^m_{int}}{m} \frac{\Delta t}{2}$
(4) $\mathbf{v}^+ = \mathbf{v}^- + \mathbf{v}' \times \frac{2\mathbf{t}}{1+t^2}$, $\mathbf{p}_n^{m+\frac{1}{2}} := m_j \mathbf{v}^+$
(5) $\mathbf{p}_n^{m+\frac{1}{2}} = \mathbf{p}_n^+ + \frac{\Delta t}{2} \frac{q_j}{m_j} \mathbf{E}^m_{int}$.

This scheme is readily generalized to the relativistic case.

Still following the Leap-Frog approach, we then use the new particle momenta $\left(\mathbf{p}_n^{m+\frac{1}{2}}\right)_{m=1}^N$ in order to advance the particle positions. This operation is easily written down by

$$\mathbf{x}_n^{m+1} = \mathbf{x}_n^m + \Delta t \frac{\mathbf{p}_n^{m+\frac{1}{2}}}{\sqrt{1 + (\mathbf{p}_n^{m+\frac{1}{2}})^2}}.$$

Now, we are almost done with the particle system - except for the last, and probably most challenging step. After the macroparticles' positions have changed, the charge density $\rho^{m+1}_{i,j,k}$ will, in general, also be different.

Early particle-in-cell simulation codes relied on recomputing the total charge density during each time step. This density was then fed into a poisson's equation solver, in order to obtain the change in **E**. However, on modern massively parallel computers, such global methods, i.e. equation system solvers with solutions depending on global information, become increasingly inefficient. Of course, there are Fourier-based fast poisson solvers and iterative methods such as multigrid or Krylov algorithms (see e.g. [**51**]), but the former are difficult to paralellize, while the latter are not trivial to implement.

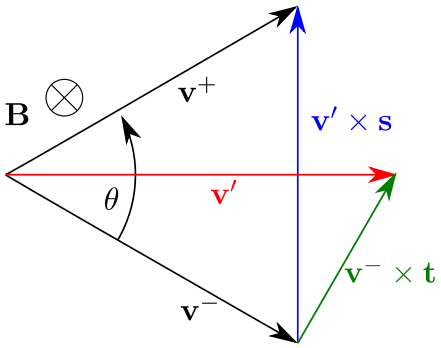

FIGURE 3.7.2. Geometrical interpretation of the magnetic part of the Boris push.

In chapter 3, we have already seen that solving Gauss' law repeatedly is not necessary. As can be proven easily, the finite difference approximations for the curl operators (3.3.1) also satisfy the exact sequence property

$$\tilde{\nabla} \cdot \tilde{\nabla} \times \mathbf{A} = 0, \tag{3.7.3}$$

with

$$\tilde{\nabla} \cdot \mathbf{A}|_{i+\frac{1}{2},j+\frac{1}{2},k+\frac{1}{2}} := \sum_{\alpha=x,y,z} \hat{d}_\alpha A_\alpha|_{i+\frac{1}{2},j+\frac{1}{2},k+\frac{1}{2}}$$

Thus, if $\tilde{\nabla} \cdot \mathbf{E}^0|_{i+\frac{1}{2},j+\frac{1}{2},k+\frac{1}{2}} = \rho^0_{i+\frac{1}{2},j+\frac{1}{2},k+\frac{1}{2}}$, and we find a charge conserving current scheme $J_x^{PIC}|^{m+\frac{1}{2}}_{i,j+\frac{1}{2},k+\frac{1}{2}}$,etc. such that

$$\frac{\rho^{m+1}_{i+\frac{1}{2},j+\frac{1}{2},k+\frac{1}{2}} - \rho^m_{i+\frac{1}{2},j+\frac{1}{2},k+\frac{1}{2}}}{\Delta t} = \tilde{\nabla} \cdot \mathbf{J}^{PIC}|^{m+\frac{1}{2}}_{i+\frac{1}{2},j+\frac{1}{2},k+\frac{1}{2}},$$

the discrete version of Gauss' law will always be fulfilled. The simplest of such schemes is the "zeroth-order current weighting" method (described in [**25**]), where the particles are just counted when they pass the cell border. It achieves exact charge conservation by generating a current impulse when a particle passes a cell boundary. This approach, however, causes significant numerical noise.

The solution used in the VLPL code has been proposed in [**52**].

It resembles to integrating the currents on each cell boundary over the time interval $[t^m, t^{m+1}]$. Let the cells be indexed with $(i,j,k) \in \mathcal{G} := \{0...n_x - 1\} \times \{0...n_y - 1\} \times \{0...n_z - 1\} \subset \mathbb{Z}^3$. For the sake of simplicity, we set the grid steps $\Delta x = \Delta y = \Delta z = 1$, and define particle positions (x,y,z) such that a particle with $x = i$, $y = j$, $z = k$ lies in the center of cell (i,j,k). We then define the in-cell offset $(\xi,\eta,\zeta) \in [0,1[^3$; so a particle at $(x,y,z) = (i+\xi,\, j+\eta,\, k+\zeta)$ lies partly in the eight cells $\{(\alpha,\beta,\gamma) \in [i,i+1] \times [j,j+1] \times [k,k+1]\}$.

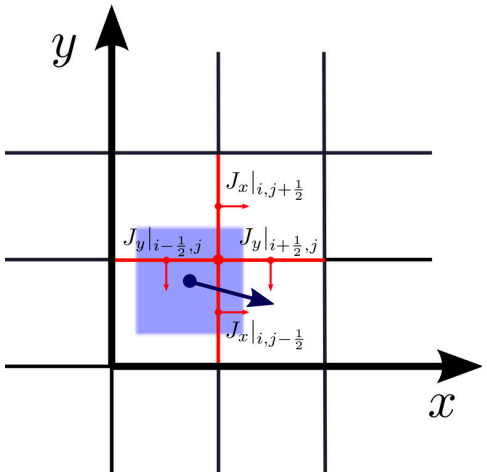

FIGURE 3.7.3. A particle in 2D always creates currents on four cell boundaries at a moment. These currents must be integrated over $[t^m, t^{m+1}]$.

For a macroparticle with a rectangular shape function (cloud-in-cell), its fraction inside a neighbouring cell is

$$\int_{\text{Cell}} S(x-x_n, y-y_n, z-z_n)dx\,dy\,dz.$$

At the same time, the particle intersects with twelve boundaries. In order to shorten the calculations, we just show the currents on the boundaries with $\vec{e}_x$ normal, which are given by

$$\begin{aligned}
J_x|_{i+1,\,j+\frac{1}{2},\,k+\frac{1}{2}} &= v_x(1-\eta)(1-\zeta)\\
J_x|_{i+1,\,j+\frac{3}{2},\,k+\frac{1}{2}} &= v_x\eta(1-\zeta)\\
J_x|_{i+1,\,j+\frac{1}{2},\,k+\frac{3}{2}} &= v_x(1-\eta)\zeta\\
J_x|_{i+1,\,j+\frac{3}{2},\,k+\frac{3}{2}} &= v_x\eta\zeta.
\end{aligned}$$

Let there be a particle with initial position $(x,y,z) = (i+\xi_0,\, j+\eta_0,\, k+\zeta_0)$, which moves linearly within its initial cell without leaving the twelve boundaries it crossed at the beginning. This means that the particle follows a trajectory

$$\begin{pmatrix} x\\ y\\ z\end{pmatrix}(t) = \begin{pmatrix} i\\ j\\ k\end{pmatrix} + \begin{pmatrix} \xi_0+v_xt\\ \eta_0+v_yt\\ \zeta_0+v_zt\end{pmatrix},$$

where

$$\begin{pmatrix} \xi_0+v_xt\\ \eta_0+v_yt\\ \zeta_0+v_zt\end{pmatrix} \in [0,1[, \text{ for } t\in[0,\Delta t[.$$

So, the currents are

$$
\begin{aligned}
J_x|_{i+1,\,j+\frac{1}{2},\,k+\frac{1}{2}} &= v_x(1-(\eta_0+v_y t))(1-(\zeta_0+v_z t))\\
J_x|_{i+1,\,j+\frac{3}{2},\,k+\frac{1}{2}} &= v_x(\eta_0+v_y t)(1-(\zeta_0+v_z t))\\
J_x|_{i+1,\,j+\frac{1}{2},\,k+\frac{3}{2}} &= v_x(1-(\eta_0+v_y t))(\zeta_0+v_z t)\\
J_x|_{i+1,\,j+\frac{3}{2},\,k+\frac{3}{2}} &= v_x(\eta_0+v_y t)(\zeta_0+v_z t).
\end{aligned}
$$

Defining the intermediate positions

$$\bar{\xi} \;=\; (\xi_2+\xi_1)/2,\ \bar{\eta}=(\eta_2+\eta_1)/2,\ \bar{\zeta}=(\zeta_2+\zeta_1)/2$$

and setting the total distances travelled

$$\Delta x \;=\; v_x\Delta t,\ \Delta y = v_y\Delta t,\ \Delta z = v_z\Delta t$$

we integrate the current

$$
\begin{aligned}
&\tilde{J}_x|_{i+1,\,j+\frac{3}{2},\,k+\frac{3}{2}} :=\\
&\int_0^{\Delta t} J_x|_{i+1,\,j+\frac{3}{2},\,k+\frac{3}{2}}\,dt \quad = \Delta x\bar{\eta}\bar{\zeta}+\Delta x\Delta y\Delta z\Delta t^2/12.
\end{aligned}
$$

This is the current contribution on the surface $(i+1,\ j+\frac{3}{2},\ k+\frac{3}{2})$ for one particle of weight 1 passing linearly through it. The other contributions are

$$
\begin{aligned}
\tilde{J}_x|_{i+1,\,j+\frac{3}{2},\,k+\frac{1}{2}} &= \Delta x\bar{\eta}(1-\bar{\zeta})-\Delta x\Delta y\Delta z\Delta t^2/12\\
\tilde{J}_x|_{i+1,\,j+\frac{1}{2},\,k+\frac{3}{2}} &= \Delta x(1-\bar{\eta})\bar{\zeta}-\Delta x\Delta y\Delta z\Delta t^2/12\\
\tilde{J}_x|_{i+1,\,j+\frac{1}{2},\,k+\frac{1}{2}} &= \Delta x(1-\bar{\eta})(1-\bar{\zeta})+\Delta x\Delta y\Delta z\Delta t^2/12.
\end{aligned}
$$

The other 8 currents follow analogously via cyclic permutation of spatial directions.

This is the simplest, and most common case of particle movement, where the particle stays in its initial cell, generating currents on twelve boundaries. However, there are cases in which a particle leaves its initial cell in one time step. In such situations, the particle movement is decomposed into a number of eight-cell movements, which are processed in the way depicted above. These algorithms are also depicted in [**25, 52**].

3.8. Parallelization

Among the various simulation concepts presently known, the particle-in-cell method is one of the most computationally expensive. Realistic, large scale simulations can easily take days, months or even years of CPU time. Trusting in Moore's law for increasing CPU clock frequency is hopeless here. This means that simulation codes must be parallelized in order to aim for more complex setups.

Fortunately, the PIC concept is relatively easy to parallelize: The mesh based field descriptions rely on linear stencil operations, which means that each grid point is modified using other grid points in its neighborhood. The particles follow relativistic equations of motion, making their velocity bounded by c. From the CFL stability condition, it follows that the time step is restricted by

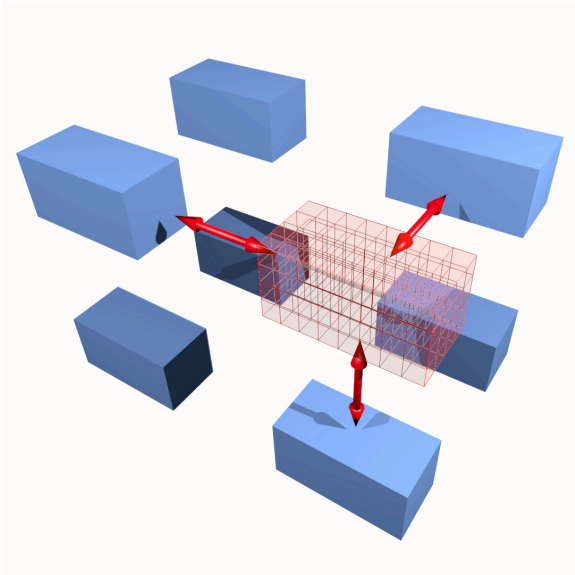

FIGURE 3.8.1. Three-dimensional visualization of a simulation domain split into $2 \times 2 \times 2$ subdomains. Each subdomain is held by one computational process which again works with its designated part of the total mesh. Interprocess communication and job launching is done with MPI.

$$\Delta t \leq \min(\Delta x, \Delta y, \Delta z),$$

so a moving particle will never travel further than one cell per time step. These features make the PIC algorithm a local one: The (rectangular) simulation domain can be divided into a number of equally shaped subdomains. These subdomains will then communicate with each other, but due to the locality of PIC, each of them only has to exchange data with its direct neighbors. So, the number of send/receive operations for each processor is $\mathcal{O}(1)$, which means that there is no theoretical limit for the parallel scaling.

In this chapter, the parallelization scheme for the VLPL PIC code (and many others) will be described.

It works in a simple way: After having defined the rectangular simulation domain and chosen the grid steps, one chooses *partition numbers* for each spatial diraction, e.g. $P_x = P_y = P_z = 2$. The simulation box will then be divided into $P_\alpha$equally sized parts along each direction α, which results in $P_x P_y P_z$ subdomains of likewise rectangular shape, each of them held by one process.

In VLPL, the Message Passing Interface (MPI) for communication and process management is used. After the MPI job launcher has started $P_x P_y P_z$ processes, they will start finding their in-box offsets according to their MPI ranks. At this time, each process knows where its spatial domain is located, and which processes are its direct neighbors. It will then allocate their subgrids in memory, with an additional layer of 2 grid cells attached at the borders. This is shown in figure 3.8.2. Here, a 2D grid is divided into 2×2 subgrids. Each subgrid gets a two-cell 'coastline' at the borders. We make use of the fact that the stencil operations of the

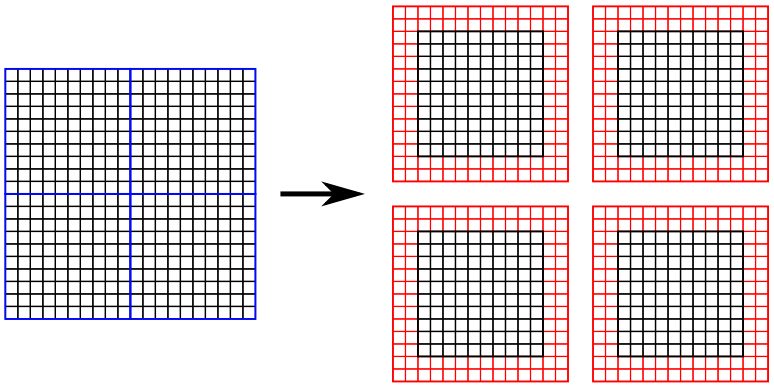

FIGURE 3.8.2. Sketch of the parallelization pattern for mesh-based quantities. The mesh on the left side is decomposed into four equal parts, which are held by different processes. A two-cell 'coastline' is wrapped around each subgrid in order to provide local boundary conditions for stencil operations.

EM field solvers only access the direct neighbors of a cell. One boundary exchange is done as follows.

Let there be a process p_{qrs}, $(q,r,s) \in \{0..P_x-1\} \times \{0..P_y-1\} \times \{0..P_z-1\}$ holding a subgrid $\mathcal{G}_{qrs} := \{-2...l_x+1\} \times \{-2...l_y+1\} \times \{-2...l_z+1\}$ with $l_\alpha = n_\alpha / P_\alpha$. This process sends data to its left neighbor in x direction, $p_{q-1,r,s}$, by

(1) writing the subset $\{0...1\} \times \{-2...l_y+1\} \times \{-2...l_z+1\}$ into a buffer
(2) submitting the buffer to process $p_{q-1,r,s}$
(3) within process $p_{q-1,r,s}$, writing the buffer contents into the subset $\{l_x..l_x+1\} \times \{-2...l_y+1\} \times \{-2...l_z+1\}$.

This procedure is followed by each process for each of the 6 main spatial directions. The outer grid information of neighboring processes has now been made available for p_{qrs} as boundary conditions for stencil operators. The exchange routine must be executed after each substep of the EM solver.

Exchange of the macroparticles in done in a similar way. A particle is said to have moved out of the processes' subdomain if, after one movement step, it resides in the outer region of the subgrid. This means, that is has left the region $\{0...l_x-1\} \times \{0...l_y-1\} \times \{0...l_z-1\}$. After the particle move step, each particle for which this is true, is removed from the subgrid and put into a buffer in order to be sent to the adjacent process.

3.9. Assembling the components / Summary and outlook

In the subsections before, the basic components for a self-consistent, relativistic, energy- and charge-conserving electromagnetic particle-in-cell simulation code have been described. According to figure 3.9.1, these form the fundamental computational cycle passed within each time step.

Similar to most other simulation codes, the Virtual Laser Plasma Laboratory (VLPL) PIC code also contains a parsing system for simulation job files (".ini files"), a versatile data storage module based on the Hierarchical Data Format (HDF5) standard, and several initialization modules for simulation setup. Additionally,

there are filtering algorithms for fields, the alternative Numerical Dispersion Free (NDF) Maxwell solver, and a variety of diagnosis and in-process control routines included.

Within the very elaborate PIC technique, there are various useful extensions to the algorithm which can be thought of. Some of them have been developed and implemented, and will be introduced, in this thesis. Others can be regarded as promising enhancements in future projects. In this chapter, a short overview of available concepts will be given, which, of course, cannot make any claim to be complete.

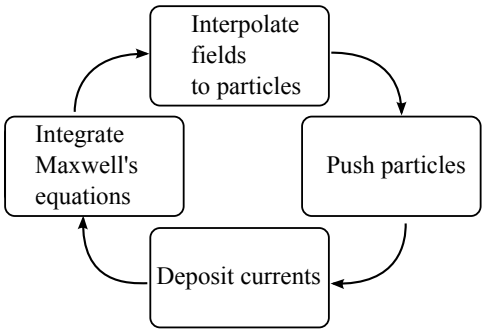

FIGURE 3.9.1. Basic computational cycle of a self-consistent PIC code

First of all, **alternative field solvers** can be implemented based on different numerical schemes. E.g., the Finite Difference Time Domain - Alternating Direction Implicit (FDTD-ADI) [**53**] scheme employs a semi-implicit time discretization, causing tri-diagonal linear equations systems to solve. This way, it becomes unconditionally stable - the time step is no longer restricted by the grid steps. If the electromagnetic phenomena involved have low characteristic frequencies, but fine features to be resolved, such a scheme can provide significant speed-up. This scheme has been implemented into the code.

In many simulation problems, there is a great demand for **absorbing boundary conditions**. Boundary conditions in the VLPL code can assume the grid functions only to be periodic or zero outside of the simulation box. Hence, there is a priori no way to simulate a laser pulse leaving the simulation domain. This problem can be solved with the perfectly matched layer technique [**54**], where additional absorbing layers are wrapped around the simulation box. Within these layers, Maxwell's equations are modified, such that incident waves become attenuated. This scheme has also been implemented, in the form of the Convolutional PML (CPML) [**55**] algorithm.

Furthermore, the investigation of ultra-short pulse induced laser plasma effects needs special **electromagnetic pulse representations**. Initializing a laser pulse as a product of a sine with a shape function is often insufficient. Such schemes, which produce a focusable pulse truly satisfying Maxwell's equations without diverging, have been developed and implemented by Daniel an der Brügge [**56**].

Adaptive Mesh refinement can prove to be worthwhile whenever a physical setup contains fine spatial features to be resolved, but large regions with very homogeneous behaviour. Usually, one would then be forced to resolve those fine features with the equidistant grid, causing large computational load. On the other hand, the fine resolution is just unnecessary in the 'boring' regions, so subdividing grid cells into smaller ones can provide significant speed-up.

CHAPTER 4

Principles of Computational Fluid Dynamics

In chapter 3, the PIC method, one of the most important concepts of computational plasma research, was presented. Despite its physical richness, and its capability of modeling highly nonlinear plasma effects, it has certain shortcomings, like its high cost and intrinsic numerical noise. Also, there is a variety of problems where kinetic modeling is not necessary, or not advisable. One of the most prominent alternatives is the wide field of Computational Fluid Dynamics (CFD). Since a major part of this work is dedicated to the development of a PIC/Fluid hybrid code, some basic principles of CFD need to be introduced.

4.1. Introduction

From a physical point of view, a fluid is a material whose components are not rigidly connected to each other, like in solids. While solids can be deformed permanently through forces, the shape of a fluid changes due to velocity fields. Examples for fluids are gases, liquids and -the reason why this chapter is included here- plasmas. In the introductory section 2.2, the first two momenta of Vlasov's equation have been derived. While computing the moments of the Vlasov equation, one notices that each of them contains a term dependent on the next higher momentum. Fortunately, this chain can be ended by introducing a closure relation, e.g. a gas dynamics law.

By adding a conservation law for the energy density, we obtain the well-known Euler equations:

$$\frac{\partial}{\partial t}\rho = -\nabla \cdot (\rho \mathbf{v}) \tag{4.1.1}$$

$$\frac{\partial}{\partial t}(\rho \mathbf{v}) = -\nabla \cdot (\rho \mathbf{v}\mathbf{v}^T) - \frac{1}{m}\nabla p \tag{4.1.2}$$

$$\frac{\partial}{\partial t}E = -\nabla \cdot ((E+p)\,\mathbf{v}) \tag{4.1.3}$$

The electromagnetic forces have been put away for brevity; they will be reintroduced later. Here, ρ denotes the number density of a respective particle species, $\rho\mathbf{v}$ is its velocity density, m is one particles' mass, and p is the pressure. The variable E stands for the energy density, which is the sum

$$E = \frac{1}{2}\rho\mathbf{v}^2 + \rho\epsilon$$

of the kinetic energy density $\frac{1}{2}\rho\mathbf{v}^2$ related to the average velocity and the internal energy $\rho\epsilon$. Because of the closure problem mentioned above, we need an approximation which relates the unknown pressure p to the other variables. For a calorically

ideal gas, it holds

$$\begin{aligned}\epsilon =& \frac{p}{\rho\left(\gamma-1\right)}\\ \Leftrightarrow p =& \epsilon\rho\left(\gamma-1\right)\\ =& \left(E-\frac{1}{2}\rho\mathbf{v}^2\right)\left(\gamma-1\right).\end{aligned}$$

The Euler equations (4.1.1)-(4.1.3) describe the behaviour of compressible, inviscid fluids, like gases. As previously mentioned, they are *conservation laws*: They predict the evolution of densities whose overall integral is constant. As previously mentioned in chapter 2.1, conservation laws take the form

$$\frac{\partial}{\partial t}U+\nabla\cdot F\left(U\right)=0.$$

Integrating over a measurable set $M\in\mathbb{R}^3$ and using Gauss' Law yields

$$\begin{aligned}\frac{\partial}{\partial t}\int\limits_M U d\lambda =& -\int\limits_M \nabla\cdot F\left(U\right)d\lambda\\ =& -\int\limits_{\partial M} F\left(U\right)d\lambda.\end{aligned}\tag{4.1.4}$$

This means that the total amount of the quantity related to U inside M changes according to the flux on the surface.

For a long time, the Euler equations themselves were not that important for hydrodynamic research. They could only be solved for a few special cases. Instead, approximations and simplified variants were relied upon. With the advent of increasingly powerful computers however, it became possible to directly apply the basic fluid laws on problems.

In the second half of the twentieth century, Computational Fluid Dynamics emerged as a versatile and potent tool for the investigation of a huge number of problems in physics, chemistry, and engineering. Its fields of application include predicting streamlines around an airfoil or the development of optimal shaping of ships, aircraft, helicopters, automobiles and submarines. Methods of CFD are applied on radiation transport, heat transport, magnetohydrodynamics in tokamaks, and many more.

In the time of its evolution, CFD research has used a number of variants of the fluid equations. These include the Navier-Stokes equations for viscous fluids, steady-state and incompressible fluid equations, Full Potential equations (for fluids where the assumptions $\nabla\cdot\mathbf{v}=0$ and $\nabla\times\mathbf{v}=0$ hold), and equations with gravitational and electromagnetic terms.

The methods used in the fields are also manifold. Among the oldest discretization schemes are **Finite Difference Methods** (FDM), which apply stencil operations on (mostly one-dimensional) grids, but have lost much importance compared to more modern methods. **Finite Volume Methods** (FVM) make use of the relation (4.1.4); such schemes can be characterized solely by their specific flux approximation. They can be easily formulated on non-rectangular grids and are widely used in many commercial CFD codes. The most sophisticated discretizations are

Finite Element Methods (FEM), which define basis functions on the cells, transform the fluid equations into weak formulations, and solve equation systems for the coefficients.

In the next chapters, concepts from CFD will be used for the modeling of wake fields. Since, in the VLPL code's field of plasma research, the plasma particles interact only collectively through fields (at most enhanced with collision terms), we do not need the Navier-Stokes equations. Furthermore, FDM schemes are not versatile enough for our 3D simulations, while FEMs are too costly. Thus, the next chapters will focus on Finite Volume Methods.

Conservation laws like Euler's equation belong to the family of hyperbolic partial differential equations. They are rather difficult to solve - throughout its history, CFD research has also seen a number of setbacks. Mostly, this due to spurious oscillations, the fact that higher order discretizations cause unphysical ripples at sharp borders. Many solutions have been devised for this problem, e.g. Total Variation Diminishing (TVD) (see e.g. [**57, 58**]), Essentially Non Oscillatory (ENO), or Flux-Corrected Transport (FCT) [**44**] schemes.

In the next section, the concept of Finite Volume Methods is introduced and explained. In (4.3), higher order extensions to the schemes are discussed.

The next chapters can only give a brief overview about the exhaustive theory of TVD methods and the huge number of fluid schemes available. For further reading, please see [**57, 58**].

4.2. Finite Volume Methods (FVM)

Finite Volume Methods for Euler's equations are widely used in many implementations, particularly for unsteady flows. They can be stable and accurate even in the presence of discontinuities and shocks because they rely on integral formulations. Let there be a three-dimensional conservation law

$$\frac{\partial}{\partial t}\mathbf{U} + \nabla \cdot \mathbf{F}(\mathbf{U}) = 0, \tag{4.2.1}$$

with $\mathbf{U} : D \times [0, T[\to \mathbb{R}^d$, $D \subset \mathbb{R}^3$, $\mathbf{F} : \mathbb{R}^d \to \mathbb{R}^{3\times d}$. Here, D is the simulation domain, $\mathbf{U}(\mathbf{x}, t)$ is the vector of hydrodynamic variables at a certain location $\mathbf{x}$ and time t, $\mathbf{F} = (F_x, F_y, F_z)^T$ is the flux function and

$$(\nabla \cdot \mathbf{F}(\mathbf{U}))_i := \sum_{k=1}^{3} \frac{\partial}{\partial x_k} \mathbf{F}(\mathbf{U})_{k,i}$$

is meant as a columns-wise divergence. $T \in \mathbb{R}$ is the simulation time. From (4.1.4), we already know

$$\frac{\partial}{\partial t} \int_M \mathbf{U} d\lambda = - \int_{\partial M} \mathbf{F}(\mathbf{U})\, d\lambda.$$

This immediately suggests to define discretized variables as integral averages rather than point values. Analogously to what has been done in 3.2, we define a grid

$$\mathcal{G} := \{0...n_x - 1\} \times \{0...n_y - 1\} \times \{0...n_z - 1\} \subset \mathbb{Z}^3,$$

with grid cells

$$\mathcal{C} := \{c_{ijk} = [i\Delta x, (i+1)\Delta x[\times [j\Delta y, (j+1)\Delta y[\times [k\Delta z, (k+1)\Delta z[: (i,j,k) \in \mathcal{G}\}.$$

Although FVMs can also be defined on non-rectangular grids, we choose a rectangular mesh here with regard to a later implementation into the existing, rectangular, VLPL code. The discretized fluid variables are then defined as

$$\mathbf{U}_{i+\frac{1}{2},j+\frac{1}{2},k+\frac{1}{2}}(t) := \frac{1}{\lambda(c_{ijk})} \int\limits_{c_{ijk}} \mathbf{U}(\mathbf{x},t)\, dx^3,$$

the Lebesgue integral average over the grid cell c_{ijk}. The essence of Finite Volume Methods is to find a flux approximation

$$\begin{aligned}
\frac{1}{\Delta y \Delta z} \int\limits_{j\Delta y}^{(j+1)\Delta y} \int\limits_{k\Delta z}^{(k+1)\Delta z} F_x(\mathbf{U})\, dzdy &\approx f_{x,i,j+\frac{1}{2},k+\frac{1}{2}}, \\
\frac{1}{\Delta z \Delta x} \int\limits_{k\Delta z}^{(k+1)\Delta z} \int\limits_{i\Delta x}^{(i+1)\Delta x} F_y(\mathbf{U})\, dxdz &\approx f_{y,i+\frac{1}{2},j,k+\frac{1}{2}}, \\
\frac{1}{\Delta x \Delta y} \int\limits_{i\Delta x}^{(i+1)\Delta x} \int\limits_{j\Delta y}^{(j+1)\Delta y} F_z(\mathbf{U})\, dydx &\approx f_{z,i+\frac{1}{2},j+\frac{1}{2},k}.
\end{aligned}$$

The semi-discretized version of the conservation law (4.2.1) then simply reads

$$\begin{aligned}
\frac{d}{dt}\mathbf{U}_{i+\frac{1}{2},j+\frac{1}{2},k+\frac{1}{2}} &= -\tilde{\nabla}\cdot\mathbf{f}(\mathbf{U}) \\
&= -\frac{\left(f_{x,\,i+1,j+\frac{1}{2},k+\frac{1}{2}} - f_{x,\,i,j+\frac{1}{2},k+\frac{1}{2}}\right)}{\Delta x} \\
&\quad -\frac{\left(f_{y,\,i+\frac{1}{2},j+1,k+\frac{1}{2}} - f_{y,\,i+\frac{1}{2},j,k+\frac{1}{2}}\right)}{\Delta y} \\
&\quad -\frac{\left(f_{z,\,i+\frac{1}{2},j+\frac{1}{2},k+1} - f_{z,\,i+\frac{1}{2},j+\frac{1}{2},k}\right)}{\Delta z}.
\end{aligned}$$

It can be easily seen that this form of a spatial discretization is always conservative, i.e.

$$\sum_{(i,j,k)\in\mathcal{G}} \mathbf{U}_{i+\frac{1}{2},j+\frac{1}{2},k+\frac{1}{2}} = \text{const},$$

provided that the boundary conditions are periodic or the boundary fluxes are zero. This crucial advantage against finite difference formulations will gain even more importance in the later hybrid implementation: Poisson's law can then be satisfied in a straightforward way.

There are plenty of such flux approximations available. A common approach is to find a flux scheme in order to obtain the semi-discretized equations (4.2.1), and apply standard ODE solvers, like Runge-Kutta methods, afterwards. This concept is also called the method of lines and has proven to be very effective in practice.

It should however be mentioned that the design of such flux schemes is not trivial. Let us briefly look at a common example for this, which involves the simple one-dimensional conservation law

$$\left(\frac{\partial}{\partial t} + a\frac{\partial}{\partial x}\right) u(x,t) = 0,\ a \in \mathbb{R}. \tag{4.2.2}$$

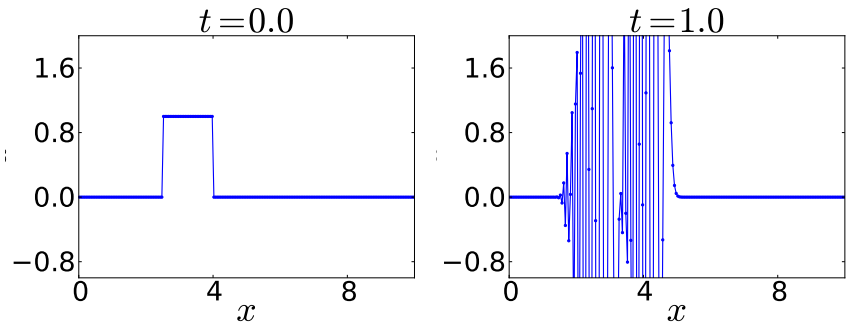

FIGURE 4.2.2. Result of a short simulation after $t = 0$ and $t = 1$ with the scheme (4.2.3). This unconditionally unstable solver quickly amplifies high-frequency modes.

Given an initial state $u(x, t = 0) =: u_0(x)$, the solution is $u(x, t) = u_0(x - at)$, which means that (4.2.2) is just a simple linear transport equation. Let us now try to discretize it. The spatially discretized variable shall be

$$u_{i+\frac{1}{2}}(t) := \frac{1}{\Delta x} \int_{i\Delta x}^{(i+1)\Delta x} u(x, t)\, dx,$$

so the semi-discrete form is

$$\frac{d}{dt} u_{i+\frac{1}{2}}(t) = -\frac{1}{\Delta x}(f_{i+1} - f_i).$$

Naively, one might choose the second order flux scheme

$$f_i := \frac{a}{2}\left(u_{i+\frac{1}{2}} + u_{i-\frac{1}{2}}\right),$$

and try the explicit Euler method for the time evolution. One gets

$$u^{n+1}_{i+\frac{1}{2}} = u^n_{i+\frac{1}{2}} - \frac{\Delta t}{\Delta x}\frac{a}{2}\left(u_{i+\frac{3}{2}} - u_{i-\frac{1}{2}}\right). \tag{4.2.3}$$

With Von Neumann stability analysis it can be seen that this scheme is unconditionally unstable. A result obtained with this solver is depicted in fig. 4.2.2, showing a rapid explosion.

The reason for this behaviour lies in the spatial discretization scheme. On smooth solutions, the scheme works fairly accurate, but it tends to enlarge high-frequency modes. Related to this is its incapability of modeling sharp edges. This can be overcome by adding diffusive fluxes or using asymmetric fluxes, whose directions depend on the velocity a:

$$f_j := a u_{i-\frac{1}{2}} \tag{4.2.4}$$

$$u^{n+1}_{i+\frac{1}{2}} = u^n_{i+\frac{1}{2}} - \frac{\Delta t}{\Delta x} a\left(u_{i+\frac{1}{2}} - u_{i-\frac{1}{2}}\right), \tag{4.2.5}$$

for $a > 0$. Equation (4.2.5) is called the upwind scheme, and again combined with an explicit Euler time integrator. The results for the scheme (4.2.5), applied on the problem (4.2.2) are shown in fig. (4.2.3). For $\Delta t \leq \Delta x/a$ it is stable, but restricted to first order accuracy. Here, the numerical error takes the form of an artificial diffusion.

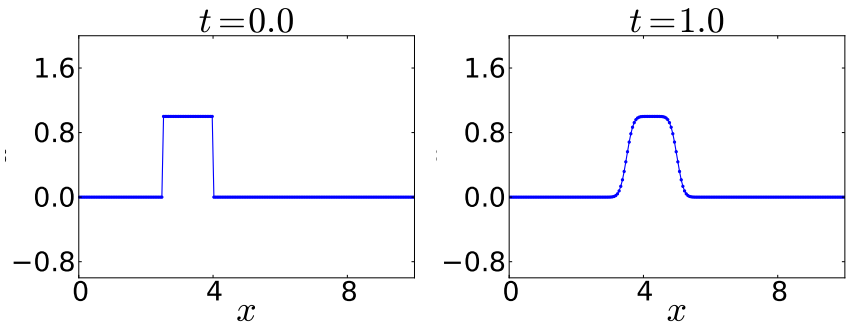

FIGURE 4.2.3. Result of a short simulation after $t = 0$ and $t = 1$ with the scheme (4.2.5). This solver is stable, but achieves only 1st order accuracy and causes a numerical diffusion.

One might wonder now how to obtain high-order flux schemes which are stable and do not suffer from spurious oscillations. It turns out that most linear spatial discretizations of high order behave similarly here. To make things worse, there is Godunov's theorem, which states:

Any linear numerical scheme for a partial differential equation, which does not introduce new extrema to the solution is at most first-order accurate.

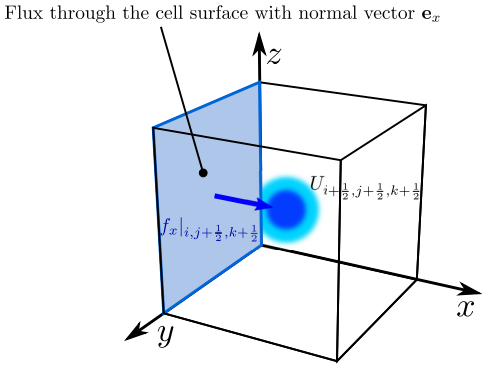

FIGURE 4.2.1. Sketch of a grid cell for an FVM scheme. The integral averaged variable $\mathbf{U}_{i+\frac{1}{2},j+\frac{1}{2},k+\frac{1}{2}}$ changes according to the surface fluxes $f_{i,j+\frac{1}{2},k+\frac{1}{2}}$ etc.

Godunov published the proof for this theorem in 1959. At the first glance, it is discouraging. However, it can be circumvented as it only describes the properties of linear schemes. Hence, a working method must always be non-linear; to be more precise, it must adapt in some way to the local structure of the solution. In the next section, two important approaches to the problem will be demonstrated.

4.3. High-resolution spatial schemes

4.3.1. Total Variation Diminishing (TVD) methods and flux limiting. From the last chapter it is obvious that the attempt to construct high-order Finite Volume Discretizations has a substantial problem: Linear schemes of more than first order will always fail in the presence of shocks and sharp borders. Their typical behaviour is demonstrated in fig. 4.3.1. Whenever the assumption of differentiability does not hold at some point in the initial condition, the schemes cause under- and overshoots. This effect is related to Runge's phenomenon present in

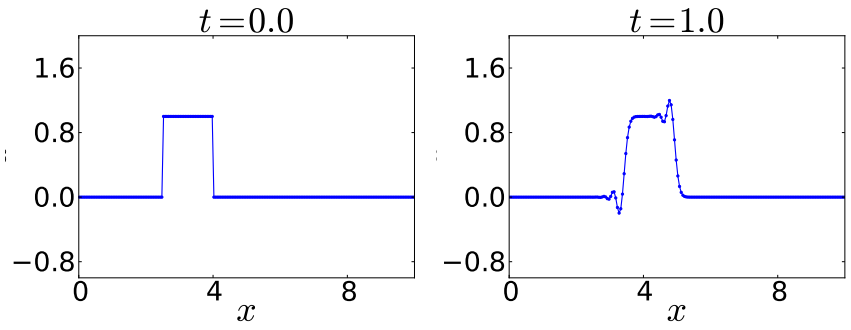

FIGURE 4.3.1. Result of a simple simulation using the Lax-Wendroff fluid scheme. Although the scheme is stable, it cannot handle shocks and sharp borders, causing spurious oscillations here.

interpolation, and is usually referred to as spurious oscillations. In the best cases, these schemes can still be quite useful - in the worst case, they are unstable, like the scheme (4.2.3).

A central task of FVM research was, and still is to put together these two seemingly contradicting features: High accuracy and the absence of spurious oscillations. Since Godunov's theorem tells us that this is not possible for linear schemes, one must find non-linear adaptive ones.

First, we need a formal definition as close as possible to "spurious oscillation-free". There are two conditions which have proven to be extremely useful, namely the *preservation of monotonicity* and the *Total Variation Diminishing (TVD)* feature.

DEFINITION 1. Monotonicity preserving scheme

A numerical scheme is called monotonicity preserving if for every non-decreasing (or non-increasing) initial state $\left[\varphi_j^0\right]_{j=0}^{N-1}$, the advanced state $\left[\varphi_j^1\right]_{j=0}^{N-1}$ is also non-decreasing (non-increasing) in space.

Godunov's order barrier theorem can be formulated for this condition:

THEOREM 2. *Godunov's order barrier theorem*

A linear one-step second order numerical scheme for the transport equation(4.2.2) cannot be monotonicity preserving, unless $|a|\Delta t/h \in \mathbb{N}$.

The proof can be found in various text books, e.g. **[57, 58]**. Of course, the "magical" time step where $|c|\Delta t/h = 1$ does not alleviate the problem, since a varies in realistic applications. Another important concept is the Total Variation:

DEFINITION 3. Total Variation

The total variation (TV) of a function $\varphi : \mathbb{R} \to \mathbb{R}$ is defined as

$$TV\left(\varphi(t,\cdot)\right) = \limsup_{\epsilon \to 0} \frac{1}{\epsilon} \int_{-\infty}^{\infty} \left|\varphi\left(t,x\right) - \varphi\left(t,x-\epsilon\right)\right| dx.$$

It can be easily seen that the exact solution of (4.2.2), $\varphi(t,x) = \varphi_0(x-ct)$, keeps the total variation constant, because

$$TV(\varphi(t,\cdot) = \limsup_{\epsilon\to 0} \frac{1}{\epsilon} \int_{-\infty}^{\infty} |\varphi_0(x-ct) - \varphi(0, x-ct-\epsilon)| dx = TV(\varphi_0).$$

DEFINITION 4. Discrete Total Variation
For a numerical solution $\left[\varphi_j^n\right]_{j=-\infty}^{\infty}$, the total variation is

$$TV(\varphi^n) = \sum_{j=-\infty}^{\infty} |\varphi_j^n - \varphi_{j-1}^n|.$$

A scheme is called Total Variation Diminishing (TVD), if the total variation of the solutions decreases with time,

$$TV\left(\varphi^{n+1}\right) \leq TV(\varphi^n).$$

Likewise, the solution to a conservation law is called TVD if the continuous total variation decreases with time.

It can be shown that the weak solution of a general conservation law

$$\frac{\partial}{\partial t}\varphi + \frac{\partial}{\partial x} f(\varphi) = 0,$$

made unique via additional entropy conditions, is TVD. At the same time, a numerical scheme which causes spurious oscillations clearly increases the total variation of the solution. This is why one tries to find schemes with the TVD property. There is a great number of methods available having this property, e.g. Riemann solvers like Godunovs method, the upwind scheme or central schemes with artifial diffusion terms.

With the TVD criterion at one's disposal, it is also possible to construct higher order schemes. In some cases one can simply employ high-order interpolation schemes for the border fluxes. Another widely used approach is called Monotone Upstream-centered Schemes for Conservation Laws (MUSCL) [**41**]. Here, one replaces the piecewise constant input data for a Riemann solver by reconstructed states. These modified reconstructed data are then fed into a Riemann solver or similar scheme, in order to obtain a flux approximation. Such a scheme provides greater accuracy in regions where the solution is smooth. It is then usually made TVD by introducing *limiter functions*, either in the form of *slope limiters* or *flux limiters*.

At this point, the details of TVD high-resolution schemes shall be omitted. Instead, we depict the Flux-corrected transport (FCT) algorithm, which serves a similar purpose and has been used in the H-VLPL3D PIC/fluid implementation.

4.3.2. Flux-corrected transport (FCT). Instead of enforcing the TVD (or a similar) condition on the solution, one can also prevent the formation of new extrema directly. This concept has been followed in the FCT [**44**] method. This procedure has proven to be very robust and less restrictive than many TVD methods tested. Its main advantage lies in the fact that, once implemented, it can be used as a closed module. While slope limiters must sometimes be adapted to the respective scheme, one can freely and easily feed various flux approximations into the FCT procedure.

One starts with the state at time $n\Delta t$, $u^n_{i+\frac{1}{2},j+\frac{1}{2},k+\frac{1}{2}}$, a "trusted" low order flux $\mathbf{F}^L$ and a high order flux $\mathbf{F}^H$, looking closely at the local structure of the solution at a given position $(i,j,k) \in \mathcal{G}$. From the low order flux one must be sure that it does not introduce spurious oscillations, which is easy to achieve with a great number of first order upwind schemes.

In the first step, a "trusted" update $u^{td}_{i+\frac{1}{2},j+\frac{1}{2},k+\frac{1}{2}}$ is computed using the flux $\mathbf{F}^L$; in the second step, we define the "antidiffusive flux"

$$\mathbf{A} := \mathbf{F}^H - \mathbf{F}^L.$$

Over- and undershoots are prevented by limiting the "anti-diffusive" flux $\mathbf{F}^H - \mathbf{F}^L$ in a way that the updated solution

$$u^{n+1}_{i+\frac{1}{2},j+\frac{1}{2},k+\frac{1}{2}} = u^n_{i+\frac{1}{2},j+\frac{1}{2},k+\frac{1}{2}} - \left(\tilde{\nabla} \cdot \mathbf{F}^{FCT}\right)_{i+\frac{1}{2},j+\frac{1}{2},k+\frac{1}{2}}$$

stays within pre-defined limits

$$\left[u^{\min}_{i+\frac{1}{2},j+\frac{1}{2},k+\frac{1}{2}}, u^{\max}_{i+\frac{1}{2},j+\frac{1}{2},k+\frac{1}{2}}\right].$$

The latter can be defined in various ways. One common choice is shown in algorithm 1, which is taken from [**44**]. It gives a moderately restrictive limiter, by computing its $u^{\max}_{i+\frac{1}{2},j+\frac{1}{2},k+\frac{1}{2}}$ value out of all neighboring points of the initial state u^n and the trusted solution u^{td}.

In the fourth step, we compute the sums of all antidiffusive fluxes going into, and out of, the cell. It can be easily seen that by replacing the antidiffusive flux by

$$A^{\text{limit}}_{x,i,\,j+\frac{1}{2},} := A_{x,\,i,j+\frac{1}{2},k+\frac{1}{2}} C_{x,\,i,j+\frac{1}{2},k+\frac{1}{2}} \text{ etc.},$$

where the coefficients

$$C_{x,\,i,j+\frac{1}{2},k+\frac{1}{2}},\, C_{y,\,i+\frac{1}{2},j,k+\frac{1}{2}} ... \in [0,1]$$

are computed according to algorithm 1, the updated solution

$$u^{n+1} = u^{td} - \left(\tilde{\nabla} \cdot \mathbf{A}^{\text{limit}}\right)_{i+\frac{1}{2},j+\frac{1}{2},k+\frac{1}{2}}$$

stays below $u^{\max}$ and above $u^{\min}$.

Algorithm 1 The flux-corrected transport (FCT) algorithm. Before execution, it needs the initial value of the variable to be updated, $u^n_{i+\frac{1}{2},j+\frac{1}{2},k+\frac{1}{2}}$, the high and low order cell flux approximations $\mathbf{F}^H$and $\mathbf{F}^L$, the grid steps $\Delta x, \Delta y, \Delta z$ and the time step Δt. It provides as output the coefficients $\left(C_{x,i,j+\frac{1}{2},k+\frac{1}{2}}, C_{y,i+\frac{1}{2},j,k+\frac{1}{2}}, C_{z,i+\frac{1}{2},j+\frac{1}{2},k}\right)_{(i,j,k)\in\mathcal{G}}$ for the limited flux $F^{FCT}_{x,i,j+\frac{1}{2},k+\frac{1}{2}} = F^L_{x,i,j+\frac{1}{2},k+\frac{1}{2}} + \left(F^H_{x,i,j+\frac{1}{2},k+\frac{1}{2}} - F^L_{x,i,j+\frac{1}{2},k+\frac{1}{2}}\right) C_{x,i,j+\frac{1}{2},k+\frac{1}{2}}$.

(1) Compute a trusted low order solution

$$u^{td}_{i+\frac{1}{2},j+\frac{1}{2},k+\frac{1}{2}} = u^n_{i+\frac{1}{2},j+\frac{1}{2},k+\frac{1}{2}} - \Delta t \left(\tilde{\nabla}\cdot\mathbf{F}^L\right)_{i+\frac{1}{2},j+\frac{1}{2},k+\frac{1}{2}}.$$

(2) Define the antidiffusive flux

$$\mathbf{A} := \mathbf{F}^H - \mathbf{F}^L.$$

(3) Define the minimum and maximum values

$$\begin{aligned}
u_{a,i+\frac{1}{2},j+\frac{1}{2},k+\frac{1}{2}} &:= \max\left(u^n_{i+\frac{1}{2},j+\frac{1}{2},k+\frac{1}{2}}, u^{td}_{i+\frac{1}{2},j+\frac{1}{2},k+\frac{1}{2}}\right),\\
u_{b,i+\frac{1}{2},j+\frac{1}{2},k+\frac{1}{2}} &:= \min\left(u^n_{i+\frac{1}{2},j+\frac{1}{2},k+\frac{1}{2}}, u^{td}_{i+\frac{1}{2},j+\frac{1}{2},k+\frac{1}{2}}\right)\\
u^{\max}_{i+\frac{1}{2},j+\frac{1}{2},k+\frac{1}{2}} &= \max_{\alpha,\beta,\gamma\in\mathbb{Z},|\alpha|+|\beta|+|\gamma|\le 1}\left(u_{a,i+\frac{1}{2}+\alpha,j+\frac{1}{2}+\beta,k+\frac{1}{2}+\gamma}\right)\\
u^{\min}_{i+\frac{1}{2},j+\frac{1}{2},k+\frac{1}{2}} &= \min_{\alpha,\beta,\gamma\in\mathbb{Z},|\alpha|+|\beta|+|\gamma|\le 1}\left(u_{b,i+\frac{1}{2}+\alpha,j+\frac{1}{2}+\beta,k+\frac{1}{2}+\gamma}\right)
\end{aligned}$$

(4) Set the sum of all antidiffusive fluxes into grid cell $[i,i+1[\times[j,j+1[\times[k,k+1[$,

$$\begin{aligned}
P^+_{ijk} &= \frac{\Delta t}{\Delta x}\left[\max\left(0,\, A_{x,i,j+\frac{1}{2},k+\frac{1}{2}}\right) - \min\left(0,\, A_{x,i+1,j+\frac{1}{2},k+\frac{1}{2}}\right)\right]\\
&+ \frac{\Delta t}{\Delta y}\left[\max\left(0,\, A_{y,i+\frac{1}{2},\,j,\,k+\frac{1}{2}}\right) - \min\left(0,\, A_{y,i+\frac{1}{2},\,j+1,\,k+\frac{1}{2}}\right)\right]\\
&+ \frac{\Delta t}{\Delta z}\left[\max\left(0,\, A_{z,i+\frac{1}{2},\,j+\frac{1}{2},\,k}\right) - \min\left(0,\, A_{z,i+\frac{1}{2},\,j+\frac{1}{2},\,k+1}\right)\right]
\end{aligned}$$

along with

$$\begin{aligned}
Q^+_{ijk} &= \left(u^{\max}_{i+\frac{1}{2},j+\frac{1}{2},k+\frac{1}{2}} - u^{td}_{i+\frac{1}{2},j+\frac{1}{2},k+\frac{1}{2}}\right),\\
R^+_{ijk} &= \begin{cases}\min\left(1,\, Q^+_{ijk}/P^+_{ijk}\right) & \text{if } P^+_{ijk} > 0\\ 0 & \text{if } P^+_{ijk} = 0.\end{cases}
\end{aligned}$$

(5) Set the sum of all antidiffusive fluxes away from grid cell $[i,i+1[\times[j,j+1[\times[k,k+1[$,

$$\begin{aligned}
P^-_{ijk} &= \frac{\Delta t}{\Delta x}\left[\max\left(0,\, A_{x,i+1,j+\frac{1}{2},k+\frac{1}{2}}\right) - \min\left(0,\, A_{x,i,j+\frac{1}{2},k+\frac{1}{2}}\right)\right]\\
&+ \frac{\Delta t}{\Delta y}\left[\max\left(0,\, A_{y,i+\frac{1}{2},\,j+1,\,k+\frac{1}{2}}\right) - \min\left(0,\, A_{y,i+\frac{1}{2},\,j,\,k+\frac{1}{2}}\right)\right]\\
&+ \frac{\Delta t}{\Delta z}\left[\max\left(0,\, A_{z,i+\frac{1}{2},\,j+\frac{1}{2},\,k+1}\right) - \min\left(0,\, A_{z,i+\frac{1}{2},\,j+\frac{1}{2},\,k}\right)\right]
\end{aligned}$$

along with

$$\begin{aligned}
Q^-_{ijk} &= \left(u^{td}_{i+\frac{1}{2},j+\frac{1}{2},k+\frac{1}{2}} - u^{\min}_{i+\frac{1}{2},j+\frac{1}{2},k+\frac{1}{2}}\right),\\
R^-_{ijk} &= \begin{cases}\min\left(1,\, Q^-_{ijk}/P^-_{ijk}\right) & \text{if } P^-_{ijk} > 0\\ 0 & \text{if } P^-_{ijk} = 0.\end{cases}
\end{aligned}$$

(6) Determine the coefficients for the flux convex combination

$$C_{x,i,j+\frac{1}{2},k+\frac{1}{2}} = \begin{cases}\min\left(R^+_{i,j,k}, R^-_{i-1,j,k}\right) & \text{if } A_{x,i,j+\frac{1}{2},k+\frac{1}{2}} \ge 0\\ \min\left(R^+_{i-1,j,k}, R^-_{i,j,k}\right) & \text{if } A_{x,i,j+\frac{1}{2},k+\frac{1}{2}} < 0\end{cases},$$

with cyclically permuted indices for the other two components.

CHAPTER 5

Exponential integrator for highly overdense plasma simulations

5.1. Introduction

The particle-in-cell method is by far the most widely used, and most important method for investigating the rich field of laser-plasma and plasma-plasma interaction. It works for a broad parameter regime, and has contributed significantly to our understanding of this complex research area.

However, there is a number of unpleasant technical restrictions to its applicability. These are e.g. its high computational cost, its grid-related limitations (Non-adaptive, boundary conditions), and, maybe most important, its various stability conditions. Possible extensions to the algorithm have already been mentioned in chapter 3.9. An important stability condition for electromagnetic material simulations like PIC is the one related to plasma oscillations, i.e.

$$\Delta t \leq \frac{2}{\omega_p},$$

where $\omega_p = \sqrt{4\pi e^2 n_e / m_e}$ is the (local) plasma frequency, n_e is the electron number density and m_e is the electron rest mass. While for laser-gas interaction simulations, it almost never becomes important, it causes severe time step restrictions if materials of solid-state density are involved.

There is a variety of physical mechanisms which involve such high densities, e.g. Target Normal Sheath Acceleration (TNSA) [**36**], the Fast Ignition scheme in inertial confinement fusion [**59**], or generation of high harmonics on solid-state surfaces [**60**]. Here, conventional PIC simulations can be become extremely costly: The time step must be adjusted according to the stability condition, but lowering the grid steps might also be necessary if numerical dispersion is an issue. One could ask here if this waste of computational resources can be circumvented somehow.

As a brief excursus, we take a look on the TNSA process, which is a candidate for laser-based ion acceleration. A few fs-short laser pulse with a_0 about 2 is incident on a foil target. The target consists of a bulk part with $n_e \approx 1000\, n_c$, a pre-plasma of about $1.5\mu m$ length, and a thin proton layer on its back surface.

The laser pulse hits the pre-plasma, creating a blow-off region in front of the foil. This results in a large cloud of hot electrons, which, partly, propagates through the foil and passes the coating of the back surface. As the electrons leave the surface, a strong electrostatic field is built up, and the protons are pulled out of the foil and eventually accelerated to high energies.

Looking closely on this effect, one notices that the bulk part of the foil is not involved in the mechanism. The pre-plasma must be modeled kinetically, as well as

the proton layer, but the contribution of the middle region can be understood just by its linear electrostatic response.

This gives rise to the idea of implementing a *hybrid code*, where the plasma can be modeled with two distinct numerical methods. First, the conventional PIC algorithm, which will simulate the hot, low density particles. Second, a fluid model, which, although resembling a strong simplification, does not suffer from any plasma frequency-related stability conditions.

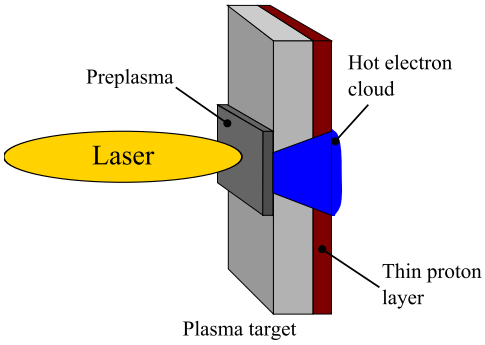

FIGURE 5.1.1. Sketch of the Target Normal Sheath Acceleration

In last years PIC-hydrodynamic hybrid techniques have emerged as an efficient solution to large scale ultra high density plasma simulations, e.g., FI physics, solid state density plasma interactions, high energy ion generation etc. Most of these codes work in the Darwin approximation and thus exclude the electromagnetic wave propagation completely. They also exclude electrostatic waves keeping the collisional magnetohydrodynamics (MHD) only. Further, an implicit electrostatic particle-fluid hybrid plasma code has been developed by Rambo and Denavit [**61**], which has been used to study interpenetration and ion separation in colliding plasmas [**62**]. There is also the implicit electromagnetic PIC code LSP [**31**]. This code uses an implicit global scheme which overcomes such restrictions of the time-step. The LSP code also employs a field solver based on an unconditionally Courant-stable algorithm for electromagnetic calculations[**63**]. Recently, we have presented a 1D version of the code Hybrid Virtual Laser Plasma Laboratory (H-VLPL) [**35**] that unites a hydrodynamic model for overdense plasmas and the full kinetic description of hot low-density electrons and ions. In this code, the linear plasma response was simulated using an implicit scheme. The implementation involved the solution of linear systems, which have been done in a very efficient way using the Schur complement.

Since the latter cannot be efficiently generalized to 3D, we propose a different scheme here, which is based on an exponential integrator.

Among the various available techniques for ordinary differential equations (ODEs), exponential integrators constitute an interesting new concept [**64, 65, 66**]. They can be an efficient alternative for ODEs consisting of a highly oscillatory linear and a smooth nonlinear part, like

$$y' = Ay + f(y). \tag{5.1.1}$$

Many classical schemes, like Runge-Kutta or multistep methods, can be generalized to an exponential integrator for (5.1.1). While it becomes necessary to compute matrix-vector products like $\varphi(A)x$, with matrix functions φ, these schemes contain $\|A\|$ neither in their stability conditions nor in their error bounds.

For our problem, we will employ a modified version of the Mollified Impulse method [**67**]. It is a variant of the above mentioned splitting methods, containing

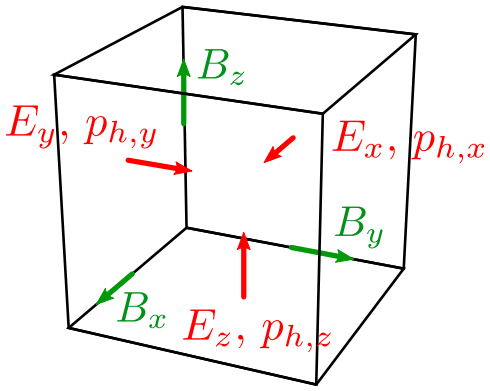

FIGURE 5.2.1. 3D grid cell configuration for the Mollified Impulse hybrid code. The additional fluid momentum $\mathbf{p}_h$ is defined on the same positions as $\mathbf{E}$.

exact solutions also for oscillatory terms. For the formulation used, the high frequencies involved stem from a diagonal linear operator, which means that matrix functions can be easily calculated.

In the next subsections, the basic model for the fluid plasma will be introduced, and the numerical scheme derived. Challenges in the algorithm, as well as their solutions, will be shown. Afterwards, the scheme's correctness shall be demonstrated using error analysis and several physical examples. We will then describe how it has been implemented into the existing VLPL PIC code, and show first results.

5.1.1. Physical model and numerical algorithm. The hybrid concept introduced here will combine an existing PIC algorithm with an additional hydrodynamic model. In this section, the equations of this model as well as the numerical scheme will be shown and discussed.

Since the hydrodynamic model is used for plasmas with a high frequency electrostatic response, we can assume the local momentum amplitudes to be rather low. Likewise, we assume that transport phenomena are negligible. Hence, we modify Maxwell's equations to

$$\frac{\partial}{\partial t}\mathbf{E} = \nabla \times \mathbf{B} - \mathbf{J}^{PIC} - \frac{n_h e}{\gamma_h}\mathbf{p}_h \tag{5.1.2}$$

$$\frac{\partial}{\partial t}\mathbf{B} = -\nabla \times \mathbf{E} \tag{5.1.3}$$

$$\frac{\partial}{\partial t}\mathbf{p}_h = e\mathbf{E}. \tag{5.1.4}$$

Again, we have used dimensionless relativistic units in order to simplify calculations. We denote the local fluid momentum by $\mathbf{p}_h$, the electron charge by e, the fluid density by n_h and its relativistic factor by $\gamma_h := \sqrt{1+\mathbf{p}_h^2}$. As mentioned before, we assume $\mathbf{p}_h$ to stay low and therefore the magnetic lorentz force to be negligible.

5.2. Spatial discretization

Since we want to keep the Yee discretization for $\mathbf{E}$ and $\mathbf{B}$ described in chapter 3.2, we align the fluid momentum $\mathbf{p}_h$ with the Yee grid. Hence, $\mathbf{p}_h$ is defined exactly the same way as $\mathbf{E}$: Each grid cell stores the values

$$\begin{bmatrix} p_{h,x}|_{i,\,j+\frac{1}{2},\,k+\frac{1}{2}} \\ p_{h,y}|_{i+\frac{1}{2},\,j,\,k+\frac{1}{2}} \\ p_{h,z}|_{i+\frac{1}{2},\,j+\frac{1}{2},\,k} \end{bmatrix},$$

as shown in figure 5.2.1. The curl operators do not change, and the fluid current in (5.1.2) as well as the electric force in (5.1.4) are act on the same grid cell. Thus, the semi-discretized equations read

$$\frac{\partial}{\partial t}\mathbf{E} = \tilde{\nabla} \times \mathbf{B} - \mathbf{J}^{PIC} - \frac{n_h e}{\gamma_h}\mathbf{p}_h \tag{5.2.1}$$

$$\frac{\partial}{\partial t}\mathbf{B} = -\tilde{\nabla} \times \mathbf{E} \tag{5.2.2}$$

$$\frac{\partial}{\partial t}\mathbf{p}_h = e\mathbf{E}. \tag{5.2.3}$$

5.3. Time discretization / Splitting

We have now obtained the usual large ordinary differential equation system. One notices that, when neglecting $\mathbf{B}$, and assuming low $\mathbf{p}_h$ such that $\gamma_h = 1$, eqs. (5.1.2) and (5.1.4) form an harmonic oscillator on each grid cell interface. This is where the exponential integrator concept shall be employed. The following considerations are also depicted in [**68**].

Removing the PIC currents for now, we can put the system formally into one vector,

$$\frac{\partial}{\partial t}\begin{bmatrix} \mathbf{E} \\ \mathbf{B} \\ \mathbf{P} \end{bmatrix} = \begin{bmatrix} \tilde{\nabla} \times \mathbf{B} - \omega_h^2 \mathbf{p}_h \\ -\tilde{\nabla} \times \mathbf{E} \\ e\mathbf{E} \end{bmatrix}, \tag{5.3.1}$$

substituting the hydrodynamic plasma frequency $\omega_h^2 = n_h e/\gamma_h$. We recall the method in section 3.2, where Maxwell's equations have been split into two distinct parts. Each of these parts formed a much simpler ODE, which could be solved exactly just by adding the right-hand side. This time, (5.3.1) is split into three different ODEs, namely

$$\frac{\partial}{\partial t}\begin{bmatrix} \mathbf{E} \\ \mathbf{B} \\ \mathbf{P} \end{bmatrix} = \begin{bmatrix} \tilde{\nabla} \times \mathbf{B} \\ 0 \\ 0 \end{bmatrix}, \tag{5.3.2}$$

$$\frac{\partial}{\partial t}\begin{bmatrix} \mathbf{E} \\ \mathbf{B} \\ \mathbf{P} \end{bmatrix} = \begin{bmatrix} 0 \\ -\tilde{\nabla} \times \mathbf{E} \\ 0 \end{bmatrix}, \tag{5.3.3}$$

$$\frac{\partial}{\partial t}\begin{bmatrix} \mathbf{E} \\ \mathbf{B} \\ \mathbf{P} \end{bmatrix} = \begin{bmatrix} -\omega_h^2 \mathbf{p}_h \\ 0 \\ e\mathbf{E} \end{bmatrix}. \tag{5.3.4}$$

If we make the approximation $\gamma_h = 1$, which resembles to the case of a quadratic potential for the oscillatory part, we can write down exact solutions.

Let us denote by φ_t^E the exact flow for the ODE (5.3.2), φ_t^B the one for (5.3.3), and φ_t^h the one for (5.3.4). (For a brief introduction to numerical flows, see section 6.7 or [**48**].) We can construct a splitting scheme as a concatenation of the split exact flows.

$$\varphi_{\Delta t} \approx \varphi^B_{\Delta t/2} \circ \varphi^E_{\Delta t/2} \circ \varphi^h_{\Delta t} \circ \varphi^E_{\Delta t/2} \circ \varphi^B_{\Delta t/2}.$$

Written down as a one-step method, the scheme reads

$$\text{kick: } \mathbf{B}^{n+\frac{1}{2}} = \mathbf{B}^n - \frac{1}{2}\Delta t\tilde{\nabla} \times \mathbf{E}^n \tag{5.3.5}$$

$$\mathbf{E}^+ = \mathbf{E}^n + \frac{1}{2}\Delta t\tilde{\nabla} \times \mathbf{B}^{n+\frac{1}{2}} \tag{5.3.6}$$

$$\text{oscillate: } \begin{bmatrix} \mathbf{p}_h^{n+1} \\ \mathbf{E}' \end{bmatrix} = \begin{bmatrix} \cos\Delta t\omega_h & \Delta t\text{sinc} \\ -\omega_h \sin\Delta t\omega_h & \cos\Delta t\omega_h \end{bmatrix} \begin{bmatrix} \mathbf{p}_h^n \\ \mathbf{E}^+ \end{bmatrix} \tag{5.3.7}$$

$$\mathbf{E}^{n+1} = \mathbf{E}' + \frac{1}{2}\Delta t\tilde{\nabla} \times \mathbf{B}^{n+\frac{1}{2}} \tag{5.3.8}$$

$$\text{kick: } \mathbf{B}^{n+1} = \mathbf{B}^{n+\frac{1}{2}} - \frac{1}{2}\Delta t\tilde{\nabla} \times \mathbf{E}^{n+1}. \tag{5.3.9}$$

It has been shown that this scheme is symmetrical for fixed $\gamma_h = 1$.

This idea of splitting an ordinary differential equation and putting an 'oscillate' step in the middle originates from [**69, 70**]. As a two-term splitting scheme, it is called the *impulse method,* a simple exponential scheme which allows for large time steps independently of ω_h. However, in [**71, 67**] the authors point out that the method exhibits unstable behaviour if the product $\Delta t\omega_h$ is a multiple of π. It turns out that this issue causes problems in our integrator too, and must be adressed.

In order to investigate the correctness of (5.3.5)-(5.3.9), the scheme was reduced to one dimension by setting transversal derivatives to zero and restricting to 1D geometry. A simple laser pulse reflection experiment serves as the test problem:

We define the pulse as

$$E_y|_i^0 := a_0 \exp\left(\frac{-(x_i + \frac{1}{2}\Delta x - x_c)^2}{\sigma^2}\right)\cos(x_i + \frac{1}{2}\Delta x - x_c)$$

$$B_z|_i^0 := a_0 \exp\left(\frac{-(x_j - x_c)^2}{\sigma^2}\right)\cos(x_i - x_c)$$

with $a_0 = 0.05$, $\Delta x = 0.05$, $\sigma = 2$ and $x_c = 7$. The pulse wave length λ is 1. The simulation box length is $L = 20$. In the right section of the simulation domain, we set the plasma density $\rho_h = 16$, which implies a plasma frequency $\omega_h = 8\pi$.

This pulse then propagates through the vacuum, hits the plasma border, and becomes reflected. As can be seen in figure 5.3.1, the expected behaviour is accurately reproduced.

For a second test, we use the same configuration, changing the plasma density to $\rho_h = 0.64$. We expect the pulse to be reflected partly, with the greater fraction of its energy passing through the plasma and undergoing dispersion. Figure 5.3.2 shows six snapshots of this 1D simulation. As expected, the transmitted fraction of the pulse becomes decelerated, and its wave number drops.

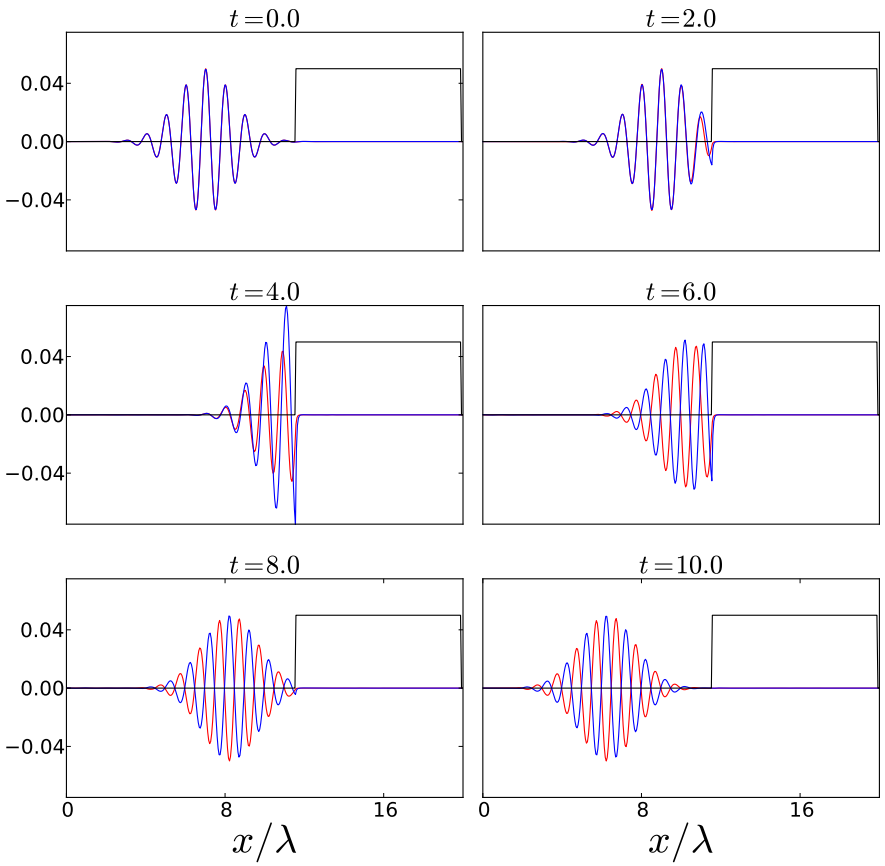

FIGURE 5.3.1. 6 Snapshots of E_y (red), B_z (blue) and the fluid plasma density ρ_h (black) in a simple test of the Impulse splitting method with a high plasma density $\rho_h = 16$. The plasma density has been rescaled for visualization purposes.

The algorithm's properties were then analyzed quantitatively, by setting up a simulation of a 1D plane wave with high plasma ρ_h density. The incoming laser pulse is modeled via inhomogeneous, time dependent Dirichlet boundary conditions and zero as initial values. A spatial grid size of 0.5 for $x \in [0, 200]$ is used. The hybrid density is set to $n_h = 10^8 n_c$ and the system is integrated over the time interval $[0, 200]$. Using these parameters, we have performed a trusted reference simulation with an extremely low time step. Afterwards, a large number of simulations was launched, scanning an interval with their time steps. Each of the latter was compared to the reference results, and the error plotted in figure 5.3.3.

Although this splitting method is of classical order two (since it is a symmetric scheme), it suffers from resonances, which arise in $\mathbf{E}$, $\mathbf{B}$, and $\mathbf{p}_h$ if the density becomes large. In fact, the errors of this scheme are of order zero for certain

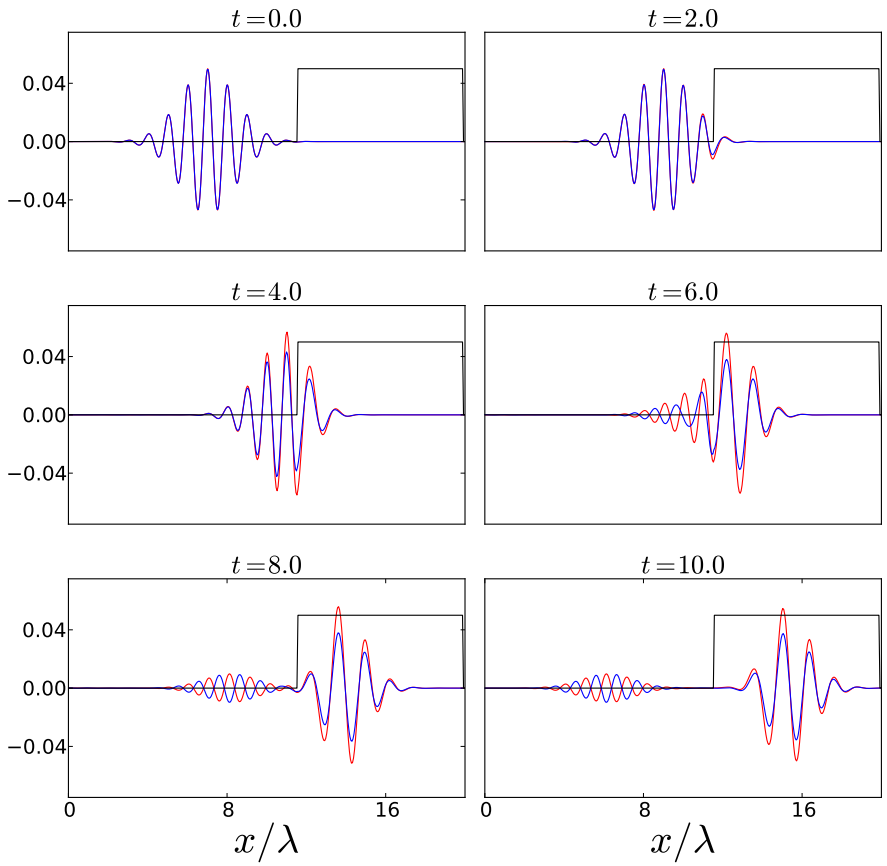

FIGURE 5.3.2. 6 Snapshots of E_y (red), B_z (blue) and the fluid plasma density ρ_h (black) in a simple test of the Impulse splitting method with a low plasma density $\rho_h = 0.64$. The plasma density has been rescaled for visualization purposes.

time steps. The blue curves in Fig. 5.3.3 show the errors in E_y, B_z and $p_{h,y}$ of the standard splitting method (5.3.5)-(5.3.9) as a function of the time step size, while the red line corresponds to a second-order error behavior. To improve the presentation, we only show the interval $[0.25, 0.5]$ for the time steps, but we would like to emphasize that the same effects have been obtained for much smaller time steps as well.

Similar resonance effects have also been observed for multiple time stepping schemes in molecular dynamics simulations [**71**] and for numerical methods for solving second-order differential equations [**64, 66, 67**]. Motivated by these papers, we suggest to apply filter functions and averaging operators to the Maxwellian part and modify the impulse splitting method (5.3.5)-(5.3.9) in the following way:

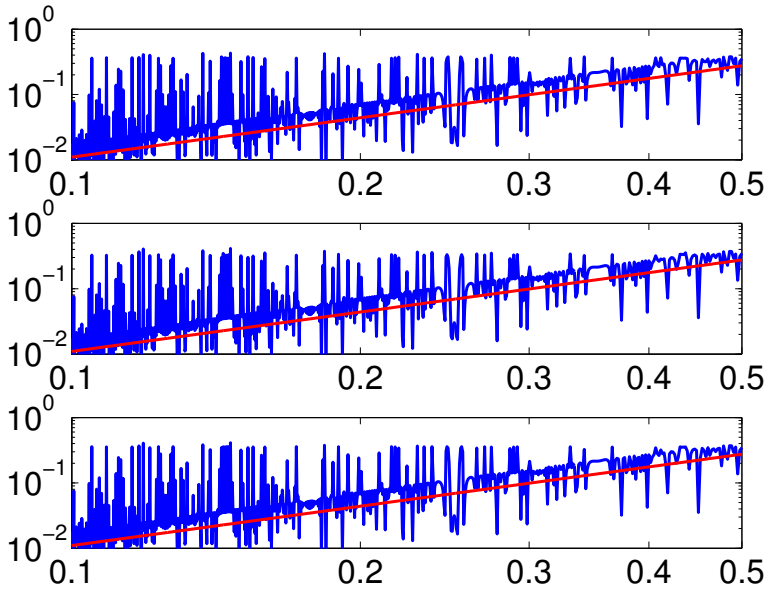

FIGURE 5.3.3. Numerical error for a simple laser plasma interaction setup involving very high fluid density, simulated with the Impulse method. Time steps are scanned through the interval $[0.1, 0.5]$. While the classical order of the method is 2, high frequency resonances cause large errors at certain time steps, and reduce the scheme's effective order to 0.

$$\mathbf{B}^{n+\frac{1}{2}} = \mathbf{B}^n - \frac{1}{2}\Delta t \psi_B(\Delta t \omega_p^n)\tilde{\nabla} \times \phi_E(\Delta t \omega_h^n)\mathbf{E}^n \tag{5.3.10}$$

$$\mathbf{E}^{+} = \mathbf{E}^n + \frac{1}{2}\Delta t \psi_E(\Delta t \omega_p^n)\tilde{\nabla} \times \phi_B(\Delta t \omega_p^n)\mathbf{B}^{n+\frac{1}{2}} \tag{5.3.11}$$

$$\begin{bmatrix} \mathbf{p}_h^{n+1} \\ \mathbf{E}' \end{bmatrix} = \begin{bmatrix} \cos \Delta t \omega_h & \Delta t \mathrm{sinc} \\ -\omega_h \sin \Delta t \omega_h & \cos \Delta t \omega_h \end{bmatrix} \begin{bmatrix} \mathbf{p}_h^n \\ \mathbf{E}^{+} \end{bmatrix} \tag{5.3.12}$$

$$\mathbf{E}^{n+1} = \mathbf{E}' + \frac{1}{2}\Delta t \psi_E(\Delta t \omega_p^n)\tilde{\nabla} \times \phi_B(\Delta t \omega_p^n)\mathbf{B}^{n+\frac{1}{2}} \tag{5.3.13}$$

$$\mathbf{B}^{n+1} = \mathbf{B}^{n+\frac{1}{2}} - \frac{1}{2}\Delta t \psi_B(\Delta t \omega_p^n)\tilde{\nabla} \times \phi_E(\Delta t \omega_p^n)\mathbf{E}^{n+1}. \tag{5.3.14}$$

This modification introduces filter functions ϕ_E, ϕ_B, ψ_E, ψ_B at several points in the scheme. The necessity of filtering can be understood by keeping in mind that eq. (5.3.12) solves for a high frequency oscillation. Thus, when using the updated **E**-field from (5.3.12) for the Maxwell solver steps, to pass on the filtering would mean to use the value at the end of that oscillation, which can be significant even when the average **E** is low. This problem can be tackled e.g. by averaging the electric field. In [**68**], the choice

$$\phi_E(x) = \mathrm{sinc}(\frac{x}{2}) \tag{5.3.15}$$

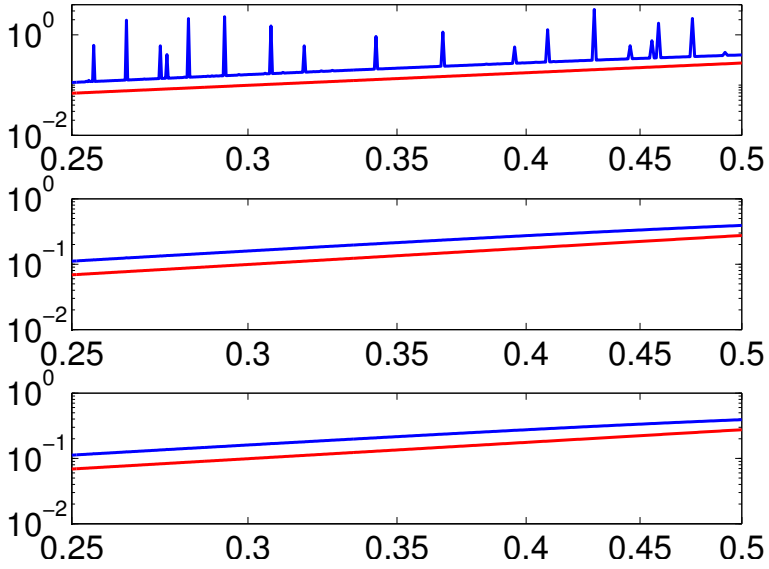

FIGURE 5.3.4. Numerical error of the Mollified Impulse method with one filter function. The three plots show the error of E_y, B_z and $p_{h,y}$, respectively.

is motivated. At the same time, the choice $\phi_B = \psi_B = 1$ is indispensable in order to fullfill

$$\nabla \cdot \mathbf{B} = 0.$$

The error analysis shown in figure 5.3.3 was then repeated with the filter (5.3.15). Results are shown in figure 5.3.4, which indicates a significantly improved approximation. For B_z and $p_{h,z}$, the order of convergence is now 2, and the number of unpleasant resonances for E_y is also lower.

Unfortunately, the choice of the last filter function ψ_E is not trivial to motivate. It would certainly involve a comprehensive local error analysis of the scheme, which has not been done up to now. However, one can try the most obvious choice

$$\psi_E(x) = \phi_E(x) = \mathrm{sinc}(\frac{x}{2}).$$

This has been implemented, and tested again in the same setup as figure 5.3.3 and 5.3.4. The result shown in figure 5.3.5 is surprisingly nice - the error curve clearly indicates second order accuracy in time. This order could be obtained even for extremely high plasma frequencies.

With these choices, we have obtained the linearized fluid Mollified Impulse scheme. It takes on the final form

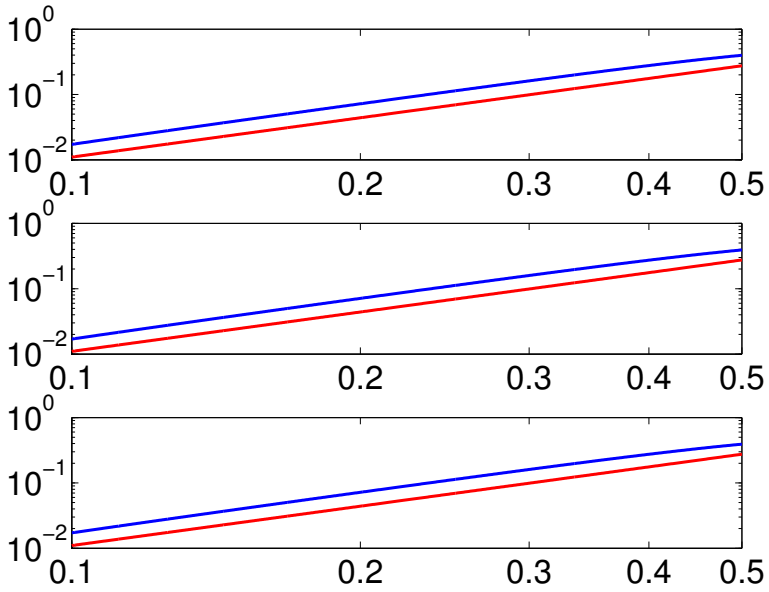

FIGURE 5.3.5. Numerical error of the Mollified Impulse scheme, using two filter functions $\psi_E(x) = \phi_E(x) = \mathrm{sinc}(x/2)$. The three plots show the error of E_y, B_z and $p_{h,y}$, respectively.

$$\mathbf{B}^{n+\frac{1}{2}} = \mathbf{B}^n - \frac{1}{2}\Delta t \psi_B(\Delta t \omega_p^n)\tilde{\nabla} \times \mathrm{sinc}(\frac{\Delta t}{2}\omega_h^n)\mathbf{E}^n \tag{5.3.16}$$

$$\mathbf{E}^{+} = \mathbf{E}^n + \frac{1}{2}\Delta t \mathrm{sinc}(\frac{\Delta t}{2}\omega_p^n)\tilde{\nabla} \times \mathbf{B}^{n+\frac{1}{2}} \tag{5.3.17}$$

$$\begin{bmatrix} \mathbf{p}_h^{n+1} \\ \mathbf{E}' \end{bmatrix} = \begin{bmatrix} \cos\Delta t\omega_h & \Delta t \mathrm{sinc} \\ -\omega_h \sin\Delta t\omega_h & \cos\Delta t\omega_h \end{bmatrix} \begin{bmatrix} \mathbf{p}_h^n \\ \mathbf{E}^{+} \end{bmatrix} \tag{5.3.18}$$

$$\mathbf{E}^{n+1} = \mathbf{E}' + \frac{1}{2}\Delta t \mathrm{sinc}(\frac{\Delta t}{2}\omega_p^n)\tilde{\nabla} \times \mathbf{B}^{n+\frac{1}{2}} \tag{5.3.19}$$

$$\mathbf{B}^{n+1} = \mathbf{B}^{n+\frac{1}{2}} - \frac{1}{2}\Delta t \tilde{\nabla} \times \mathrm{sinc}(\frac{\Delta t}{2}\omega_p^n)\mathbf{E}^{n+1}. \tag{5.3.20}$$

The theoretical properties of the numerical method including a detailed error analysis are currently investigated and will be reported elsewhere.

5.4. Properties of the algorithm

5.4.1. H-VLPL implementation / Results. The numerical integrator which was described in the previous sections has been implemented into the VLPL code as a three- dimensional, parallelized version, and is now operational. In order to examine its accuracy and reliability, we have benchmarked it with a variety of physical processes. First, we check if it correctly models laser propagation through linearly dispersive plasma as well as reflection from overdense plasma. Second, we verify the conservation of the total energy of the system by the hybrid algorithm. Third, our code is applied to the Target Normal Sheath Acceleration (TNSA) process, which would have been very difficult to treat just using PIC means since it uses materials

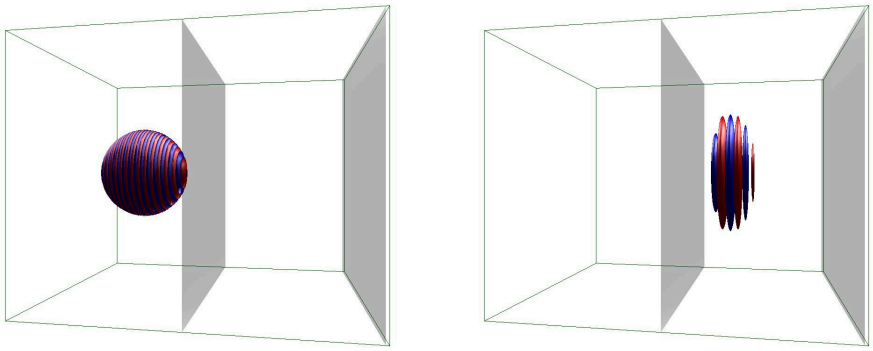

FIGURE 5.4.1. Snapshots of the simulation setup taken with an interactive VR visualization software, which is a part of H-VLPL. The left picture shows the laser pulse (isosurfaces of fixed positive and negative electric field amplitudes) as it enters the hybrid plasma. The right picture demonstrates the dispersive effect.

of solid state density. We check if our hybrid integrator correctly describes the exponential decay of a wave in overdense plasma. Finally, we show its applicability to study the Weibel instability.

5.4.2. Reflection of an incident pulse. As the simplest test one can imagine, we will show that our integrator accurately models refraction in underdense plasma and reflection from overdense plasma. First, we set up a plasma slab of density $0.85n_c$(where $n_c = m\omega_L^2/4\pi e^2$ is the critical density with respect to the laser) and send a $26fs$ Gaussian laser pulse through it. As the pulse hits the surface of the purely hybrid plasma, a part of the wave is transmitted while a significant reflection also occurs.

On the other hand, when the experiment was modified by setting the density to $1.2n_c$, we observe a reflection of the entire electromagnetic wave by the plasma.

We point out that these simulations have been performed using just the fluid part of our combined code without any PIC macroparticles. Still, the effect has been described correctly.

5.4.3. Energy conservation. An important property we require from the new integrator is the conservation of the total energy of the system, comprising PIC macroparticles, electromagnetic fields, and the hybrid fluid. A very simple setup with a laser pulse being reflected from an overdense surface is used for this benchmark. We expect the total energy

$$E_{tot} = \sum_l m_l c^2(\gamma - 1) + \frac{1}{8\pi}\int_V (E^2 + B^2)dV + \int_V n_h(\gamma_h - 1)m_h c^2 dV$$

to be constant, where m_l are the masses of the respective particle species and $\gamma = \sqrt{1 + (p_l/m_l c)^2}$ is the relativistic gamma factor. We denote the hybrid density by n_h and its gamma factor by γ_h. Figure 5.4.2 shows the total energy of the simulation versus time, which is measured in units of laser periods.

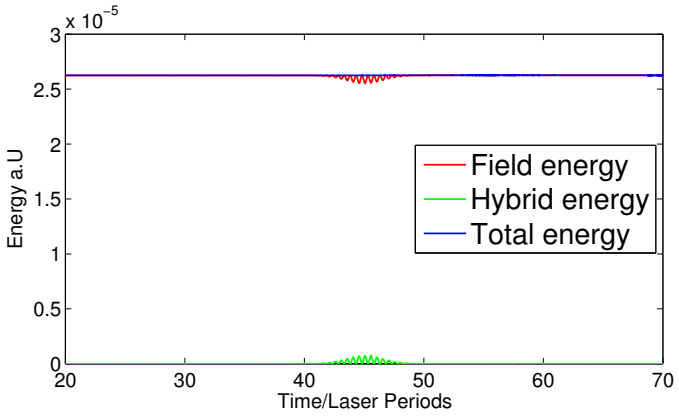

FIGURE 5.4.2. Plot of the total energy, the energy of the electromagnetic field and of the hybrid plasma versus time.

During the laser propagation in vacuum, the energy stays constant except for small fluctuations within the order of magnitude of the machine precision. When the pulse hits the overdense hybrid plasma surface, it is reflected, as can be seen at the time of 45 laser periods. While this reflection occurs, energy fluctuations are limited by 0.04 of the total energy.

5.4.4. Target Normal Sheath Acceleration (TNSA). For a more realistic benchmark we model a physical setup our hybrid code is very suitable for: We use it for the investigation of the TNSA process. TNSA provides a possible way of laser ion acceleration out of solids by utilizing the electrostatic fields generated by the space charge of thermal electrons. The process is shown schematically in figure 5.1.1: A $10fs$ laser pulse of normalized amplitude $a_0 = 2$ is focused on a thin foil which can be assumed to have been pre-ionized by the laser. The foil consists of a bulk part of $1000n_c$, a preplasma on its front surface, and an 80 nm thick proton layer on its back surface. The preplasma is modeled as a density ramp reaching from 0 to $2n_c$ over a distance of 2 laser wavelengths (1.6 μm) and treated entirely by the PIC method. Analogously, we use PIC macroparticles for the back surface protons. On the contrary, any attempt to describe the highly overdense main part of the foil as macroparticles would result in numerical problems. Here we use the hydrodynamic feature of H-VLPL, setting the hybrid density on the grid to $1000n_c$.

The intense laser radiation creates a blow-off region in the front of the foil, resulting in a large cloud of hot electrons, which, in parts, propagates through the foil and passes the coating of the back surface. As the electrons leave the surface, a strong electrostatic field is built up, and the protons are pulled out of the foil and eventually accelerated to high energies. Figure 5.4.3 shows a 3D visualization of the hybrid simulation after 10 and 380 laser periods, respectively. In Fig. 5.4.4, the spectrum of the accelerated ions is shown. A maximum energy of about 0.9 MeV is reached, which is quite remarkable considering the laser intensity in the setup. We conclude that our hybrid algorithm succeeded well and efficiently in treating this numerically challenging physical situation.

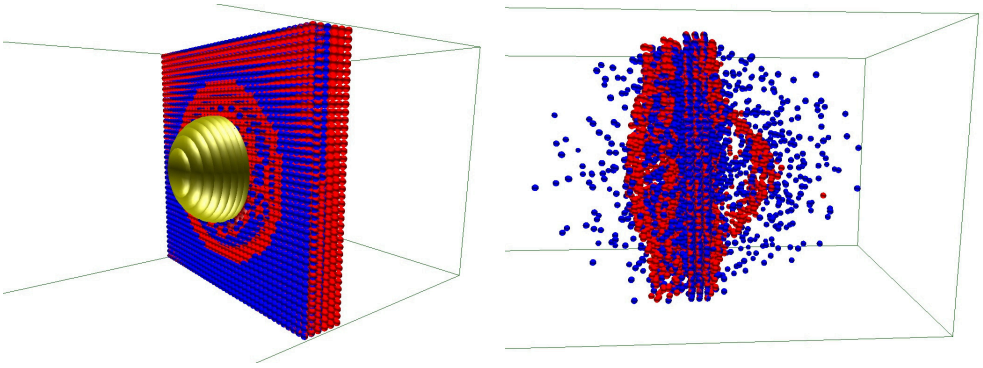

FIGURE 5.4.3. Snapshot of the TNSA benchmark simulation after 10 (left) and 380 (right) laser periods. PIC macroparticles containing electrons are displayed blue, while those with protons are rendered red. One observes the thin coating of protons dissolving from the back of the foil in the right image.

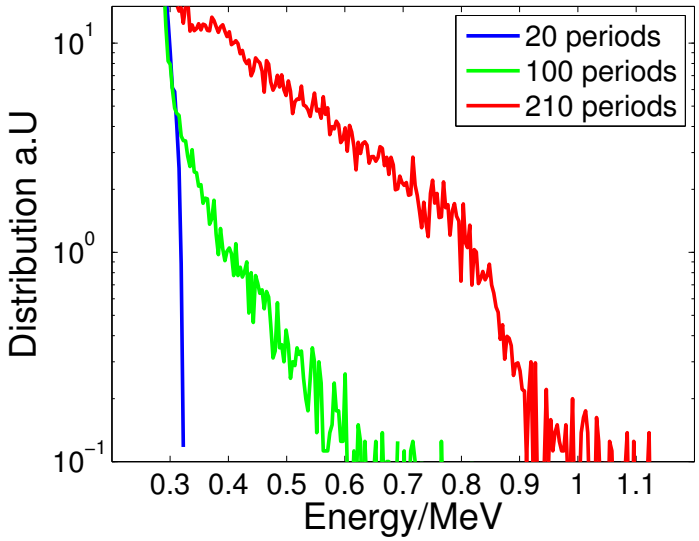

FIGURE 5.4.4. Spectrum of the accelerated ions in the TNSA simulation.

5.4.5. Comparison of skin depths. As a further benchmark for our hybrid code we check the decay of a wave in an overdense plasma. According to the linear theory, it should scale as $E(x) \sim \exp(-x/\delta_s)$ in the plasma, where $\delta_s = c/\sqrt{\omega_p^2 - \omega^2}$ is the skin length. Several simulations have been set up using a circularly polarized laser pulse with duration 6λ and amplitude $a_0 = 0.01$ in order to avoid relativistic nonlinearities. The densities of the plasma surfaces used for this benchmark range from $1.5n_c$ to $500n_c$. We show the decay of the wave inside the plasma for three

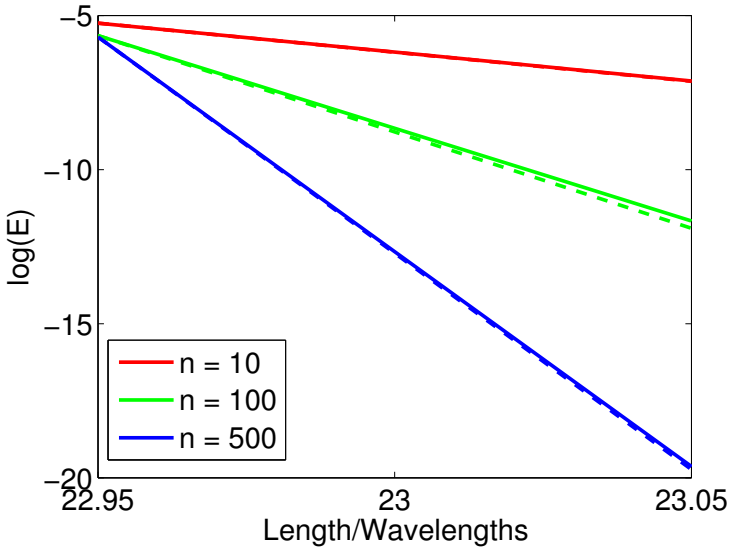

FIGURE 5.4.5. Snapshot of the logarithm of the fields $\log(\sqrt{E_y^2 + E_z^2})$ (solid lines) inside the plasma for three different densities. The dashed lines show the theoretical prediction.

densities; the agreement with the theoretical predictions up to densities of $500n_c$ is very good.

Additionally, by fitting exponentials through the measured field data, one can compute the skin depths of the decay. In figure , the results are shown and we get an excellent agreement. One has to mention that even though these simulations have been done with a grid step of 0.05λ, the skin depths match remarkably well with the theory up to a density of $500n_c$, where $\delta_s = 0.007\lambda$.

5.4.6. Investigation of Weibel instabilities. When studying the fast ignition (FI) scenario in inertial confinement fusion, one is interested in the behaviour of the beam of electrons propagating into the target, particulary the amount of energy deposited and the shaping of the beam over time. Generally, electron beams running through a background plasma suffer from the major problem of the Weibel instability [**72**], which is a very important issue to be studied if one wants to understand the FI scheme. The ratio of the beam density to that of the background n_b/n_p, as well as the density gradient in propagation direction, is likely to influence the evolution of the beam, its filamentation and the increase of electromagnetic fields as the instability builds up.

For low densities, roughly about $100n_c$, PIC simulations can be carried out to perform these investigations. However, as the electron beam approaches the core of an ICF pellet, the density will exceed multiple times solid density and conventional PIC codes must be applied with extremely small time steps in order to avoid numerical instability, and thus cannot be used with reasonable computational effort.

We are going to study the phenomenon of the Weibel instability with our new hybrid code, using standard PIC macroparticles for the electron beam and the fluid

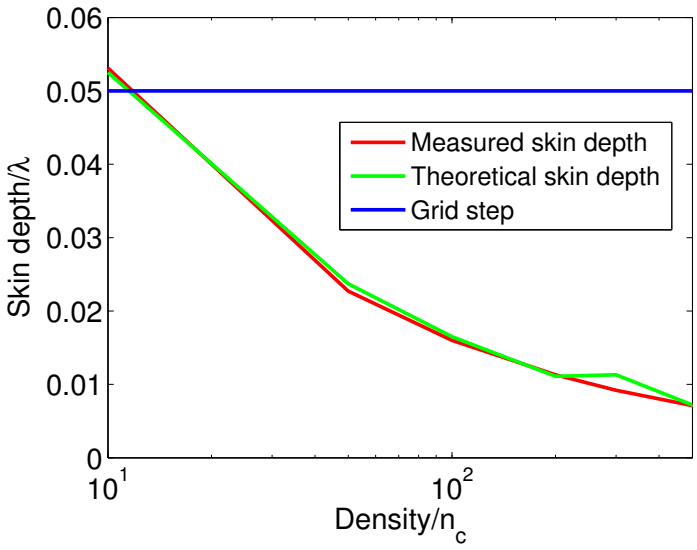

FIGURE 5.4.6. Plot of the skin depth versus the plasma density. The blue line shows the grid step used in the simulation.

part in order to model the background plasma. Since H-VLPL has no restrictions for the hybrid densities used, we can perform such simulations within a moderate amount of CPU time.

In order to obtain a proof for the physical correctness of our code within the linear regime, we have launched tests with H-VLPL comparing a classical PIC computation to a hybrid simulation of this setup. An electron beam with density n_b propagates through a background plasma with $n_p = 100 n_b$. The momentum of the beam electrons is $p_b = mc$ with a thermal spread of $10^{-4}mc$, and the momentum of the background is chosen such that its current compensates for that of the beam plasma, meaning

$$n_b v_b + n_p v_p = 0.$$

The setup is restricted to a 2D geometry, with the beams traveling perpendicularly to the x-y-plane; this is necessary in order to exclude two-stream instabilities. After about 3.3 beam plasma periods $2\pi/\omega_b$, with $\omega = \sqrt{4\pi n_b e^2/m}$, one observes a strong filamentation of the beam, and a magnetic field builds up. When launching the same simulation with and without the hybrid model, we notice that the latter succeeds well in describing the filamentation effect at the initial, linear stage. We compare the integral of the squared magnetic field

$$\int_V \mathbf{B}^2 dV$$

of the two models. At this point it has to be mentioned that during the nonlinear stage of the instability, the present version of H-VLPL will fail in describing the

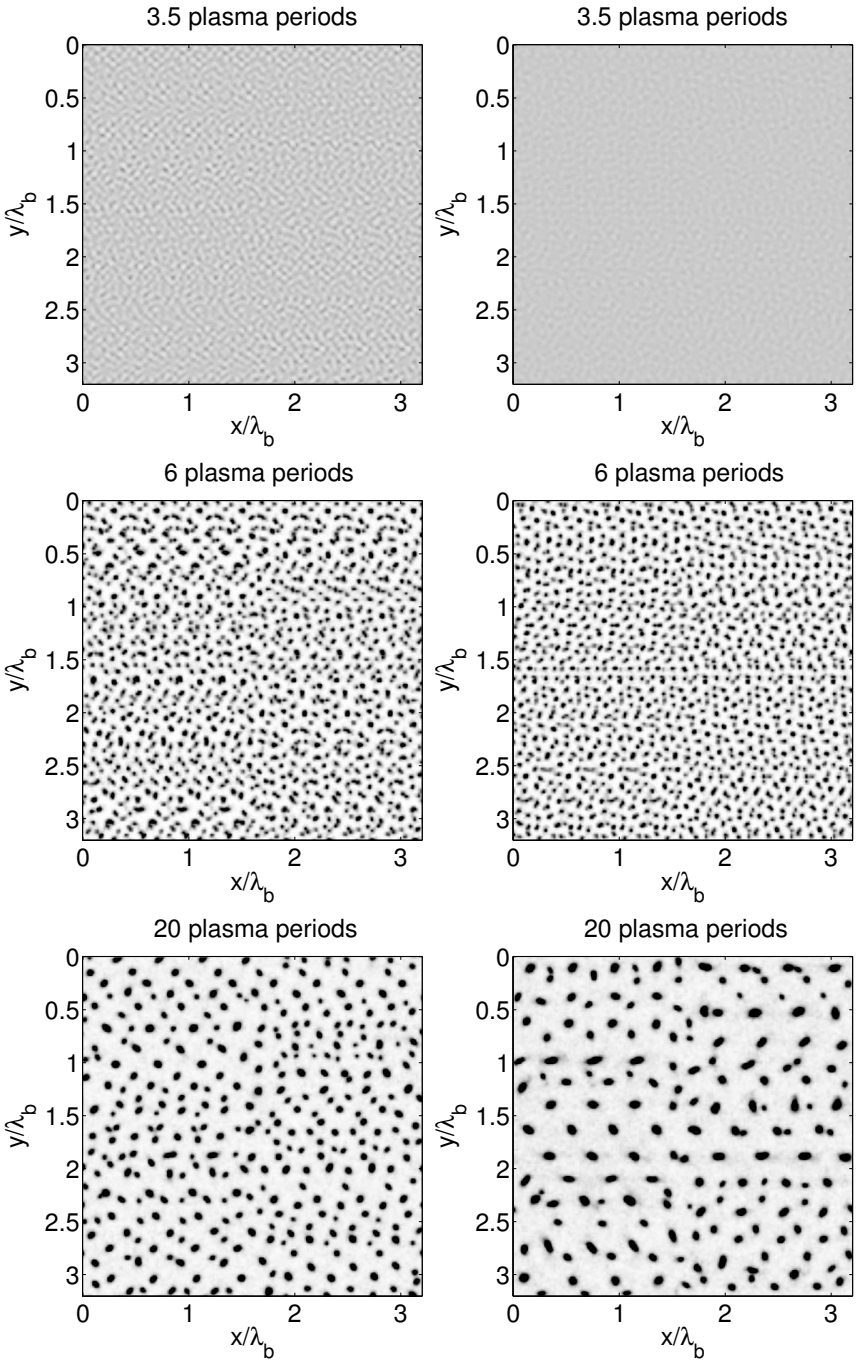

FIGURE 5.4.7. Snapshot of the Weibel instability benchmark simulations with PIC (left) and the hybrid code (right) at 3.5, 6, and 20 beam plasma periods. We observe very similar behaviour, although the instability starts approximately 0.5 period later with the hybrid model due to the lower numerical noise.

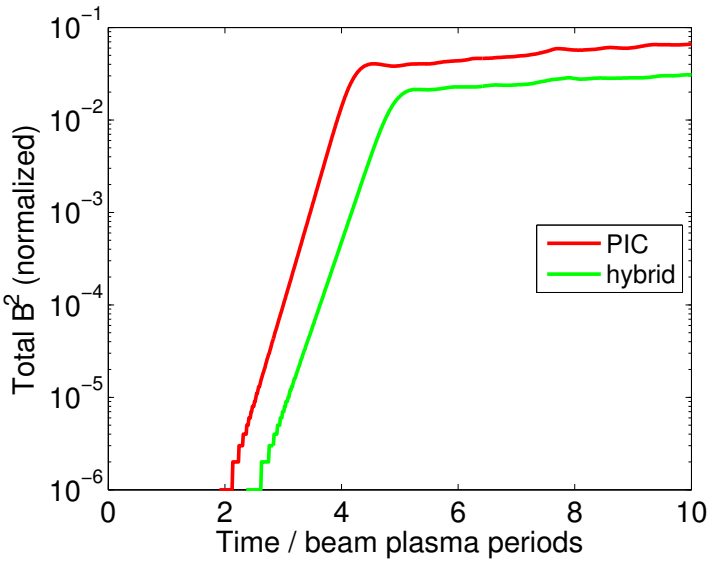

FIGURE 5.4.8. Integral of the squared **B**-field over the simulation plane. During the linear stage of the instability, we observe an exponential growth with almost the same growth rate.

filamentation of the background plasma since it does not treat its continuity equation and convective term of momentum evolution. Additionally, the fluid plasma does not react to magnetic fields directly. Nevertheless, the behaviour, and the growth rate of the Weibel instability during the linear stage are accurately reproduced. This result indicates the applicability of H-VLPL to the Weibel instability scenario, and makes further investigations of the effect with an advanced, fully hydrodynamic hybrid code appear promising.

5.5. Summary

Conventional particle-in-cell implementations are limited by a stability condition, which is connected to the plasma frequency. In order to overcome this restriction, a PIC/fluid hybrid code was developed. In addition to the well-known PIC part, it can also model a plasma as a linearized fluid, using a specially designed exponential integrator scheme. This scheme was implemented into the existing VLPL PIC code, and successfully tested on a variety of physical examples. The results have been published in [**73**].

CHAPTER 6

H-VLPL3D PIC/fluid hybrid code

In this chapter, the second PIC/fluid hybrid code implementation is introduced. In contrast to the scheme from chapter 5, the full non-linear cold, relativistic fluid equations are solved. The algorithm has been designed for the efficient simulation of long wake fields. Hence, no exponential integrator is involved here, but a novel spatial discretization scheme is used.

6.1. Introduction

The idea of utilizing wake fields as particle accelerators becomes increasingly promising [**9, 5**] . While conventional accelerators are limited by characteristic breakdown fields, plasma waves do not suffer from such restrictions. They reach field strengths orders of magnitude higher. In this context, TeV proton bunches as drivers have recently gained much attention [**3**]. Due to their high energy, they may remove the need for multiple acceleration stages.

In order to achieve longitudinal electric fields in the GV/m-range, electron densities of at least $n_e = 10^{14}\text{cm}^{-3}$ are required. Thus, one needs proton bunches as short as half of the plasma wave length $\lambda_p = \frac{2\pi c}{\omega_p} \approx 3\text{mm}$. Unfortunately, there are no proton accelerators in the TeV class capable of producing bunches this short. This drawback can be overcome by making use of the self-modulation effect on the driving pulse [**22**].

Recent results show that phase velocity control by altering the background plasma density appears feasible. Also, side injection of the particles to accelerate can be efficient. Because of the complexity of such setups as well as the large scale of experiments involving TeV proton beams, reliable simulations are crucial. A commonly preferred method for wake field simulations is the particle-in-cell (PIC) algorithm.

However, the self-modulated proton driver plasma wakefield acceleration (SM-PDPWA) process under investigation has special requirements on the numerical algorithms employed. It involves about 200-500 plasma wavelengths of the background together with very long propagation distances $\geq$ 10m. PIC treatments tend to be very costly in CPU time. They also suffer from numerical noise and diffusion, which renders them ineffective for this regime.

We show that a PIC/fluid hybrid code concept is very well suited for this problem. The basic idea is again to represent the plasma under investigation by two distinct means: First, as a set of PIC macroparticles for parts undergoing kinetic effects. Second, as a fluid through numerical solution of conservation laws. For wake field simulations, the algorithm from section 5 is not sufficient, since non-linear density modulation effects must be considered. Hence, one can think of a hybrid implementation which solves Euler's gas equations for the fluid part.

The latter offers a number of advantages over the PIC method: It is far more efficient, with low noise and less numerical diffusion. In the last years, hybrid techniques have gained importance in high density plasma simulations, including fast ignition (FI) experiments and solid state density plasma interactions. Most of these codes do not model the propagation of electromagnetic waves as well as electrostatic waves, instead using magnetohydrodynamic (MHD) descriptions. The hybrid PIC code LSP [**31**] uses a particle-in-cell algorithm along with a fluid model and an implicit electromagnetic field solver. Also, the OSIRIS and the dHybrid[**34**] code comprise hybrid functionality, treating ions kinetically and electrons as a fluid, under the assumption $\nabla \times \vec{B} = \mu_0 \vec{J}$.

For the new hybrid system presented here, we choose a more general fluid approach. No MHD assumptions are made. Instead, the background plasma is a true cold fluid, covering density modulations and convection. For the spatial discretization, we adopt the flux-corrected transport (FCT)[**44**] method. It is combined with a modified quadratic upstream interpolation for convective kinematics (QUICK)[**74**] scheme.

In the next sections, we shall give a detailed description of the algorithm. Sub section 6.2 introduces the fluid equations which are added to the existing PIC model, section 6.3 explains the spatial scheme used. The general challenge of such a simulation code design is clarified in chapter 6.4, its solution for the final 3D code is shown in chapter 6.5. In section 6.7, we discuss the various time integrators which can be applied. The H-VLPL implementation is verified first on simple physical examples. Afterwards, more application-oriented setups are tested. Results are depicted in chapter 6.9.

6.2. Fluid Model

In the new H-VLPL implementation, a plasma can be modeled by two distinct means: First, using a kinetic description and statistically populating the phase space with PIC macroparticles. It is capable of simulating effects like wave-breaking while trading speed for accuracy and suffering from damping effects. Second, it also contains a cold-fluid model. The latter, despite the fact it fails in the presence of wave-breaking, works far more smoothly and efficiently. The equations related to the fluid part read

$$\frac{\partial}{\partial t}\mathbf{E} = \nabla \times \mathbf{B} - \mathbf{J}^{PIC} - \frac{q}{\gamma^h}\rho^h \mathbf{p}^h \tag{6.2.1}$$

$$\frac{\partial}{\partial t}\mathbf{p}^h = -(\mathbf{v}^h \cdot \nabla)\mathbf{p}^h + q(\mathbf{E} + \mathbf{v}^h \times \mathbf{B}) \tag{6.2.2}$$

$$\frac{\partial}{\partial t}\rho^h = -\nabla \cdot (\frac{\rho^h}{\gamma^h}\mathbf{p}^h), \tag{6.2.3}$$

where $\mathbf{p}^h$ denotes the relativistic fluid momentum and ρ^h is the fluid density. $\mathbf{v}^h$ is the fluid velocity, $\mathbf{J}^{\mathrm{PIC}}$ is the current caused by the PIC algorithm. The cold-fluid plasma model implies that pressure terms can be neglected; the second equation has been obtained from the momentum density conservation law. This model is used in addition to the kinetic description. It is intended for the cold parts of the plasma, where thermal effects can be neglected. Therefore one must carefully decide for each particle species which model is appropriate.

6.3. Spatial discretization

It is a widely known fact that the solution of conservation laws such as Euler's gas equations is not trivial. The hyperbolic nature of the partial differential equations involved causes problems related to Runge's phenomenon, like spurious oscillations, for linear high order schemes. By now, after decades of research in the large field of Computational Fluid Dynamics (CFD), there are now many efficient non-linear numerical methods available.

The simulation of electromagnetic fluid phenomena, like plasma wake fields, however, adds another requirement to the schemes used: The approximation error of the flux in a FVM can cause unphysical modulations in the density profile. This results in artificial higher harmonics of the wake, eventually destroying the overall wake field structure.

After extensive testing and careful design of multiple discretization schemes, several algorithms were found which were capable of modeling wake fields with low or no distortions. Among the uniform (non-staggered) schemes with this property is the Kurganov-Tadmor central scheme [**42**]. Still, using non-staggered schemes always enforces interpolation of the electric field onto the cell centers, causing an unphysical diffusion of the wake structure. Hence, we have designed a new, simple, staggered scheme for the FVM charge flux.

In the next chapters, the details of this algorithm will be depicted. Subsection 6.4 will explain the challenges encountered with various CFD schemes, and discuss possible solutions. In 6.5, the spatial discretization for the charge density flux is shown. Subsection 6.6 describes how the problem of solving the convective momentum term in (6.2.2) is tackled.

6.4. General considerations

The well-established field of Computational Fluid Dynamics (CFD) offers a wide range of spatial discretization methods. Examples include the MUSCL [**41**], PPM [**45**] and QUICKEST [**74**] schemes as well as finite element approaches. Since the grid geometry is rectangular, there is no need for finite element algorithms. Given this simplification, one might argue that standard finite-volume schemes should be used. For example, MUSCL Riemann solvers appear appropriate. However, the computational task of wake field modeling causes certain restrictions to the discretization pattern employed. The structure of the Yee discretization for electromagnetic fields involves electric fields located at the cell faces. Thus, any nonstaggered hydrodynamic space discretization implies interpolating electric fields to the cell centers.

Additionally, many schemes can cause unphysical high frequency distortions to the wake field structure. Thorough investigations showed that this is the case e.g. for upwind methods and their MUSCL generalizations.

It is crucial to find an efficient method which preserves the wake field as long as possible. For this purpose, a simple one-dimensional plasma wake field benchmark was created. It works as follows:

We define a 1D wake field setup, starting with a density offset $\rho_0 = 4\pi^2$. The plasma frequency associated with ρ_0 will then be $\omega_0 = 2\pi$. We introduce a small density modulation $\rho_1 \ll \rho_0$, and set the total electron density to

$$\rho(x, t = 0) = \rho_0 + \rho_1 \cos(2\pi x).$$

The longitudinal electric field is

$$E_x(x, t = 0) = E_0 \sin(2\pi x),$$

where $E_0 = \rho_1/(2\pi)$ because of Poisson's law, and the initial momentum (in the non-relativistic limit) is

$$p_x(x, t = 0) = -\frac{E_0}{2\pi} \cos(2\pi x) = -\frac{\rho_1}{4\pi^2} \cos(2\pi x).$$

These conditions assume an immobile ion background of charge density $\rho_{\text{Ion}} = \rho_0$. The three variables E_x, ρ, p_x at $t = 0$ are shown in figure 6.4.1. The 1D partial differential equations to be solved for this setup are

$$\frac{\partial}{\partial t} E_x = -\rho_0 v_x \tag{6.4.1}$$

$$\frac{\partial}{\partial t} (\rho p_x) = -\frac{\partial}{\partial x} (\rho v_x p_x) + \rho E_x \tag{6.4.2}$$

$$\frac{\partial}{\partial t} \rho = -\frac{\partial}{\partial x} (\rho v_x), \tag{6.4.3}$$

where $v_x = p_x/\gamma$ is the fluid velocity and $\gamma = \sqrt{1 + p_x^2}$ is the relativistic factor.

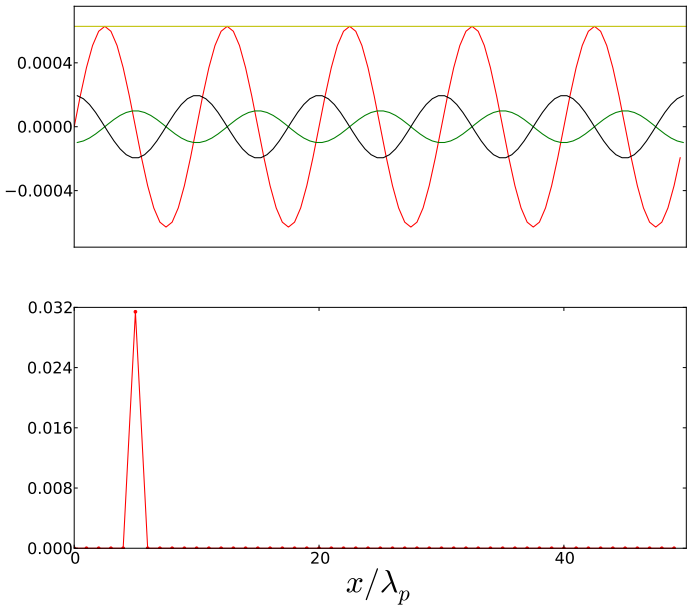

FIGURE 6.4.1. Initial setup for the wake field test problem at $t = 0$. The upper graph shows the longitudinal electric field $E_x(x)$ (red), the density modulation $\rho_1(x)$ (black) and the initial momentum p_x (green). The lower graph shows the (trivial) initial spectrum of E_x.

In the limit $\rho_1 \ll \rho_0$, and $p_x \ll 1$, we can simplify the set of equations to

$$\frac{\partial}{\partial t} E_x = -\rho_0 p_x \tag{6.4.4}$$

$$\frac{\partial}{\partial t} \left(\rho_0 p_x\right) = \rho_0 E_x \tag{6.4.5}$$

$$\frac{\partial}{\partial t} \rho = -\partial_x \cdot (\rho_0 p_x). \tag{6.4.6}$$

For the initial conditions given above, the solution is

$$E_x(x,t) = \frac{\rho_1}{2\pi} \sin(2\pi(x-t)) \tag{6.4.7}$$

$$\rho(x,t) = \rho_0 + \rho_1 \cos(2\pi(x-t)) \tag{6.4.8}$$

$$p_x(x,t) = -\frac{\rho_1}{4\pi^2} \cos(2\pi(x-t)). \tag{6.4.9}$$

The solution (6.4.7)-(6.4.9) essentially resembles a wake field without a driver, which extends to infinity. The solution is separable in space and time, i.e. the problem can be viewed as being composed of separated harmonic oscillators at each spatial position. Still, it looks like a propagating wave due to the phase shift between the locations.

This simple problem is then used to test several fluid schemes for their basic capability of simulating wake fields. We define a 1D simulation domain $D = [0, L[$, with $L \in \mathbb{N}$. The grid step is chosen to be $\Delta x = \frac{1}{20}$, which is a realistic value for further simulations. The grid points are then denoted by

$$j \in \{0...n\}\,,\; n := \frac{L}{\Delta x}.$$

Boundary conditions are set to be periodic for each discretized spatial differential operator. The standard finite volume semi-discretization

$$\frac{\partial}{\partial t} \rho_{j+\frac{1}{2}} = \frac{1}{\Delta x} \left(f_{j+1}(t) - f_j(t)\right)$$

is used, where the spatially discretized variables $\rho_{j+\frac{1}{2}}$, $\left(\rho p_x\right)_{j+\frac{1}{2}}$ are defined as cell averages:

$$\rho_{j+\frac{1}{2}} := \int_{j\Delta x}^{(j+1)\Delta x} \rho(x) dx.$$

$$\left(\rho p_x\right)_{j+\frac{1}{2}} := \int_{j\Delta x}^{(j+1)\Delta x} \left(\rho p_x\right)(x) dx.$$

The electric field E_x is defined on the cell edges:

$$E_{x,\,j} := E_x(j\Delta x)$$

Eq. (6.4.5) is discretized as

$$\frac{\partial}{\partial t} \left(\rho p_x\right)_{j+\frac{1}{2}} = \rho_{j+\frac{1}{2}} \frac{1}{2} \left(E_{x,\,j} + E_{x,\,j+1}\right).$$

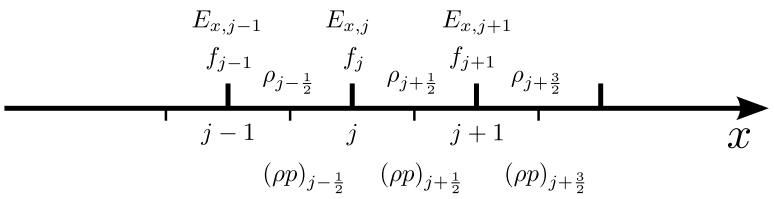

FIGURE 6.4.2. Spatial discretization scheme for the 1D benchmark setup. The electric field is located at the cell face, as given by the Yee scheme. The density ρ as well as the momentum density (ρp_x) is defined at the cell center.

We start with the simplest scheme available, namely the upwind scheme, which defines the flux to be

$$f_j^U := \begin{cases} \rho_{j-1} v_{x,\,j-1} & \text{if } p_{x,\,j-1} + p_{x,\,j} > 0 \\ \rho_j v_{x,\,j} & \text{otherwise} \end{cases} . \tag{6.4.10}$$

The semi-discretization of the problem reads

$$\frac{\partial}{\partial t}\rho_j = \frac{1}{\Delta x}\left(f_{j+1}^U - f_j^U\right) \tag{6.4.11}$$

$$\frac{\partial}{\partial t}\left(\rho p_x\right)_{j+\frac{1}{2}} = \rho_{j+\frac{1}{2}} \frac{1}{2}\left(E_{x,\,j} + E_{x,\,j+1}\right) \tag{6.4.12}$$

$$\frac{\partial}{\partial t} E_{x,\,j} = -\, f_j^U . \tag{6.4.13}$$

In eq. (6.4.12), the convective term has been neglected (which is legitimate for wake fields in the linear regime). One also notices that this discretization readily fulfills Poisson's theorem. Since (6.4.11)-(6.4.13) will show oscillatory behaviour with relatively low frequency, we can use a simple Strang splitting scheme (see chapter (3.4)) for the time integration:

$$\left(\rho p_x\right)_{j+\frac{1}{2}}^{n+\frac{1}{2}} = \left(\rho p_x\right)_{j+\frac{1}{2}}^{n} + \frac{1}{4}\Delta t \rho_j^n \left(E_{x,\,j}^n + E_{x,\,j+1}^n\right) \tag{6.4.14}$$

$$\left(\rho_j^n, E_{x,\,j}^n\right) \to \left(\rho_j^{n+1}, E_{x,\,j}^{n+1}\right) \tag{6.4.15}$$

with e.g. trapezoidal-leapfrog integrator or explicit Euler

$$\left(\rho p_x\right)_{j+\frac{1}{2}}^{n+1} = \left(\rho p_x\right)_{j+\frac{1}{2}}^{n+1} + \frac{1}{4}\Delta t \rho_j^{n+1} \left(E_{x,\,j}^{n+1} + E_{x,\,j+1}^{n+1}\right) . \tag{6.4.16}$$

The results are shown in fig. 6.4.3, with the initial condition given in fig. 6.4.1. It is generally known that for advection problems, the upwind scheme tends to smoothen the solutions, smearing out fine structures through artificial diffusion. The wake field solution (6.4.7)-(6.4.9) also looks like a wave travelling with the speed of light. Naively, one could expect the wake field to be smoothened, too.

However, this is not the case. While looking similar, the essential part of the problem at hand is not advective. We want to accurately resolve local oscillations, so the quality of the fluid scheme depends strongly on its ability to preserve the oscillation phase. The Upwind scheme performs exceptionally bad at this task, and the consequence is a high frequency distortion. It adds a significant noise to every variable involved, eventually destroying the wake structure. The phase information

contained in p_x and E_x is lost due to the repeated interpolations onto the cell centers or edges (midpoint rule in (6.4.12), and Upwind in eq. (6.4.11),(6.4.13)).

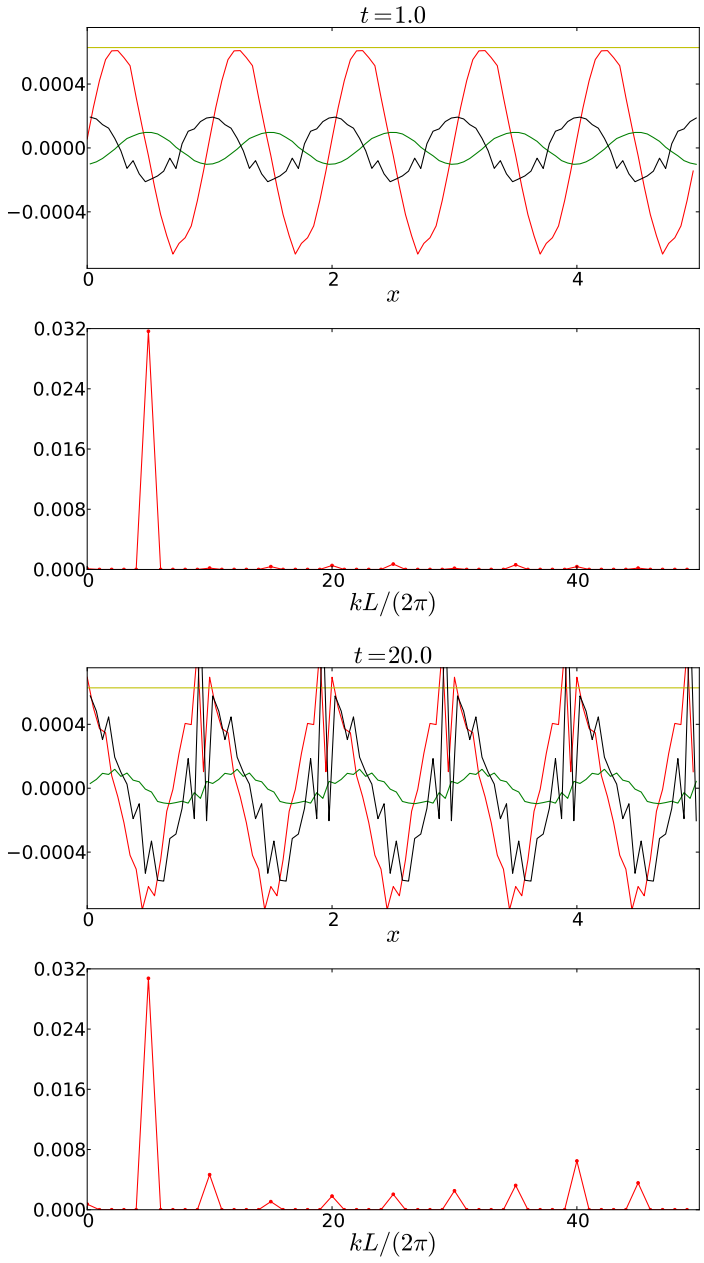

FIGURE 6.4.3. Plots of the result of the Upwind scheme, applied on the linear wake field problem (6.4.1)-(6.4.3) with $\Delta x = 0.05$, $\Delta t = 0.025$. One observes that, while the scheme is stable, it causes a severe distortion to the wake field structure.

The obvious bug-fix for this issue is to improve the interpolation schemes. Hence, we replace the midpoint rule in (6.4.12) by higher order interpolation, and the Upwind scheme by a flux-limited high-order method. We begin with deriving the interpolation coefficients.

First, we must not forget that we are using finite-volume fluid schemes. Thus, we must perform the interpolation with an integral condition. For $\rho_{j+\frac{1}{2}}$ we perform quadratic interpolation in order to keep the stencil symmetrical. Without loss of generality, the grid points are assumed to lie around $j = 0$, and the grid cell length is $\Delta x = 1$. The interpolation polynomial is named

$$p_\rho(x) = ax^2 + bx + c.$$

The conditions are

$$\begin{aligned}
\frac{1}{\Delta x}\int_{-1}^{0} p_\rho(x)dx =& \rho_{-\frac{1}{2}} \\
\frac{1}{\Delta x}\int_{0}^{1} p_\rho(x)dx =& \rho_{\frac{1}{2}} \\
\frac{1}{\Delta x}\int_{1}^{2} p_\rho(x)dx =& \rho_{\frac{3}{2}}.
\end{aligned}$$

This yields

$$\begin{aligned}
a =& \frac{\rho_{\frac{3}{2}} - 2\,\rho_{\frac{1}{2}} + \rho_{-\frac{1}{2}}}{2} \\
b =& \rho_{\frac{1}{2}} - \rho_{-\frac{1}{2}} \\
c =& \frac{-\rho_{\frac{3}{2}} + 5\,\rho_{\frac{1}{2}} + 2\,\rho_{-\frac{1}{2}}}{6},
\end{aligned}$$

so the interpolation polynomial reads

$$p_\rho(x) = \frac{\rho_{\frac{3}{2}} - 2\,\rho_{\frac{1}{2}} + \rho_{-\frac{1}{2}}}{2}\,x^2 + \left(\rho_{\frac{1}{2}} - \rho_{-\frac{1}{2}}\right)\,x + \frac{-\rho_{\frac{3}{2}} + 5\,\rho_{\frac{1}{2}} + 2\,\rho_{-\frac{1}{2}}}{6},\ x \in [0,1[,$$

and for an arbitrary grid index j it is

$$\begin{aligned}
p_\rho^j(x) \quad = \quad & \frac{\rho_{j+\frac{3}{2}} - 2\,\rho_{j+\frac{1}{2}} + \rho_{j-\frac{1}{2}}}{2}\,x^2 + \left(\rho_{j+\frac{1}{2}} - \rho_{j-\frac{1}{2}}\right)\,x + \frac{-\rho_{j+\frac{3}{2}} + 5\,\rho_{j+\frac{1}{2}} + 2\,\rho_{j-\frac{1}{2}}}{6}, \\
& x \in [0,1[.
\end{aligned}$$

Because the electric field is staggered with respect to $\rho_{j+\frac{1}{2}}$, we use cubic interpolation for E_x to keep the interpolating functions symmetrical. The cubic hermite interpolation polynomial can be written as a linear combination of cubic basis functions. The coefficients are the interpolants' values or derivatives. The interpolation scheme reads

$$\begin{aligned}
p_E(t) =& (2t^3 - 3t^2 + 1)E_{x,\,0} + \\
& \left(t^3 - 2t^2 + t\right)\left(E_{x,\,1} - E_{x,\,-1}\right) \\
& + (-2t^3 + 3t^2)E_{x,\,1} + \\
& \left(t^3 - t^2\right)\left(E_{x,\,2} - E_{x,\,0}\right),\ t \in [0,1].
\end{aligned}$$

We can then approximate

$$\begin{aligned}
\frac{\partial}{\partial t}\left(\rho p_x\right)_{j+\frac{1}{2}} &= \frac{1}{\Delta x}\int_{j\Delta x}^{(j+1)\Delta x} \rho(x)E_x(x)dx \\
&\approx \frac{1}{\Delta x}\int_{j\Delta x}^{(j+1)\Delta x} p_\rho^j(\frac{x-j\Delta x}{\Delta x})E_x^j(\frac{x-j\Delta x}{\Delta x})dx \\
&= \int_0^1 p_\rho^j(x)E_x^j(x)dx \\
&= \frac{1}{360}(\rho_{j+\frac{3}{2}}E_{x,\,j+2} + 31\rho_{j+\frac{1}{2}}E_{x,\,j+2} - 2\,\rho_{j-\frac{1}{2}}\,E_{x,\,j+2} \\
&\quad - 16\,\rho_{j+\frac{3}{2}}\,E_{x,\,j+1} - 211\,\rho_{j+\frac{1}{2}}\,E_{x,\,j+1} + 17\,\rho_{j-\frac{1}{2}}\,E_{x,\,j+1} \\
&\quad + 17\,E_{x,\,j}\,\rho_{j+\frac{3}{2}} - 2\,E_{x,\,j-1}\,\rho_{j+\frac{3}{2}} - 211\,\rho_{j+\frac{1}{2}}\,E_{x,\,j} - 16\,\rho_{j-\frac{1}{2}}\,E_{x,\,j} \\
&\quad + 31\,E_{x,\,j-1}\,\rho_{j+\frac{1}{2}} + \rho_{j-\frac{1}{2}}\,E_{x,\,j-1}) \\
&=: (\rho E_x)^{int}_{j+\frac{1}{2}} \qquad (6.4.17)
\end{aligned}$$

To obtain a high resolution for the continuity equation, one can e.g. employ fourth-order flux interpolation:

$$f_i^{hi} = \frac{7}{12}\left(\left(\rho v_x\right)_{i-\frac{1}{2}} + \left(\rho v_x\right)_{i+\frac{1}{2}}\right) - \frac{1}{12}\left(\left(\rho v_x\right)_{i-\frac{3}{2}} + \left(\rho v_x\right)_{i+\frac{3}{2}}\right). \qquad (6.4.18)$$

It is generally known from Computational Fluid Dynamics research that such a scheme cannot be used as the flux approximation without any modifications. Doing so would result in spurious oscillations and instability.

Hence, we combine this scheme with the Upwind flux (6.4.10) via the Flux-Corrected Transport (FCT) algorithm [**44**]. Essentially, it takes as input the density $\left(\rho^n_{j+\frac{1}{2}}\right)_{j=0}^{N-1}$ to be updated, the time step Δt, a low order flux approximation $\left(f_j^{lo}\right)_{j=0}^{N-1}$ which is known to smoothen advected solutions, and a high order flux $\left(f_j^{hi}\right)_{j=0}^{N-1}$.

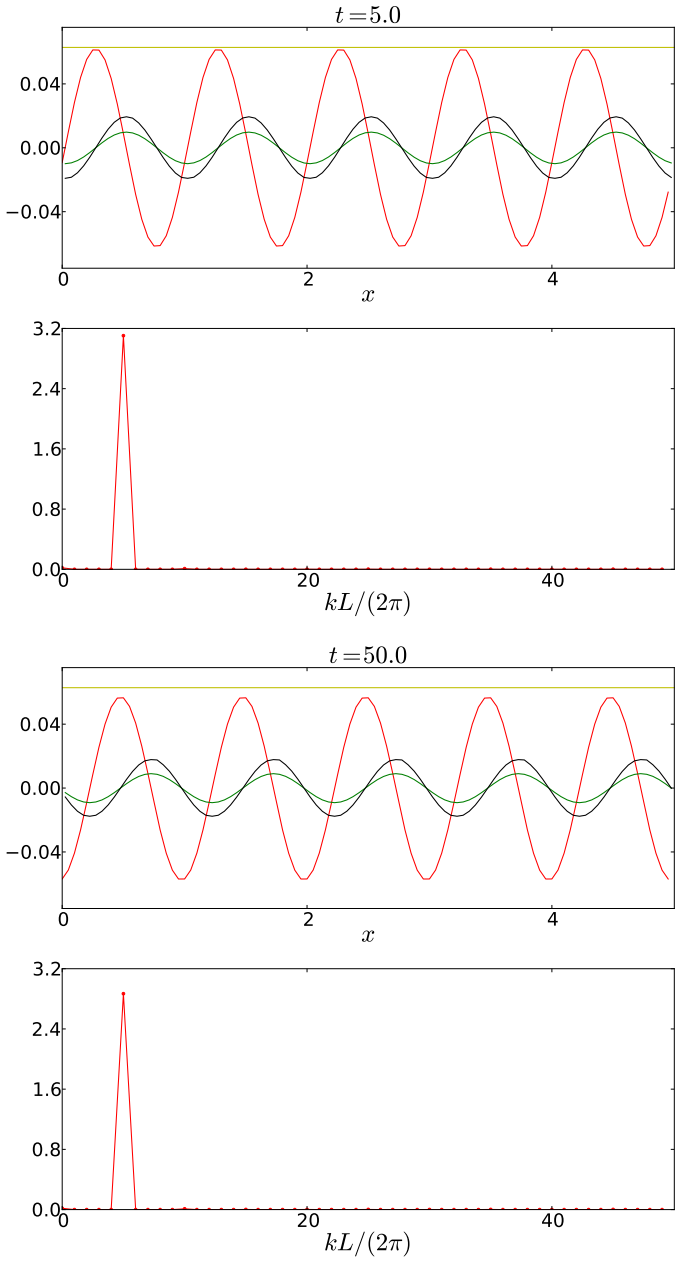

FIGURE 6.4.4. Plots of the result of the enhanced scheme (6.4.20)-(6.4.21), applied on the linear wake field problem (6.4.1)-(6.4.3) with $\Delta x = 0.05$, $\Delta t = 0.025$. The plots show the field E_x(red), the density modulation ρ_1 (black) and the fluid momentum p_x (green). The lower plots show the Fourier spectrum of E_x. Distortions of the wake field structure are significantly lower; still, one observes a slight damping.

It provides as output a linear combination

$$\left(f_j^{FCT}\right)_{j=0}^{N-1} := \left(\left(1-C_j\right) f_j^{lo} + C_j f_j^{hi}\right)_{j=0}^{N-1},$$

such that a finite volume update

$$\rho_{j+\frac{1}{2}}^{n+1} = \rho_{j+\frac{1}{2}}^{n} + \frac{\Delta t}{\Delta x}\left(f_{j+1}^{FCT} - f_j^{FCT}\right)$$

will create no new extrema in the updated solution. As the high order flux, we take the 4th order approximation (6.4.18), and for the low order flux, we stick to the Upwind scheme (6.4.10).

The new scheme reads

$$(\rho p_x)_{j+\frac{1}{2}}^{n+\frac{1}{2}} = (\rho p_x)_{j+\frac{1}{2}}^{n} + \frac{1}{2}\Delta t\,(\rho E_x)_{j+\frac{1}{2}}^{int} \tag{6.4.19}$$

$$\rho_{j+\frac{1}{2}}^{n+1} = \rho_{j+\frac{1}{2}}^{n} + \frac{\Delta t}{\Delta x}\left(f_{j+1}^{FCT} - f_j^{FCT}\right) \tag{6.4.20}$$

$$E_{x,\,j}^{n+1} = E_{x,\,j}^{n} + \Delta t\, f_j^{FCT} \tag{6.4.21}$$

$$(\rho p_x)_{j+\frac{1}{2}}^{n+1} = (\rho p_x)_{j+\frac{1}{2}}^{n+1} + \frac{1}{2}\Delta t\,(\rho E_x)_{j+\frac{1}{2}}^{int}\,. \tag{6.4.22}$$

The steps (6.4.20)-(6.4.21) constitute an explicit Euler update, but can also be replaced by a second order scheme, such as the trapezoidal leapfrog method. It should be emphasized that for small density modulations ρ_1 (linear wake field regime), this specific choice does not make any notable difference. The scheme was implemented similarly to (6.4.14)-(6.4.16) as a numerical Python test script using NumPy. The result is shown in fig. (6.4.4). One can see that the picture has improved: The distortions are significantly weaker and the wake field structure is preserved nicely even after 50 plasma oscillation periods. This indicates that this high order scheme is a candidate for a fluid integrator which could be implemented into a PIC/hydrodynamic hybrid code.

However, a finite driven three-dimensional wake field also involves plasma-oscillations which look like a standing wave. This can be observed in a plane perpendicular to the propagation direction of the driver. In full 3D simulations with Upwind-based schemes like (6.4.19)-(6.4.22), it was observed that even if 1D linear wake fields are accurately preserved, transversal distortion can occur.

Hence, a second 1D test simulation was set up. The equations do not change, and the initial conditions are almost the same. As the only difference, we set the initial momentum p_x to zero. In the linear regime with $\rho_1 \ll \rho_0$, $p_x \ll 1$, the approximate solution is

$$E_x(x,t) = E_0 \sin(2\pi x)\cos(2\pi t) \tag{6.4.23}$$

$$\rho(x,t) = \rho_0 + \rho_1 \cos(2\pi x)\cos(2\pi t) \tag{6.4.24}$$

$$p_x(x,t) = -\frac{\rho_1}{4\pi^2}\cos(2\pi x)\sin(2\pi t), \tag{6.4.25}$$

which corresponds to a standing wave. The result for this problem obtained with the enhanced scheme (6.4.19)-(6.4.22) is shown in fig. (6.4.5).

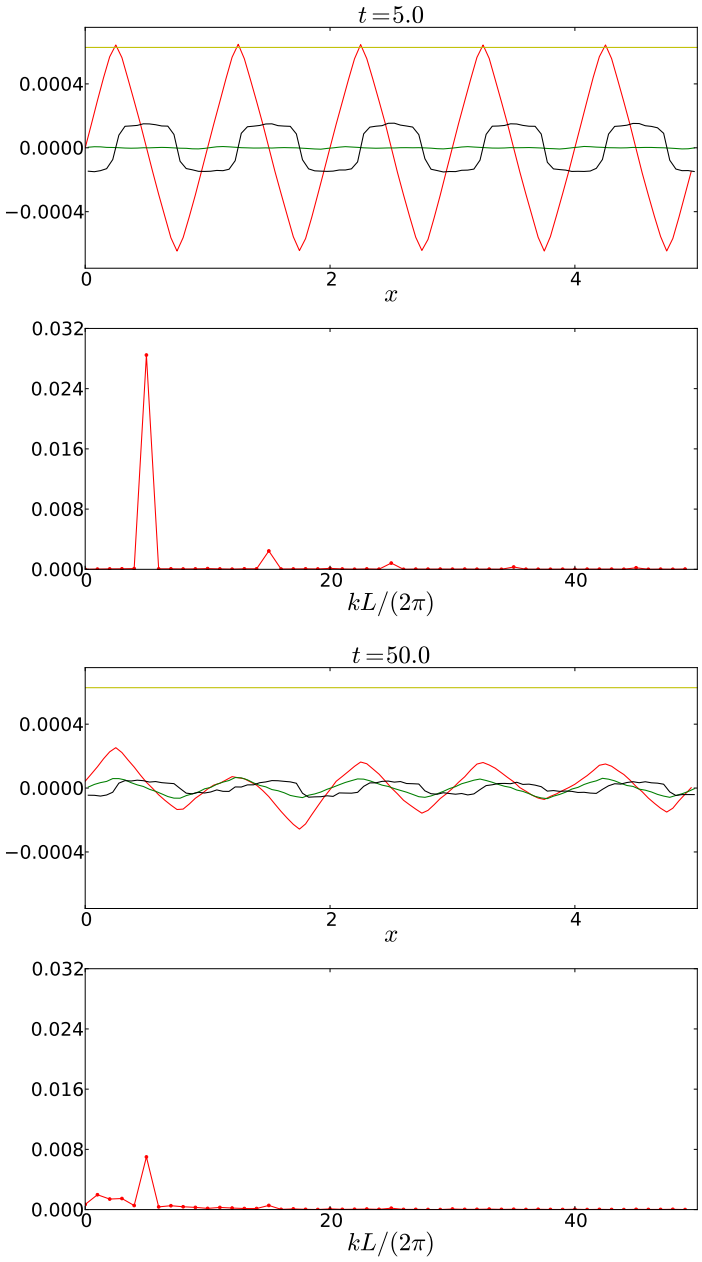

FIGURE 6.4.5. Plots of the result of the enhanced scheme (6.4.20)-(6.4.21), applied on a linear plasma oscillation problem (6.4.1)-(6.4.3) with $\Delta x = 0.05$, $\Delta t = 0.025$. The plots show the field E_x(red), the density modulation ρ_1 (black) and the fluid momentum p_x (green). The lower plots show the Fourier spectrum of E_x. After 5 plasma oscillations, a significant distortion is observed; after 50 periods, the initial structure is almost entirely lost.

Although the behaviour of this scheme for one-dimensional wake fields is promising, it clearly fails at modeling standing plasma oscillations. After $t = 5(2\pi/\omega_p)$, one sees higher harmonics of the initial E_x profile, and after 50 plasma oscillations, the structure is lost entirely. Moreover, there is also a significant damping of the amplitude of the fundamental wave.

Thorough investigations have shown that, at the maxima and minima of the initial density modulation, the FCT algorithm sets its weighting coefficient C_j to zero, thus de-activating the high order scheme. This is mostly where the unphysical distortions first occur. With passing simulation time, those distortions make the FCT algorithm set $C_j = 0$ in quickly growing regions. Due to this process, the whole spatial structure becomes randomly distorted, rendering the scheme useless. One can, of course, disable the FCT, and retreat to the high-order scheme. For this case (not shown in the figures), the wake field and standing oscillation modeling is excellent, with low damping and without any distortions. Unfortunately, this is not a feasible alternative, since such a scheme would - as previously mentioned - cause ripples, spurious oscillations e.g. at plasma boundaries, and unstable behaviour. The schemes mentioned above as well as various MUSCL-based upwind schemes, have also been tested in full 3D simulations. Likewise, significant distortions were observed.

At this point, finding a fluid scheme which works for wake fields might appear impossible.

Fortunately, it is not. Looking again closely at the problem reveals at least two possible ways out of the distortion predicament:

(1) Avoid the upwind scheme. Just a slight perturbation of the initial smooth data is enough to make FCT retreat to the Upwind flux, causing distortions, and making FCT use the Upwind flux even more, with the consequence of more distortions. So, it might suffice to find another stable, Total Variation Diminishing (TVD) scheme, which causes less perturbations than Upwind. It turns out that the Kurganov-Tadmor central scheme [**42**] is such a method.
(2) Avoid the interpolations completely. One can try to get rid of the necessity to interpolate the fields onto the cell centers, and approximate the fluxes (which resembles an interpolation onto the cell border). This can be achieved by staggering the grid, and relocating the fluid momenta from the cell centers to the cell borders, as shown in fig. 6.4.6.

For designing the new H-VLPL3D PIC/fluid hybrid code, we follow the second approach. The new grid is constructed according to fig. 6.4.6. We reformulate the equations 6.4.1-6.4.3 to primitive variables E_x, p_x, ρ:

$$\frac{\partial}{\partial t} E_x = -\rho_0 v_x \tag{6.4.26}$$

$$\frac{\partial}{\partial t} p_x = -\left(v_x \cdot \frac{\partial}{\partial x}\right) p_x + E_x \tag{6.4.27}$$

$$\frac{\partial}{\partial t} \rho = -\frac{\partial}{\partial x}(\rho v_x). \tag{6.4.28}$$

Note that the momentum equation (6.4.27) is now written in a non-conservative form. Since the momentum variables are now located at the same position as the

electric field, no interpolation is necessary anymore. However, we need a new flux approximation.

Here, we choose to adopt the FCT method again. As before, it needs a trusted low order flux and a high order flux as inputs. For the low order flux, we use the Upwind scheme again:

$$f_j^{Upw} := v_x|_j \begin{cases} \rho|^n_{j-\frac{1}{2}}, v_x|_j \geq 0 \\ \rho|^n_{j+\frac{1}{2}}, v_x|_j < 0 \end{cases} .$$

One might object that an Upwind method caused a lot of distortion in the previous investigations - so why use it here? The reason is that only the fluid density ρ undergoes this nearest-neighbour interpolation. The momenta are kept and their information is preserved. For the high-order scheme, several methods can be used. We chose to use a modified version of the Quadratic Upstream Interpolation for Convective Kinematics (QUICK) scheme [**74**]. It works by quadratic interpolation using a three-point stencil. Since one wants to interpolate the data from three cells onto a grid cell border, this stencil is not symmetrical. The three points which go into the flux scheme are chosen dynamically, dependent on the direction of the flow. This is shown in fig. 6.4.7.

Let us now derive the scheme for one grid cell. The flux we would like to derive is f_j, and the adjacent densities are $\left\{\rho_{j-\frac{3}{2}} ... \rho_{j+\frac{3}{2}}\right\}$. Without loss of generality, we assume $p_{x,\,j} \geq 0$. According to the upstream concept, the density values $\rho_{j-\frac{3}{2}}, \rho_{j-\frac{1}{2}}, \rho_{j+\frac{1}{2}}$ are used for the quadratic interpolation. The polynomial is denoted by

$$p_Q(t) = ax^2 + bx + c,$$

and we again set $\Delta x = 1$ for the sake of simplicity. The interpolation conditions are

$$\begin{aligned} \int_{j-1}^{j} p_Q(x)dx &= \rho_{j-\frac{1}{2}} \\ \int_{j}^{j+1} p_Q(x)dx &= \rho_{j+\frac{1}{2}} \\ \int_{j+1}^{j+2} p_Q(x)dx &= \rho_{j+\frac{3}{2}}. \end{aligned}$$

The solution is

$$p_Q\left(x\right) = \frac{\rho_{j+\frac{3}{2}} - 2\rho_{j+\frac{1}{2}} + \rho_{j-\frac{1}{2}}}{2}\left(x-j\right)^2 + \left(\rho_{j+\frac{1}{2}} - \rho_{j-\frac{1}{2}}\right)\left(x-j\right) + \frac{-\rho_{j+\frac{3}{2}} + 5\rho_{j+\frac{1}{2}} + 2\rho_{j-\frac{1}{2}}}{6},$$

hence the interpolated density is

$$\rho^{int}_{j,forw} = p_Q(0) = -\frac{1}{6}\rho_{j-\frac{3}{2}} + \frac{5}{6}\rho_{j-\frac{1}{2}} + \frac{1}{3}\rho_{j+\frac{1}{2}}.$$

The momentum does not need to be interpolated because it is already located at the cell interface. The coefficients for the case $p_x < 0$ are derived analogously. Thus, the final QUICK scheme reads

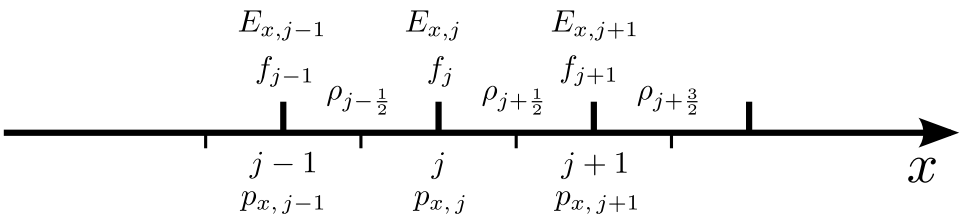

FIGURE 6.4.6. Sketch of the staggered grid approach for the fluid scheme. In contrast to the scheme depicted in fig. 6.4.2, the fluid momenta $p_{x,\,j}$ are now written as primitive variables, and located at the cell border.

$$f_j^{QUICK} := v_x|_j \begin{cases} -\frac{1}{6}\rho|^n_{j-\frac{3}{2}} + \frac{5}{6}\rho|^n_{j-\frac{1}{2}} + \frac{1}{3}\rho|^n_{j+\frac{1}{2}},\ v_x|_j \geq 0 \\ \frac{1}{3}\rho|^n_{j-\frac{1}{2}} + \frac{5}{6}\rho|^n_{j+\frac{1}{2}} - \frac{1}{6}\rho|^n_{j+\frac{3}{2}},\ v_x|_j < 0 \end{cases} .$$

Using Taylor expansion for $v_x^h > 0$, one obtains

$$\rho(i\Delta x) = \rho_{int,hi,x}|_i - \rho^{(3)}(0)\frac{1}{12}\Delta x^3 + \mathcal{O}(4)$$

for the interpolation error of the modified QUICK discretization for smooth ρ, while the order of the upwind scheme is 1. Now we have an expression for a low order Upwind flux and a third order accurate QUICK flux. These fluxes are fed into the FCT algorithm, which returns a ripple-free high-resolution flux

$$f_j^{FCT} = (1 - C_j)\, f_j^{Up} + C_j f_j^{QUICK}.$$

Omitting the convective term for now, we can write down a time-discretized splitting scheme:

$$p^{n+\frac{1}{2}}_{x,\,j} = p^n_{x,\,j} + \frac{1}{2}\Delta t E^n_{x,\,j} \tag{6.4.29}$$

$$\rho^{n+1}_{j+\frac{1}{2}} = \rho^n_{j+\frac{1}{2}} + \frac{\Delta t}{\Delta x}\left(f^{FCT}_{j+1} - f^{FCT}_j\right) \tag{6.4.30}$$

$$E^{n+1}_{x,\,j} = E^n_{x,\,j} + \Delta t\, f^{FCT}_j \tag{6.4.31}$$

$$p^{n+1}_{x,\,j} = p^{n+\frac{1}{2}}_{x,\,j} + \frac{1}{2}\Delta t E^{n+1}_{x,\,j}. \tag{6.4.32}$$

Similar to the steps (6.4.20)-(6.4.21) of the non-staggered scheme, the steps (6.4.30)-(6.4.31) in the middle constitute an explicit Euler substep. In order to make the overall scheme 2nd order accurate, one can easily employ a e.g. trapezoidal leap-frog integrator here. However, the differences are negligible in our numerical small-signal experiment. The solver (6.4.29)-(6.4.32) was again implemented as a NumPy test script and run on the plasma oscillation problem and the wake field setup.

The result for the standing plasma oscillation is shown in fig. (6.4.9). One observes an excellent modeling of the effect. There is no distortion of the spatial structure at all. Also, no damping was seen even after 200 plasma oscillation periods. Fig. 6.4.8 shows the result for the wake field test. Likewise, there is neither any distortion of the structure nor damping effects.

These outcomes make the method (6.4.29)-(6.4.32) a candidate for a fluid solver for the new hybrid code H-VLPL3D.

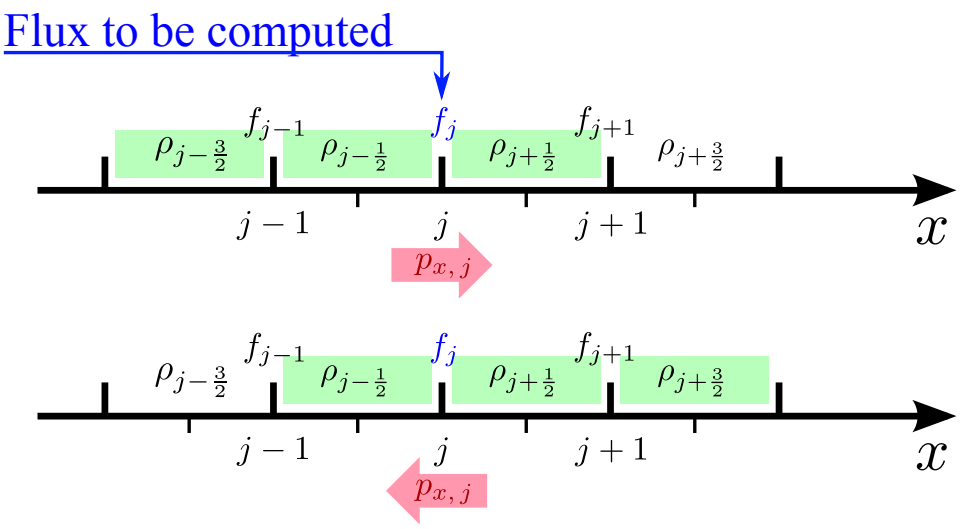

FIGURE 6.4.7. Principle of the modified QUICK flux scheme. If $p_{x,j} \geq 0$, a quadratic interpolation polynomial is computed from two values on the left side and one on the right side. Vice versa, if $p_{x,j} < 0$, the polynomial is computed from one left and two right values.

Of course, it must be evaluated whether the scheme also works in the nonlinear wake field regime. In the next chapters, the scheme will be generalized to multidimensions, and tested with a variety of physical examples.

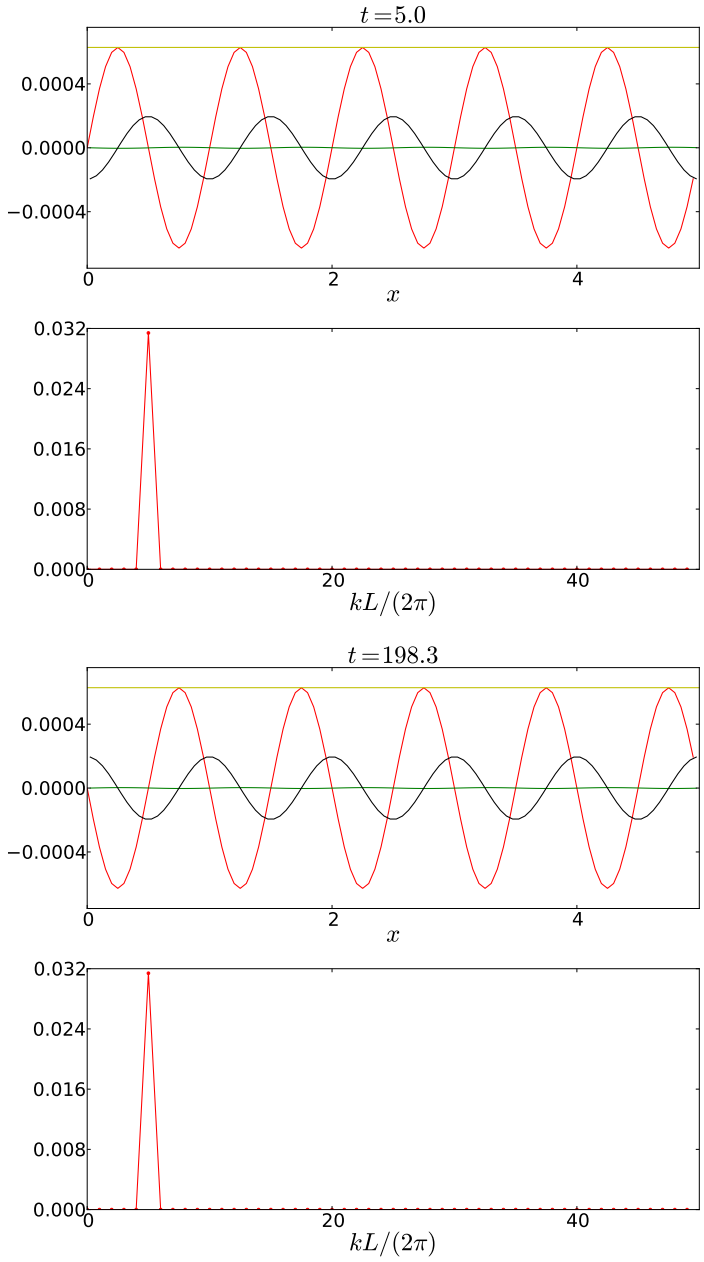

FIGURE 6.4.9. Plots of the result of the staggered scheme (6.4.29)-(6.4.32), tested with the linear plasma oscillation problem. The plots show the field E_x(red), the density modulation ρ_1 (black) and the fluid momentum p_x (green). The lower plots show the Fourier spectrum of E_x. Similarly to the wake field result shown in fig. (6.4.8), the algorithm excels at modeling the plasma oscillation.

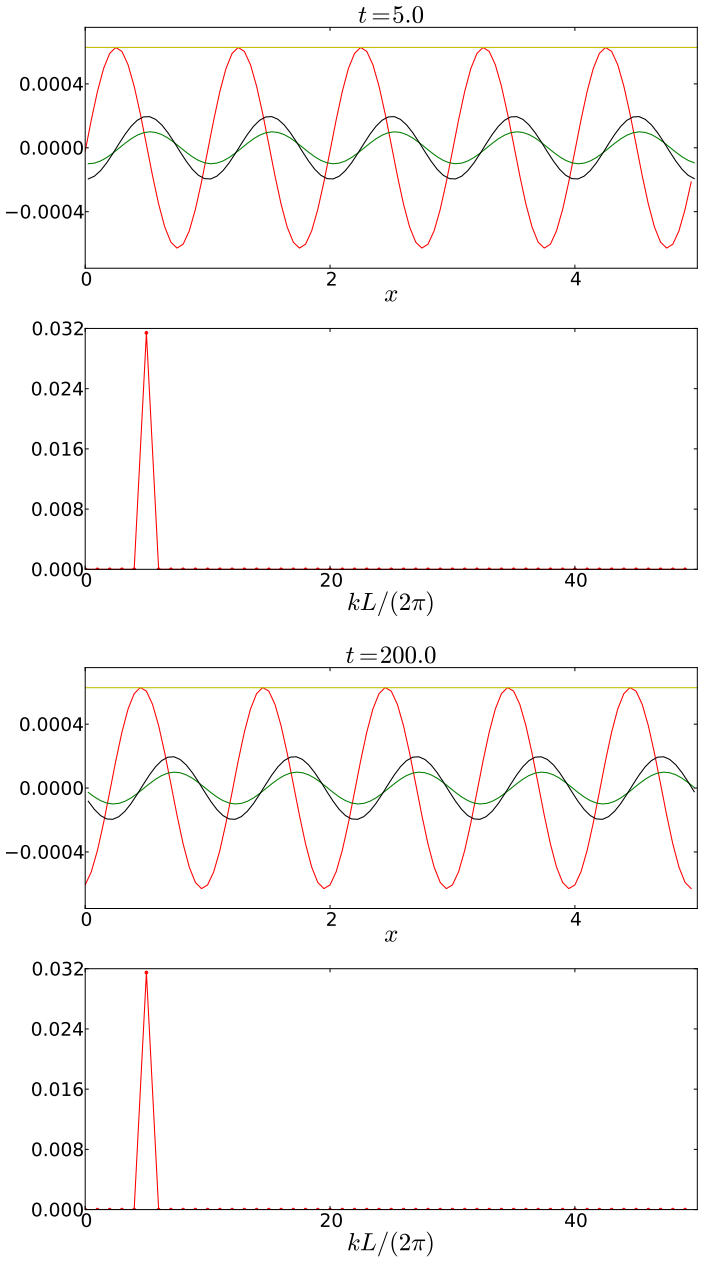

FIGURE 6.4.8. Plots of the result of the staggered scheme (6.4.29)-(6.4.32), applied on the linear plasma wake field problem. The plots show the field E_x(red), the density modulation ρ_1 (black) and the fluid momentum p_x (green). The lower plots show the Fourier spectrum of E_x. There is no distortion or damping present; the spatial structure is unaltered even after 200 oscillation periods.

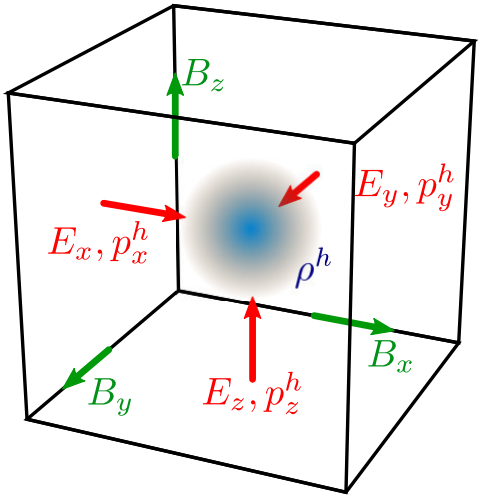

FIGURE 6.5.1. Geometry of the spatial discretization scheme for electromagnetic field quantities as well as fluid variables. Losses are minimized by aligning the positions of the fluid momentum components with the electric field locations.

6.5. Spatial scheme for the continuity equation

The scheme developed in chapter 6.4 has been shown to work exceptionally well in the linear wake regime of one-dimensional wake fields and plasma oscillations. So, the next task will be to generalize it to three dimensions and test its capability in the linear as well as the non-linear regimes. This will be done in the next sections.

For the 3D discretization, we again choose a staggered grid for the spatial fluid modeling, with the numerical density as an integral over the cell volume, but momenta located on the cell faces:

$$\rho|^n_{i+\frac{1}{2},j+\frac{1}{2},k+\frac{1}{2}} := \int_{Cell} \int \int \rho(\vec{r}, n\Delta t) d^3r$$

$$p_x^h|^n_{i,j+\frac{1}{2},k+\frac{1}{2}} := \int_{j\Delta y}^{(j+1)\Delta y} \int_{k\Delta z}^{(k+1)\Delta z} p_x^h(i\Delta x, y, z, n\Delta t) dz dy,$$

with the other two momentum components defined analogously. This grid configuration is depicted in figure 6.5.1. Analogously to the 1D case, the staggered grid is chosen in a way that the fluid momenta are collocated with the respective electric field components. This is done in order to avoid interpolations of the electric fields and momenta and significantly improve the modeling of plasma oscillations. Since, for this special grid scheme, spatial discretization schemes are rare, we have constructed a new scheme, following the concept of the QUICKEST technique.

The FCT [**44**] method used in the 1D scheme in chapter 6.4 is readily generalized to three dimensions. The multidimensional algorithm again takes as input a low order flux $\vec{f}_{\rho,low}$, a high order flux $\vec{f}_{\rho,hi}$, a quantity ρ to be updated, and the time step Δt.

A general semi-discretized 1D Finite Volume Method (FVM) for a quantity $u = \left(u_{i+\frac{1}{2}}\right)_{i=0}^{n-1}$ is defined as

$$\frac{\partial}{\partial t} u_{i+\frac{1}{2}} = -\frac{1}{\Delta x}\left(f_{i+1}^{1D}(u) - f_i^{1D}(u)\right);$$

the whole algorithm is then contained in the approximated flux function $f_i^{1D}(u)$. Such a method can be easily generalized to multidimensions by computing the 1D fluxes of each variable along each spatial direction,

$$\begin{aligned}
f_x|_{i,\,j+\frac{1}{2},\,k+\frac{1}{2}} &= f_i^{1D}\left(\left(u_{\alpha+\frac{1}{2},\,j+\frac{1}{2},\,k+\frac{1}{2}}\right)_{\alpha=0}^{n_x-1}\right),\\
f_y|_{i+\frac{1}{2},\,j,\,k+\frac{1}{2}} &= f_j^{1D}\left(\left(u_{i+\frac{1}{2},\,\alpha+\frac{1}{2},\,k+\frac{1}{2}}\right)_{\alpha=0}^{n_y-1}\right),\\
f_z|_{i+\frac{1}{2},\,j+\frac{1}{2},\,k} &= f_k^{1D}\left(\left(u_{i+\frac{1}{2},\,j+\frac{1}{2},\,\alpha+\frac{1}{2}}\right)_{\alpha=0}^{n_z-1}\right),
\end{aligned}$$

and arrange these fluxes as a vector:

$$\vec{f}^{3D} = \begin{bmatrix} f_x^{1D} \\ f_y^{1D} \\ f_z^{1D} \end{bmatrix} \tag{6.5.1}$$

It should be pointed out that in the literature one often distinguishes the abovementioned concept from inherently multidimensional schemes. The latter ones always stem from multidimensional considerations from the very beginning. Thus, they can usually not be written as a vector with 1D fluxes as components (as in eq.(6.5.1)). They are generally considered to be more accurate and stable. Numerical artifacts like smearing in transverse motions are avoided to some degree.

However, they are not necessary unless complicated fluid problems are to be simulated. It will turn out that our scheme works satisfactory even with the simple generalization (6.5.1). Following that idea, the 3D upwind flux reads

$$\begin{aligned}
&(f_{\rho,low,x}|_{i,j+\frac{1}{2},k+\frac{1}{2}}, f_{\rho,low,y}|_{i+\frac{1}{2},j,k+\frac{1}{2}}, f_{\rho,low,z}|_{i+\frac{1}{2},,j+\frac{1}{2},k}) :=\\
&(v_x^h|_{i,j+\frac{1}{2},k+\frac{1}{2}} \begin{cases} \rho|_{i-\frac{1}{2},j+\frac{1}{2},k+\frac{1}{2}}^n, v_x^h|_{i,j+\frac{1}{2},k+\frac{1}{2}} \geq 0 \\ \rho|_{i+\frac{1}{2},j+\frac{1}{2},k+\frac{1}{2}}^n, v_x^h|_{i,j+\frac{1}{2},k+\frac{1}{2}} < 0 \end{cases},\\
&v_y^h|_{i+\frac{1}{2},,j,k+\frac{1}{2}} \begin{cases} \rho|_{i+\frac{1}{2},j-\frac{1}{2},k+\frac{1}{2}}^n, v_y^h|_{i+\frac{1}{2},j,k+\frac{1}{2}} \geq 0 \\ \rho|_{i+\frac{1}{2},j+\frac{1}{2},k+\frac{1}{2}}^n, v_y^h|_{i+\frac{1}{2},j,k+\frac{1}{2}} < 0 \end{cases},\\
&v_z^h|_{i+\frac{1}{2},,j+\frac{1}{2},k} \begin{cases} \rho|_{i+\frac{1}{2},j+\frac{1}{2},k-\frac{1}{2}}^n, v_z^h|_{i+\frac{1}{2},j+\frac{1}{2},k} \geq 0 \\ \rho|_{i+\frac{1}{2},j+\frac{1}{2},k+\frac{1}{2}}^n, v_z^h|_{i+\frac{1}{2},j+\frac{1}{2},k} < 0 \end{cases}.)
\end{aligned}$$

Similarly, the high order QUICK scheme is computed by arranging three one-dimensional flux schemes into a vector.

$$\begin{bmatrix} f_{\rho,hi,x}|_{i,j+\frac{1}{2},k+\frac{1}{2}} \\ f_{\rho,hi,y}|_{i+\frac{1}{2},j,k+\frac{1}{2}} \\ f_{\rho,hi,z}|_{i+\frac{1}{2},,j+\frac{1}{2},k} \end{bmatrix} := \begin{bmatrix} v_x^h|_{i,j+\frac{1}{2},k+\frac{1}{2}} \rho_{int,hi,x}|_{i,j+\frac{1}{2},k+\frac{1}{2}} \\ v_y^h|_{i+\frac{1}{2},j,k+\frac{1}{2}} \rho_{int,hi,y}|_{i+\frac{1}{2},j,k+\frac{1}{2}} \\ v_z^h|_{i+\frac{1}{2},j+\frac{1}{2},k} \rho_{int,hi,z}|_{i+\frac{1}{2},j+\frac{1}{2},k} \end{bmatrix},$$

where

$$\rho_{int,hi,x}|_{i,j+\frac{1}{2},k+\frac{1}{2}} := \begin{cases} -\frac{1}{6}\rho|^n_{i-\frac{3}{2},j+\frac{1}{2},k+\frac{1}{2}} + \frac{5}{6}\rho|^n_{i-\frac{1}{2},j+\frac{1}{2},k+\frac{1}{2}} \\ \quad +\frac{1}{3}\rho|^n_{i+\frac{1}{2},j+\frac{1}{2},k+\frac{1}{2}},\ v^h_x|_{i,j+\frac{1}{2},k+\frac{1}{2}} \geq 0 \\ \frac{1}{3}\rho|^n_{i-\frac{1}{2},j+\frac{1}{2},k+\frac{1}{2}} + \frac{5}{6}\rho|^n_{i+\frac{1}{2},j+\frac{1}{2},k+\frac{1}{2}} \\ \quad -\frac{1}{6}\rho|^n_{i+\frac{3}{2},j+\frac{1}{2},k+\frac{1}{2}},\ v^h_x|_{i,j+\frac{1}{2},k+\frac{1}{2}} < 0 \end{cases}$$

$$\rho_{int,hi,y}|_{i+\frac{1}{2},j,k+\frac{1}{2}} := \begin{cases} -\frac{1}{6}\rho|^n_{i+\frac{1}{2},j-\frac{3}{2},k+\frac{1}{2}} + \frac{5}{6}\rho|^n_{i+\frac{1}{2},j-\frac{1}{2},k+\frac{1}{2}} \\ \quad +\frac{1}{3}\rho|^n_{i+\frac{1}{2},j+\frac{1}{2},k+\frac{1}{2}},\ v^h_y|_{i+\frac{1}{2},j,k+\frac{1}{2}} \geq 0 \\ \frac{1}{3}\rho|^n_{i+\frac{1}{2},j-\frac{1}{2},k+\frac{1}{2}} + \frac{5}{6}\rho|^n_{i+\frac{1}{2},j+\frac{1}{2},k+\frac{1}{2}} \\ \quad -\frac{1}{6}\rho|^n_{i+\frac{1}{2},j+\frac{3}{2},k+\frac{1}{2}},\ v^h_y|_{i+\frac{1}{2},j,k+\frac{1}{2}} < 0 \end{cases}$$

$$\rho_{int,hi,z}|_{i+\frac{1}{2},j+\frac{1}{2},k} := \begin{cases} -\frac{1}{6}\rho|^n_{i+\frac{1}{2},j+\frac{1}{2},k-\frac{3}{2}} + \frac{5}{6}\rho|^n_{i+\frac{1}{2},j+\frac{1}{2},k-\frac{1}{2}} \\ \quad +\frac{1}{3}\rho|^n_{i+\frac{1}{2},j+\frac{1}{2},k+\frac{1}{2}},\ v^h_z|_{i+\frac{1}{2},j+\frac{1}{2},k} \geq 0 \\ \frac{1}{3}\rho|^n_{i+\frac{1}{2},j+\frac{1}{2},k-\frac{1}{2}} + \frac{5}{6}\rho|^n_{i+\frac{1}{2},j+\frac{1}{2},k+\frac{1}{2}} \\ \quad -\frac{1}{6}\rho|^n_{i+\frac{1}{2},j+\frac{1}{2},k+\frac{3}{2}},\ v^h_z|_{i+\frac{1}{2},j+\frac{1}{2},k} < 0 \end{cases} .$$

The FCT algorithm then provides coefficients

$$C_{\rho,x}|_{i,j+\frac{1}{2},k+\frac{1}{2}}, C_{\rho,y}|_{i+\frac{1}{2},j,k+\frac{1}{2}}, C_{\rho,z}|_{i+\frac{1}{2},j+\frac{1}{2},k},$$

such that

$$\begin{bmatrix} f_{\rho,FCT,x}|_{i,j+\frac{1}{2},k+\frac{1}{2}} \\ f_{\rho,FCT,y}|_{i+\frac{1}{2},j,k+\frac{1}{2}} \\ f_{\rho,FCT,z}|_{i+\frac{1}{2},j+\frac{1}{2},k} \end{bmatrix} := \begin{bmatrix} f_{\rho,lo,x}|_{i,j+\frac{1}{2},k+\frac{1}{2}} + C_{\rho,x}|_{i,j+\frac{1}{2},k+\frac{1}{2}}(f_{\rho,hi,x}|_{i,j+\frac{1}{2},k+\frac{1}{2}} - f_{\rho,lo,x}|_{i,j+\frac{1}{2},k+\frac{1}{2}}) \\ f_{\rho,lo,y}|_{i+\frac{1}{2},j,k+\frac{1}{2}} + C_{\rho,y}|_{i+\frac{1}{2},j,k+\frac{1}{2}}, (f_{\rho,hi,y}|_{i+\frac{1}{2},j,k+\frac{1}{2}} - f_{\rho,lo,y}|_{i+\frac{1}{2},j,k+\frac{1}{2}}) \\ f_{\rho,lo,z}|_{i+\frac{1}{2},j+\frac{1}{2},k} + C_{\rho,z}|_{i+\frac{1}{2},j+\frac{1}{2},k}(f_{\rho,hi,z}|_{i+\frac{1}{2},j+\frac{1}{2},k} - f_{\rho,lo,z}|_{i+\frac{1}{2},j+\frac{1}{2},k}) \end{bmatrix}$$

will achieve high accuracy in regions with low gradients in density while maintaining positivity and monotonicity. It should be mentioned that charge conservation is maintained very easily, since with the finite difference operator

$$\hat{d}_\alpha u|_{i+\frac{1}{2},,j+\frac{1}{2},k+\frac{1}{2}} := \begin{cases} \frac{1}{\Delta x}(u_{i+1,j+\frac{1}{2},k+\frac{1}{2}} - u_{i,j+\frac{1}{2},k+\frac{1}{2}}), & \alpha = x \\ \frac{1}{\Delta y}(u_{i+\frac{1}{2},j+1,k+\frac{1}{2}} - u_{i+\frac{1}{2},j,k+\frac{1}{2}}), & \alpha = y \\ \frac{1}{\Delta z}(u_{i+\frac{1}{2},j+\frac{1}{2},k+1} - u_{i+\frac{1}{2},j+\frac{1}{2},k}), & \alpha = z \end{cases}$$

for a staggered-grid variable u, Gauss' law can be rewritten into the discrete form

$$(\sum_{\alpha=x,y,z} \hat{d}_\alpha E_\alpha|_{i+\frac{1}{2},j+\frac{1}{2},k+\frac{1}{2}}) - \rho|_{i+\frac{1}{2},j+\frac{1}{2},k+\frac{1}{2}} = \text{const.}$$

This will always be satisfied if, given a flux approximation

$$(f_{\rho,x}|_{i,j+\frac{1}{2},k+\frac{1}{2}}, f_{\rho,y}|_{i+\frac{1}{2},j,k+\frac{1}{2}} f_{\rho,z}|_{i+\frac{1}{2},j+\frac{1}{2},k}),$$

one keeps updating the electric field and density at the same time.

6.6. Semi-Lagrange convective scheme

For high-accuracy wake field simulations, the scheme for the density equation constitutes the most critical part of the spatial discretization. This is why the staggered grid convention was chosen, combining the advantages of an interpolation-free momentum update, simple flux calculation and perfect charge conservation. However, this grid poses a challenge regarding the design of a discretization of the convective term in the momentum update. That problem is adressed via a semi-Lagrange advection scheme, processing each momentum component independently. It reads as follows:

(1) Given $\alpha \in \{x, y, z\}$, interpolate the remaining two momentum components symmetrically to the position of p^h_α, precisely

$$\begin{aligned}(p_x^{h,int}|_{i,j+\frac{1}{2},k+\frac{1}{2}}, p_y^{h,int}|_{i,j+\frac{1}{2},k+\frac{1}{2}}, p_z^{h,int}|_{i,j+\frac{1}{2},k+\frac{1}{2}}) := \\ p^h_x|_{i,j+\frac{1}{2},k+\frac{1}{2}}, \\ \frac{1}{4}(p^h_y|_{i+\frac{1}{2},j,k+\frac{1}{2}} + p^h_y|_{i-\frac{1}{2},j,k+\frac{1}{2}} + \\ p^h_y|_{i+\frac{1}{2},j+1,k+\frac{1}{2}} + p^h_y|_{i-\frac{1}{2},j+1,k+\frac{1}{2}}), \\ \frac{1}{4}(p^h_z|_{i+\frac{1}{2},j+\frac{1}{2},k} + p^h_z|_{i-\frac{1}{2},j+\frac{1}{2},k} + \\ p^h_z|_{i+\frac{1}{2},j+\frac{1}{2},k+1} + p^h_z|_{i-\frac{1}{2},j+\frac{1}{2},k+1})\end{aligned}$$

for the x-component; the other momentum components are computed analogously.

(2) From these three localized momentum vectors, calculate three velocities

$$(\mathbf{v}^{h,int,x}|_{i,j+\frac{1}{2},k+\frac{1}{2}}, \mathbf{v}^{h,int,y}|_{i+\frac{1}{2},j,k+\frac{1}{2}}, \mathbf{v}^{h,int,z}|_{i+\frac{1}{2},j+\frac{1}{2},k})$$

with

$$\mathbf{v}^{h,int,x}|_{i,j+\frac{1}{2},k+\frac{1}{2}} = \frac{\mathbf{p}^{h,int,x}|_{i,j+\frac{1}{2},k+\frac{1}{2}}}{\sqrt{1+\mathbf{p}^{h,int,x}|^2_{i,j+\frac{1}{2},k+\frac{1}{2}}}}$$

(3) Using these velocities, back-track the trajectories of virtual particles:

$$\begin{aligned}&\mathbf{r}^{1,x} := \\ &(i\Delta x, (j+\frac{1}{2})\Delta y, (k+\frac{1}{2})\Delta z) - \Delta t \mathbf{v}^{h,int,x}|_{i,j+\frac{1}{2},k+\frac{1}{2}}\end{aligned}$$

$$\begin{aligned}\lambda_x &:= -v_x^{h,int,x}|_{i,j+\frac{1}{2},k+\frac{1}{2}} \frac{\Delta t}{\Delta x} \\ \sigma_x &:= sgn(\lambda_x)\end{aligned}$$

etc.

(4) Obtain the interpolated momenta at the new positions $\mathbf{r}^{1,x}, \mathbf{r}^{1,y}, \mathbf{r}^{1,z}$ and use them as the updated solution.

Since the error of the semi-Lagrange scheme can also cause significant damping in the solution, the interpolation scheme for 4 must be chosen carefully. Since trilinear interpolation does not suffice, we use the monotonicity preserving cubic interpolation scheme from [**75**]. This scheme is then extended to a 3D monotone tricubic method by cycling through the dimensions.

The semi-Lagrangian solver for the hydrodynamic momentum is then arranged symmetrically around a central part consisting of the differential equations stated below. These equations can be written in a spatially discretized, semi-discrete form:

$$\frac{\partial}{\partial t}E_x|_{i,j+\frac{1}{2},k+\frac{1}{2}} = -qf_{\rho,FCT,x}|_{i,j+\frac{1}{2},k+\frac{1}{2}} \tag{6.6.1}$$

$$\frac{\partial}{\partial t}\rho^h|_{i+\frac{1}{2},j+\frac{1}{2},k+\frac{1}{2}} = -\sum_{\alpha=x,y,z}\hat{d}f_{\rho,FCT,\alpha}|_{i+\frac{1}{2},j+\frac{1}{2},k+\frac{1}{2}} \tag{6.6.2}$$

$$\frac{\partial}{\partial t}p^h|_{i,j+\frac{1}{2},k+\frac{1}{2}} = qE_x|_{i,j+\frac{1}{2},k+\frac{1}{2}} \tag{6.6.3}$$

6.7. Time discretization

The new H-VLPL3D simulation code follows a modular concept, which means that there are few cross-dependencies between different numerical code sections. This is why various time integrator schemes can be implemented very easily.

The fluid integrator is nested into the Maxwell solver as follows:

(1) $\mathbf{B}^n \to \mathbf{B}^{n+1/2}$
(2) $\mathbf{E}^n \to \mathbf{E}^{n+1/2}$
(3) $\mathbf{p}^{h,n} \to \mathbf{p}^{h,A}$(Semi-Lagrange step)
(4) $\mathbf{p}^{h,A} \to \mathbf{p}^{h,B}$(Magnetic Lorentz force push)
(5) $\mathbf{p}^{h,B} \to \mathbf{p}^{h,*}$(Electric force)
(6) $(\rho^{h,n}, \mathbf{E}^{n+1/2}) \to (\rho^{h,n+1}, \mathbf{E}^*)$
(7) $\mathbf{p}^{h,*} \to \mathbf{p}^{h,C}$(Electric force)
(8) $\mathbf{p}^{h,C} \to \mathbf{p}^{h,D}$(Magnetic Lorentz force push)
(9) $\mathbf{p}^{h,D} \to \mathbf{p}^{h,n+1}$(Semi-Lagrange step)
(10) $\mathbf{E}^* \to \mathbf{E}^{n+1}$
(11) $\mathbf{B}^{n+1/2} \to \mathbf{B}^{n+1}$

The steps 1,2,10,11 implement a splitting solver for the well known FDTD Yee scheme. As stated in section 3.4, splitting schemes are constructed from exact solutions of reduced differential equations. Thus, steps 1 and 11 solve the reduced equation

$$\frac{\partial}{\partial t}\mathbf{B} = -\nabla \times \mathbf{E}$$
$$\frac{\partial}{\partial t}\mathbf{E} = 0$$

exactly. Steps 2 and 10 work in a similar fashion. Considering the steps 5 and 7 shows one main advantage of

the staggered scheme with primitive variables, because the reduced equation

$$\frac{\partial}{\partial t}\mathbf{p}^h = q\mathbf{E}$$
$$\frac{\partial}{\partial t}\mathbf{E} = 0$$

can as well be solved exactly in a straightforward manner. The steps 4 and 8 implement a Boris push.

As opposed to the steps mentioned before, there are no simple exact solutions for step 6. Instead, we need a one-step time integrator of at least second order accuracy. Up to now, H-VLPL3D contains a 2nd order Runge solver as well as 2nd and 3rd order Heun schemes for this step.

In the remaining steps 3 and 9, the reduced differential equation

$$\frac{\partial}{\partial t}\mathbf{p}^h = -(\mathbf{v}^h \cdot \nabla)\mathbf{p}^h$$

resembles a relativistic inviscid Burgers equation. It was found that the semi-Lagrange algorithm depicted above, arranged as a predictor-corrector scheme, achieves good results.

6.8. Implementation

This optimized fluid discretization scheme has been combined with the existing particle-in-cell implementation of VLPL, forming the H-VLPL3D hybrid code. The fluid solver is nested into the existing time step. Fluid densities and momenta are stored using the `Grid<T>` grid storage template class, hence the algorithms are readily parallelized with MPI. The grid information can be naturally fed into VLPLs existing data storage system in order to achieve easy output of simulation results.

The fluid system allows for the definition of arbitrary boundary conditions, e.g. in order to let plasma flow into the box from its border. This is also possible when the moving box mode is enabled. If desired, new time integrators for (6.6.1)-(6.6.3) can be implemented within minutes, and the `v.ini` files then let the user choose between the schemes. Inside the job initialization files, fluid plasma species can be defined the same way as PIC species. With recent enhancements, one can also define multiple fluid species.

The hybrid functionality of H-VLPL3D can be turned on and off easily.

6.9. Properties and benchmarking results

The novel H-VLPL PIC-fluid hybrid code unites the simulational capabilities and richness of the particle-in-cell algorithm with the efficiency, smoothness and speed of a hydrodynamic plasma description. In this section, we demonstrate its correctness using various physical examples. The grid geometry convention of the fluid data as well as the spatial discretization pattern has been designed with particular emphasis on noiseless, highly accurate simulations of driven plasma oscillations, which are encountered in the laser wake field acceleration (LWFA) or the plasma wake field acceleration (PWFA) regimes. Therefore, we pay particular attention to the code's performance in modeling wake field setups.

In order to quantify the new system's spatial accuracy, we have carried out a sequence of one-dimensional test computations. The grid step h_x is varied from

0.1 to 0.01, and the result for the electric field is compared to a high-resolution reference simulation. The max norm of the error is shown in figure 6.9.1.

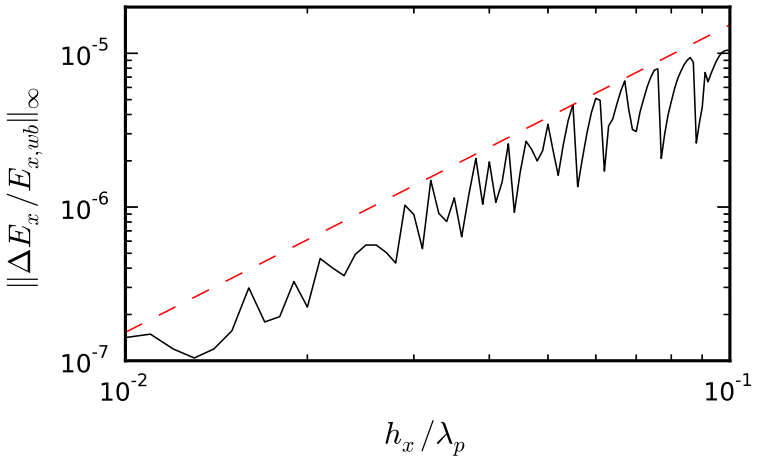

FIGURE 6.9.1. Error analysis using a series of wake field test simulations. The error curve indicates second order spatial accuracy.

6.10. Interaction with electromagnetic waves

As a first test for the code's correctness, it is benchmarked against a conventional PIC code (VLPL) in a simple refraction experiment. A narrow, short virtual laser beam is targeted onto a plasma surface dividing the simulation box into two equal parts. The plasma consists of electrons, with a density of zero in the left half and $n_e = n_c/2$ in the right half, where n_c denotes the critical density corresponding to the laser frequency. This plasma is modeled with the conventional PIC code for a reference simulation as well as the new hybrid extension. The results are shown in figure 6.10.1; as it can be easily seen, the linear plasma response is reproduced very accurately.

6.11. Wake field simulations

The test simulation for the driven wake field regime is set up as follows: Given the background plasma wavelength λ_p, we choose a virtual box of size $(L_x, L_y, L_z) = (32, 1.5, 1.5)\lambda_p$ covered by an equidistant grid with resolution

$$(h_x, h_y, h_z) = (0.05, 0.06, 0.06)\,\lambda_p.$$

A homogeneous background with density $\rho_h = \rho_{\text{plasma}}$ with $\rho_{\text{plasma}} = (\pi mc^2)/(e^2\lambda_p^2)$ is set to consist of electrons, represented as a fluid. A proton bunch is put next to the right wall of the box, with $\rho_p = 0.1\rho_{\text{plasma}} \exp(-(x/\sigma_x)^2 - (x/\sigma_y)^2)$, $\sigma_x = 0.17\lambda_p$, $\sigma_r = 0.2\lambda_p$ and momentum $\vec{p} = (479mc, 0, 0)$. The simulation runs with a moving frame, keeping the position of the proton bunch in virtual grid coordinates constant. Figure 6.11.1 shows a snapshot of this setup after $t = 40T_p$, where $T_p = \lambda_p/c$. The 3D visualization has been cut to show only the right part of the box, with $x \in [25.6, 32]$, for the sake of simplicity. As depicted, the proton bunch excites a wake field with a background density modulation of $\sim 15\%$. One observes a very

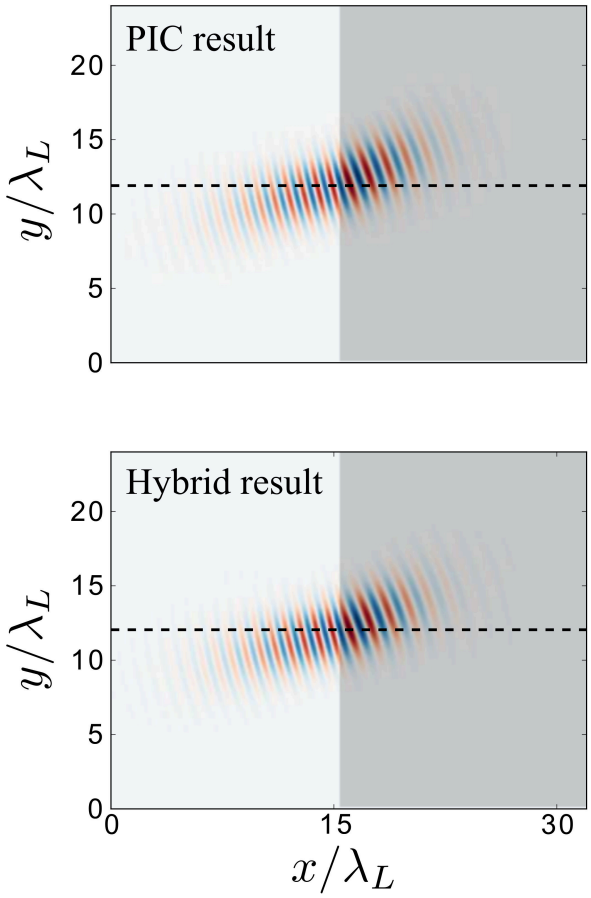

FIGURE 6.10.1. Snapshot of a linear refraction test of the hybrid code. The plasma surface is a jump discontinuity from $n_e = 0$ to $n_e = \frac{1}{2}n_c$.

smooth and accurate modeling of the effect, with very short simulation time. In order to cross-check and accentuate the advantage of this model, we initialize hybrid and conventional PIC simulations of the same geometry, with $n_p = 0.001$, with a comparison shown in figure 6.11.2. The first picture shows the result obtained with the H-VLPL code, while the second one has been created replacing the fluid representation by PIC macroparticles. This simulation suffers from heavy diffusion due to repeated interpolations required by the kinetic scheme. Now one could expect that increasing the number of particles per cell could alleviate this effect; on the contrary, the diffusion becomes worse with more macroparticles changing their grid cell location more frequently and causing additional loss of information.
For the sake of clarity about the solution of this problem, we repeat the simulation with one half of the initial grid steps (causing a 16 times longer simulation, third image in figure 6.11.2) and one quarter of the initial step (causing a 256 times

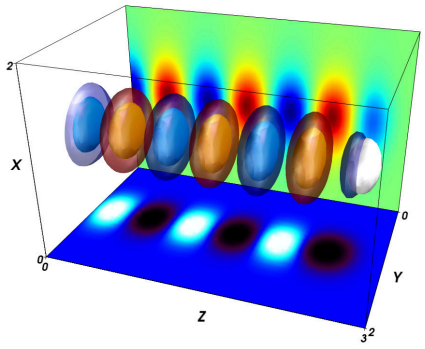

FIGURE 6.11.1. Snapshot of a hybrid simulation of a proton driven wake field at time $t = 40T_{\text{plasma}}$. The color plot attached to the bottom wall shows the density modulation of the fluid. The back wall image as well as the blue and orange iso surfaces illustrate the E_x electric field component.

longer simulation, fourth image). A convergent behaviour of this data is obvious. We again point out that while PIC algorithms are still unmatched in their richness, their continuous loss of information makes them need an overall simulation size orders of magnitude larger in order to reproduce the hybrid result.

An additional benchmark is done by testing the hybrid code in the highly nonlinear regime of wake field excitation. A dense, high energy gaussian proton bunch with $n_{p,\max} = 0.3n_{\text{plasma}}$is made to propagate through a background plasma with constant density ρ_{ref}. Results at $t = 20T_p$ are shown in figure 6.11.3. Here, the density fluctuation is as high as $\frac{1}{2}\rho_{\text{plasma}}$, making convective effects significant. Again, one notices that the hydrodynamic algorithm succeeds at reproducing the nonlinear steepening of the wave, but without the noise a PIC code would generate.

As a last benchmark, we have measured quantitatively the non-physical damping in driven plasma oscillations. Again, a driver pulse was made to propagate through a fluid plasma, exciting wake fields. The on-axis E_x component was extracted and its amplitude was calculated via FFT. Then, a parametric exponential function $E_{x,fit}(x) := E_0 \exp(-x/\lambda_{\text{decay}})$ was fitted to E_x with linear regression for the constants $E_0, \lambda_{\text{decay}}$. A typical result is shown in figure (6.11.4), where for a driver density of $n_d = 0.1$ the $1/e$ length was as large as $5559\lambda_p$.

Even for higher driver densities, the damping was very low, with the lowest $1/e$ length observed being $\sim 750\lambda_p$.

6.12. Summary

In this chapter, a comprehensive description of the novel H-VLPL3D PIC/fluid hybrid code was given. The basic fluid equations as well as the schemes for the spatial and temporal discretization have been presented. Furthermore, I have described the challenges, and the solutions for finding an algorithm capable of modeling wake fields with low distortions. The H-VLPL3D implementation was then successfully tested on various physical examples.

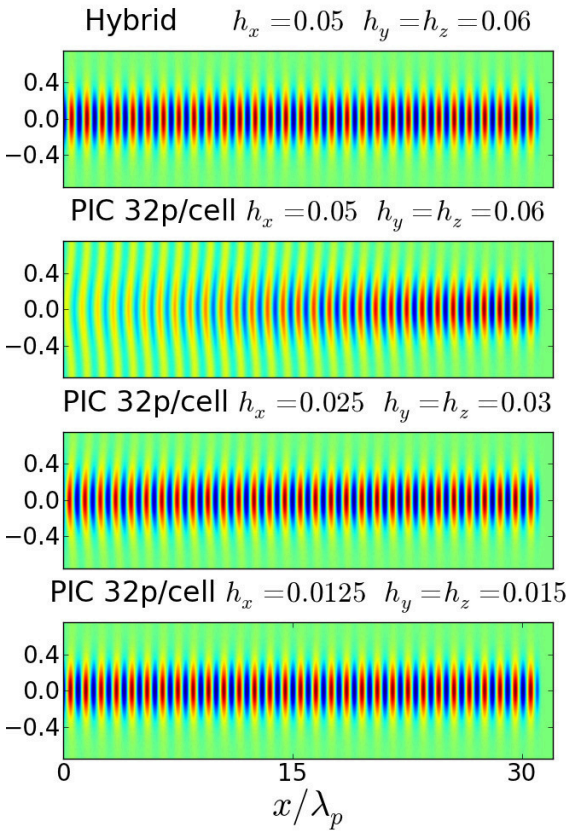

FIGURE 6.11.2. Snapshot of the E_x component of four simulations of the setup depicted on page 82 after $t = 40T_{ref}$. The wake field was excited by a proton bunch driver, which is located just at the right box wall. The PIC simulations have been computed with increasing resolution, showing clearly that the latter suffer from numerical diffusion of the electric field information while converging towards the hybrid result.

The results depicted above give a good justification for the H-VLPL3D code. For the regime of very long wake fields without wave-breaking, it is far more accurate and efficient than the PIC method.

Its break-out capability of modeling such high numbers of plasma oscillations immediately finds its first application: Chapter 7 describes how this code has been used in the simulation of self-modulation effects of long proton bunches in plasma.

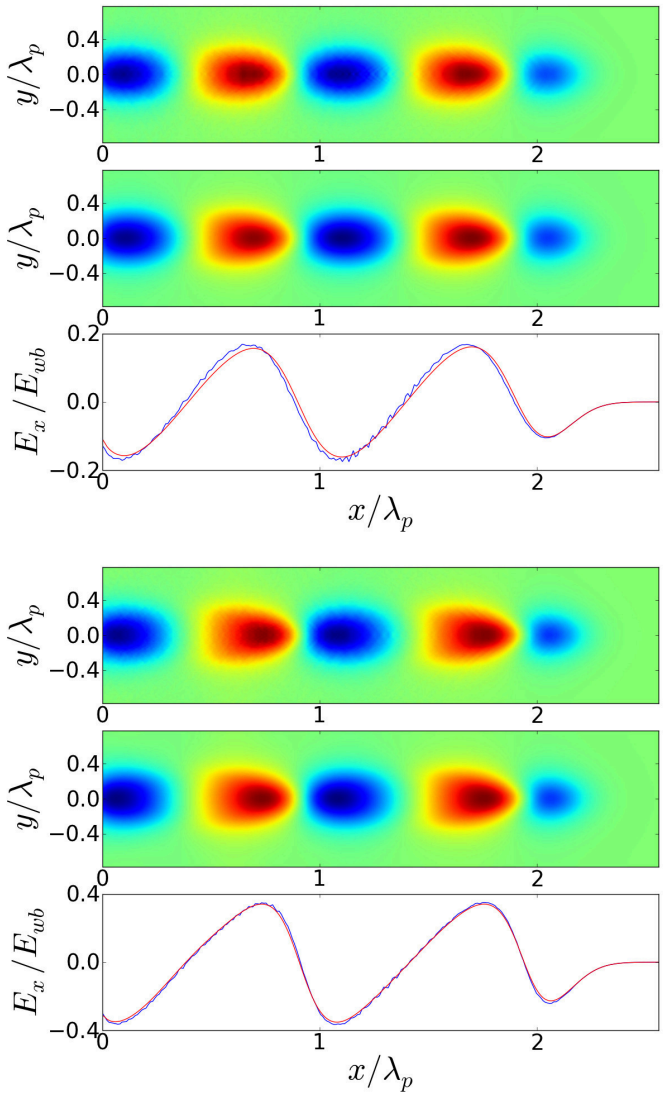

FIGURE 6.11.3. First three plots: Comparison of E_x/E_{wb}in the nonlinear regime, with a density fluctuation of ∼50%. The upper plot shows the PIC result, and the middle plot depicts the outcome from the hybrid simulation. The lower plot shows a 1D cross-section at $y = 0$, for PIC (blue) and hybrid (red) results.
Last three plots: Comparison of PIC (top) against hybrid (middle) result for the E_x-component in units of the wave-breaking field E_{wb} in the nonlinear regime with a maximum density fluctuation of 100%. The lower plot shows a one-dimensional cross-section of the same quantity at $y = 0$.

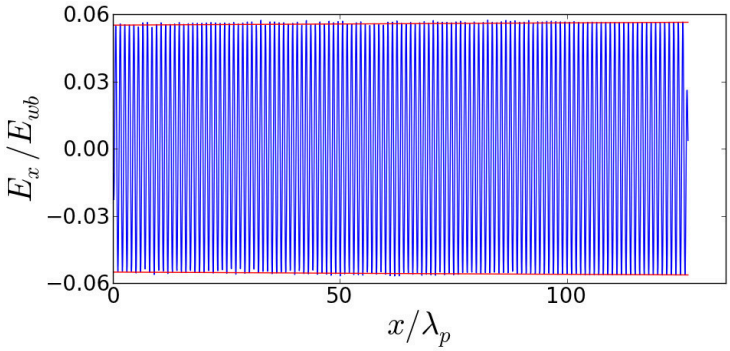

FIGURE 6.11.4. Analysis of the numerical damping of E_x of a wake field with a driver density $n_d = 0.1$. One observes that there is almost no damping present, corresponding to a $1/e$ length of $5559\lambda_p$.

CHAPTER 7

Simulation of Self-Modulated Proton Driven Plasma Wake Field Acceleration

7.1. Introduction

Plasma is a promising medium for high gradient acceleration of charged particles. It can sustain fields orders of magnitude higher than the breakdown fields of the conventional accelerators [**1**]. One can excite strong plasma waves either by lasers or by charged particle beams [**8, 9**]. One of the very attractive approaches is to use already existing TeV proton beams as a driver to generate plasma wake fields. Due to the limitation set by the transformer ratio, the energy gain of the witness beam cannot be much larger than the driver energy [**18**]. Employing a TeV proton driver allows in principle to accelerate an electron bunch to TeV energies in one single stage thus alleviating technical burden of multistaging.

It has recently been shown using detailed simulations [**3, 20**] that a high gradient plasma wake field can be generated with an ultra-short bunch of protons. In that scenario, the proton bunch was shorter than the plasma wavelength. Unfortunately, such ultra-short proton bunches are not available presently. The bunch length of the existing TeV-class proton beams are of order $L \sim 10$cm. The characteristic plasma field, the so called wave breaking field is $E_{\rm WB} = mc\omega_p/e \approx 96\sqrt{n_e({\rm cm}^{-3})}$eV, where $\omega_p = \sqrt{4\pi n_e e^2/m}$ is the plasma frequency defined by the electron density n_e. Accelerating gradients of a GeV/m-scale require plasma density of at least $n_e = 10^{14}{\rm cm}^{-3}$ corresponding to the plasma wavelength $\lambda_p \equiv 2\pi c/\omega_p \sim 3$mm. Thus, the existing proton beams correspond to $L = (10-100)\lambda_p$ and cannot efficiently generate wake fields in such plasma. The situation with the proton beams is very much the same as it was with laser pulses in the 80's of the previous century. The availability of long laser pulses necessitated the invention of a self-modulated laser wakefield accelerator (SM-LWFA)[**21**]. Subsequent progress in ultra-short pulse laser technology removed the need for self-modulation and lead to successful mono-energetic electron acceleration in the bubble regime [**11**] that reached GeV energies.

A long proton beam propagating in overdense plasma is also subject to self-modulation at the background plasma wavelength [**22**]. The effect of self-modulation opens a possibility to use existing proton beams for large amplitude wake field excitation. An experimental program is currently under consideration at CERN. The Super Proton Synchrotron at Large Hadron Collider (SPS) beam with 450 GeV protons is proposed as the driver for the initial stage of the experimental campaign. The wake field will be used for accelerating externally injected electrons. The particles must be trapped in the wake field. The trapping condition depends on the wake field amplitude and phase velocity [**4**]. Because it is expected that the SPS beam will generate a weakly-nonlinear plasma wave with the same phase velocity $v_{\rm ph}$ as the speed of the driver, it is natural to assume that the gamma-factor of the

injected electrons γ_{el} must be comparable to that of the proton driver γ_{p} for them to be trapped. As demonstrated below, that is not the case because the spatio-temporal nature of the self-focusing instability of the proton bunch considerably reduces v_{ph}.

Although it has been realized for some time[**76**] that the phase velocity of the plasma wake produced by the self-modulation instability of a laser pulse is slower than the pulse's group velocity, this was not an important issue because the laser group velocity was usually modest. For the self-modulated proton driver plasma wakefield accelerator (SM-PDPWA), the wake slowdown is of critical importance. In the next chapters, we show that the phase velocity of the unstable wave is defined not so much by the driver velocity, but mainly by the instability growth rate. The wake field is greatly slowed down at the linear instability stage when the growth rate is at its maximum. At the nonlinear saturation stage, the wake reaches the driver phase velocity. We also show a way how one can manipulate the wake phase velocity by smooth longitudinal density gradients.

Self-consistent simulations of the SM-PDPWFA effect are difficult and impose special conditions on the simulation code. Classical particle-in-cell codes suffer from numerical dispersion and field-to-particle interpolation errors. This takes the form of a wake field damping which has a strong impact on the modeling of the self-modulation.

Hence, the simulations are carried out with the new hybrid code H-VLPL3D, which was presented in chapter 6. While the proton beam can be described with the conventional PIC model, the background is represented numerically as a fluid.

The following chapters will be organized as follows. The general simulation setup is described in chapter 7.2, which will also show the self-modulation process qualitatively. In section 7.3, analytical models of the self-modulation instability are introduced.

7.2. Simulation setup

The testing phase of the envisioned experimental program at CERN will use the SPS beam. It delivers $1.15 \cdot 10^{11}$ protons at 450 GeV/c with the normalized emittance $\epsilon_n = 3.5\mu$m and the length $\sigma_z = 12$cm. We use these beam parameters in our 3D PIC simulations with the newly developed hybrid code H-VLPL3D, chapter 6. This new code simulates the background plasma hydrodynamically while the high energy beams are treated with the full kinetic algorithm. The hydrodynamic part of the code introduces much less numerical dispersion into the plasma waves than a PIC code with the same resolution. The beam has been focused down to $\sigma_r = 0.19\,$mm and sent through plasma with the free electron density $n_e = 7.76 \cdot 10^{14}\,\mathrm{cm}^{-3}$. The maximum beam density on axis is $n_b = 1.5 \cdot 10^{12}\,\mathrm{cm}^{-3}$. To avoid the beam hosing and to pre-seed the self-modulation instability, we assumed the beam being hard-cut in the middle [**22**]. The basic setup is shown in fig. 7.2.1. For the background density n_e, the plasma wave length is

$$\lambda_p = 1.2\text{mm}.$$

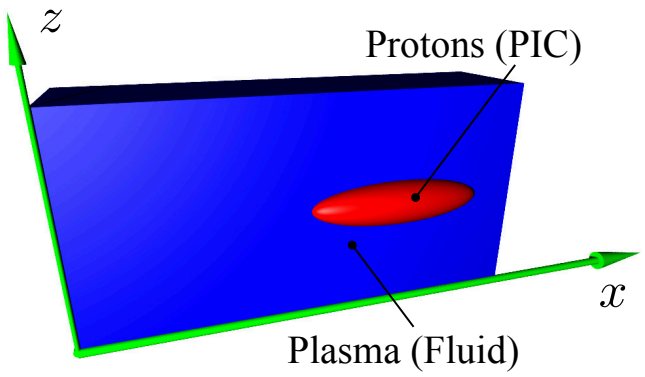

FIGURE 7.2.1. Basic setup of the SM-PDPWFA simulations. The proton bunch consists of PIC macroparticles, while the plasma is modeled with the new fluid module of H-VLPL3D.

We chose a computational domain

$$\mathcal{D} = [0, 256\lambda_p] \times [0, 1.56\lambda_p] \times [0, 1.56\lambda_p]\,,$$

the cell size

$$(\Delta x, \Delta y, \Delta z) = (0.05, 0.06, 0.06)$$

and the initial time step

$$\Delta t = 0.03.$$

A moving frame was used, shifting cell contents in the $-x$ direction with a velocity $v_{MF} = c$.

The course of events of a typical simulation can qualitatively be described as follows: The sharp border of the half-cut Gauss beam immediately excites a weak

wake field. Along a propagation distance of roughly 5 meters, the wake field slowly displaces the protons. At the same time, this introduces a modulation of the local radius $\sigma_x(x)$ of the Gauss distribution. The modulated beam again drives the wake field more resonantly, which causes the field amplitudes to rise. The structure of the densities and the E_x field component is shown in fig. 7.2.2.

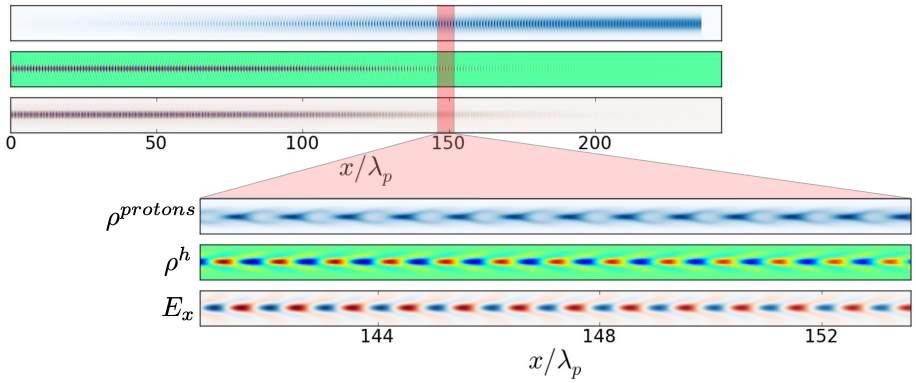

FIGURE 7.2.2. Snapshot of a typical SM-PDPWFA simulation. The upper plot shows the whole simulation domain, and the lower plot visualizes a small fraction of the total length.

In section 7.4, the important local phase velocity v_{ph} will be extracted from this data.

7.3. Self-Modulation instability

To describe the wake slowdown analytically, we adopt the formalism developed within the framework of the envelope description of the driver [**22**]. We assume an axis-symmetric beam driver and utilize the co-moving and propagation distance variables $\xi = \beta_0 ct - z$ and $\tau = z/c$, respectively, where $\beta_0 = v_z/c$ (v_z is the velocity of the bunch), and the beam's propagation direction is z. Further, the driver beam is assumed stiff enough so that its evolution time is slow $\partial_\tau \ll c\partial_\xi$. The beam occupying the $0 < \xi < L$ space is assumed to be long: $\omega_p L/c \gg 1$. The beam density profile is assumed in the form of $\rho(r,\xi) = \rho_0\,\psi(r)f(\xi)$, where $\rho_0 = n_b e$ is the charge density of the proton bunch. For simplicity, the step-like radial profile $\psi(r) = \Theta(r_b - r)$ is assumed, where $r_b(\xi,\tau)$ is the evolving radius of the beam's envelope, and $\Theta(r_b - r)$ is the Heaviside step-function. The betatron frequency of the self-focused beam is defined as $\omega_{\beta 0} \equiv ck_{\beta 0} = \sqrt{4\pi n_b e^2/2\gamma_b m_p}$, where m_p is the proton mass. In the limit of thin beam ($k_p r_b \ll 1$) and linear plasma response, the equation of motion for the beam's radius (in normalized coordinates $\tilde{r}_b = r_b/r_{b0}$, $\tilde{\tau} = \omega_{\beta 0}\tau$, $\tilde{\xi} = k_p\xi$) is given by [**22**]

$$\frac{\partial^2 \tilde{r}_b(\tilde{\xi})}{\partial \tilde{\tau}^2} - \frac{\tilde{\epsilon}_n^2}{\tilde{r}_b^3(\tilde{\xi})} = -\int_0^{\tilde{\xi}} \frac{I(\tilde{\xi}')}{\tilde{r}_b(\tilde{\xi}')} \sin(\tilde{\xi} - \tilde{\xi}')d\tilde{\xi}', \tag{7.3.1}$$

where σ_θ, r_{b0} and $I(\xi) = f(\xi)\tilde{r}_b^2(\tilde{\xi},\tilde{\tau})$ are the beam angular divergence, initial radius, and longitudinal current profile, respectively, and $\tilde{\epsilon}_n = \sigma_\theta/(k_{\beta 0} r_{b0})$. Perturbing Eq.(7.3.1) about the initial radius $\tilde{r}_b = 1+\delta r_b$, yields the linearized equation [**22**]:

$$\left(\frac{\partial^2}{\partial\tilde{\xi}^2}+1\right)\left(\frac{\partial^2\delta\hat{r}_b}{\partial\tilde{\tau}^2}+3\tilde{\epsilon}_n^2\delta\hat{r}_b\right)=\delta\hat{r}_b. \tag{7.3.2}$$

Following the approach of Bers [**77**], we find an asymptotic solution of this equation for sufficiently late times, $\tilde{\tau} > L_e$, where $L_e \sim 1/\Gamma$ is the e-folding length, and Γ is the growth rate of the instability. Substitution of $\delta r_b = \delta\hat{r}_b \exp(-i\delta\omega\tilde{\tau} + ik\tilde{\xi})$ into Eq. (7.3.2) yields the dispersion equation $\delta\omega(k)$. The peak growth rate is calculated [**77**] by introducing $\delta\omega^{'} = \delta\omega - \upsilon k$, where $\upsilon = \tilde{\xi}/\tilde{\tau}$, and requiring that $D(\delta\omega^{'},k) = 0$ and $\partial D(\delta\omega^{'},k)/\partial k = 0$:

$$(1-k^2)(-\delta\omega^2+3\tilde{\epsilon}_n^2) = 1, \tag{7.3.3}$$

$$-k(-\delta\omega^2+3\tilde{\epsilon}_n^2)-\delta\omega\upsilon(1-k^2) = 0. \tag{7.3.4}$$

Equations (7.3.3) and (7.3.4) lead to the standard dispersion relation typical of the beam-breakup instability which is known [**78**] to always possess a growing mode with $\Im(\delta\omega) > 0$. To simplify the algebra, we assume that $3\tilde{\epsilon}_n^2 = \mathcal{O}(1)$ and consider the initial stage of instability corresponding to $k = 1+\delta k$, where $\delta k \ll 1$. In this limit $\delta\omega \gg \tilde{\epsilon}_n$, and Eqs. (7.3.3),(7.3.4) are reduced to the dispersion relation $\delta\omega^3 = -\upsilon$, and $4\delta\omega\upsilon\delta k^2 = -1$. The complex roots are given by

$$\delta\omega_\pm = \frac{1\pm i\sqrt{3}}{2}\left(\frac{\tilde{\xi}}{\tilde{\tau}}\right)^{1/3},\ \delta k = -\frac{1\pm i\sqrt{3}}{4}\left(\frac{\tilde{\tau}^2}{\tilde{\xi}^2}\right)^{1/3}. \tag{7.3.5}$$

In physical units, the condition for $\delta\omega \gg \tilde{\epsilon}_n$ can be expressed as

$$t \ll t_{\rm short} \equiv \gamma_b^2\frac{\xi}{c}\frac{n_b m}{n_e M}\left(\frac{k_p r_{b0}^2}{\varepsilon_n}\right)^3, \tag{7.3.6}$$

where $\varepsilon_n = \gamma_b\sigma_\theta r_b$ is the normalized beam emittance. The number of e-foldings is given by $N_e = \Im(\delta\omega)\tilde{\tau} - \Im(\delta k)\tilde{\xi} = 3\Im(\delta\omega)\tilde{\tau}/2$, and therefore the growth rate $\Gamma = 3\Im(\delta\omega)/2 = 3\sqrt{3}\left(\tilde{\xi}I(\tilde{\xi})/\tilde{\tau}\right)^{1/3}/4$. In dimensional variables, the instability growth rate is expressed as

$$\Gamma = \frac{3\sqrt{3}}{4}\omega_p\left(\frac{n_b m}{2n_e m_p\gamma_b}\frac{\xi}{ct}\right)^{1/3}, \tag{7.3.7}$$

and the maximum number of e-foldings achieved at $t = t_{\rm short}$ is

$$N_e \approx (3\sqrt{3}/4)\tilde{\xi}^{1/3}\tilde{\tau}^{2/3} = (3\sqrt{3}/4)k_p L\tilde{\epsilon}_n^{-2/3}.$$

Note that for the typical parameters of the SPS beam and plasma density $n_e = 10^{14}\ldots10^{15}{\rm cm}^{-3}$, $N_e \approx 100$. Therefore, it is most likely that the self-modulation instability will enter the nonlinear regime prior to $t = t_{\rm short}$, and the above assumptions will remain valid throughout the linear stage of the instability.

The crucial observation is that $\delta\omega$ and δk have not only imaginary parts responsible for instability growth, but also real parts. It is this real part that changes the wake phase velocity. The wake phase is $\psi_e = (1+\Re(\delta k))\tilde{\xi} - \Re(\delta\omega)\tilde{\tau}$, and the phase velocity $\upsilon_{\rm ph} = \upsilon_b + (\partial\psi/\partial\tilde{\tau})/(\partial\psi/\partial\tilde{\xi})\omega_{\beta 0}/\omega_p$. Substituting (7.3.5) for $\delta\omega$ and

δk and neglecting small terms on the order of $\upsilon^{-2/3}$, we obtain the phase velocity of the growing mode

$$\upsilon_{\rm ph} = \upsilon_b \left[1 - \frac{1}{2} \left(\frac{\xi}{ct} \right)^{1/3} \left(\frac{I(\xi) n_b m}{2 n_e m_p \gamma_b} \right)^{1/3} \right]. \tag{7.3.8}$$

The wake phase velocity (7.3.8) can be significantly lower than the speed of the beam due to the instability dispersion. The relativistic $\gamma-$factor of the wake phase velocity $\gamma_{ph} = \left(1 - \upsilon_{ph}^2/c^2\right)^{-1/2}$ can be an order of magnitude lower than that of the driving beam. This effect will prohibit electron acceleration to high energies at the instability stage. Yet, one can easily see from the formulas that the phase velocity decrease is closely connected with the instability growth rate. Thus, one may expect that when the instability saturates, the phase velocity of the wake becomes close to that of the beam. This effect might help to inject low energy electrons into the wake of a highly relativistic proton beam at a later stage of the instability, just before the nonlinear saturation.

7.4. Simulation results

The main subject of this investigation is the wake field's phase velocity v_{ph}, which is important for a later injection of particles. Also, we aim for a way of controlling v_{ph} via plasma density gradients. Hence, one needs a proper definition of such a phase velocity first. A natural approach is to define it through the motion of the accelerating phases of the field component E_x.

In practice, we have obtained a good approximation by tracking the zeros of E_x from on-axis data extracts. This is done by linearly interpolating E_x and retrieving the positions of the zeros at a time n. These positions are then matched to the former ones at time $n-1$. From this procedure we have obtained one-dimensional trajectories

$$(x_\alpha^n)_{\alpha,n=1,1}^{N_Z,N_T} \tag{7.4.1}$$

of the E_x field zeros. Here, α is the index of the zero and, N_Z is the total number of zeros tracked and N_T is the number of recorded snapshots. The phase velocity was obtained by computing the numerical derivative of (7.4.1).

The results are presented in Fig. 7.4.1. From the frame (a) we see that the linear instability stage lasts during the first 5 meters of propagation. Then, the beam is completely modulated and the nonlinear saturation is reached. The wake phase velocity is shown in the frame (b). A significant slowdown of the wake is observed during the instability. The lowest phase velocity is registered to be $\upsilon_{\rm ph} \approx (1 - 3.5 \cdot 10^{-4})\, c$. This corresponds to the wake $\gamma-$factor $\gamma_{ph} \approx 38$. This is an order of magnitude lower than the $\gamma-$factor of the driving beam. The frame (c) compares the simulation result (the solid red curve) with the analytic expression (7.3.8), where we substituted the SPS beam parameters. This snapshot of the wake phase velocity has been taken at $Z = 2.5\,\mathrm{m}$, in the middle of the linear instability stage. A reasonable agreement between the simulation and the analytical theory is seen.

The wake slowdown has a dramatic impact on the electron trapping and acceleration. First, it allows to trap low energy electrons whose velocities are comparable with the wake velocity. However, the energy gain in the slow wake is very

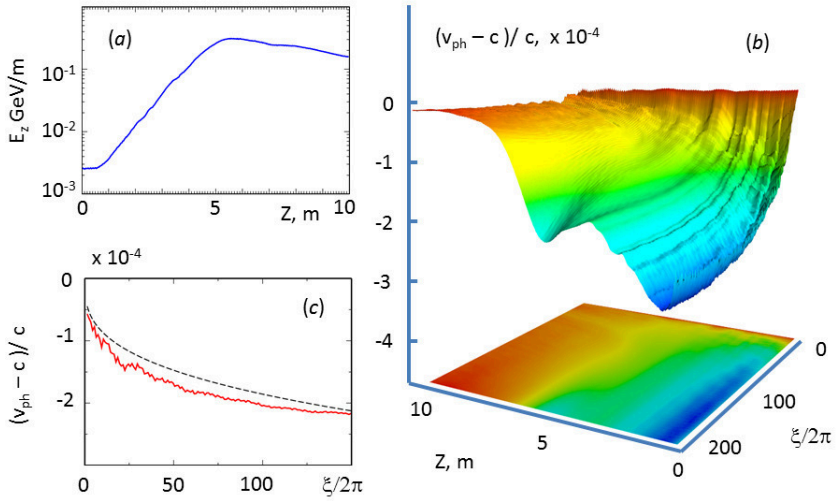

FIGURE 7.4.1. (color online) 3D hybrid PIC simulation of SPS beam self-modulation in plasma with constant density $n_e = 7.76 \cdot 10^{14}$ cm^{-3}. Frame (a) shows evolution of the maximum accelerating field. The linear instability persists for some 5 meters before the nonlinear saturation. Frame (b) shows the phase velocity of the wake as a surface in dependence on the propagation distance Z and the beam coordinate ξ. The phase velocity experiences a deep drop towards the tail of the beam at the linear stage of the instability. When the beam is completely modulated and the instability saturates at $Z > 5$m, the wake phase velocity surges up to that of the driving beam. Frame (c) gives a snapshot of the wake phase velocity after 2.5 meters of propagation distance (the solid red line). The broken line gives the analytical expression (7.3.8).

limited due to the fast dephasing. The energy gain is given by the formula [**4**] $\Delta W \approx 4\gamma_{ph}^2 mc^2 (E_{max}/E_{WB})$. At the linear stage we have $E_{max} \ll E_{WB}$ and the energy gain is low for small γ_{ph}. The dephasing, however, has a much worse effect. If the electrons have been injected into the early instability phase of the slow wake, they can be lost when they overtake the wave and enter the defocusing phase. The dephasing distance is $k_p L_d \approx 2\pi\gamma_{ph}^2$ and for the slow wake field it can be shorter than the instability time. For this reason, the electrons must be injected at the late time of the instability, when the phase velocity begins to grow. In our simulation, the saddle point for injection is located around $z = 5\,$m. The wake phase velocity is still low here, but starts to grow rapidly as the beam reaches complete modulation.

7.5. Electron side injection

A possibility to inject electrons into the wake is the side injection [**79**]. In this case, a beam of electrons is propagating at a small angle with respect to the driver. The advantage of the side injection over the on-axis injection is that electrons are gradually "sucked-in" by the wake transverse field at the right phase. This leads to a high quality quasi-monoenergetic acceleration of electrons.

The energy of the accelerated electrons is quite sensitive to their initial conditions. However, because of the negligible charge of an electron "witness" beam, one can perform greatly simplified test particle simulations here. The idea is to run two-staged computations:

First, a large scale self-consistent simulation of the plasma wake field of a self-modulating proton bunch in done. The parameters are the same as for the investigation depicted above. From this simulation, two-dimensional snapshots of the electromagnetic fields were saved with a high resolution in time.

Then, the VLPL code was run with its recently implemented test particle mode. The stored data from the first simulation were read by the second simulation, and re-interpreted as cylindrically symmetric fields. VLPL's particle module was adapted for this purpose, skipping the current deposition step. Since the need for grid operations and current calculation was removed, such a job could be executed on one single processor core. Thus, a great number of witness beam simulations was run simultaneously in order to scan through the injection angles and injection points. For an injection angle $\theta_{in}$and relativistic factor γ_{in}, the initial momentum of the witness bunch must be set to

$$\mathbf{p}_{in} = m_e c \sqrt{\gamma_{in}^2 - 1} \begin{bmatrix} \cos\theta_{in} \\ \sin\theta_{in} \\ 0 \end{bmatrix}.$$

We denote by x_{hit} the distance the proton bunch has propagated in the plasma until it meets the electron witness bunch; $x_{shift} > 0$ is the distance between the proton beam's head and the theoretical point where the electron bunch meets the protons. Additionally, we need the position of the head of the proton bunch, x_{head}. The initial electron velocity is

$$\mathbf{v}_{in} = c \sqrt{1 - \frac{1}{\gamma_{in}^2}} \begin{bmatrix} \cos\theta_{in} \\ \sin\theta_{in} \\ 0 \end{bmatrix},$$

and the time of collision between the two bunches is approximately

$$t_{hit} \approx \frac{x_{hit}}{c}.$$

Then the initial position of the electrons must be set to

$$\mathbf{r}_0^e = \begin{bmatrix} x_{head} - x_{shift} + (c - v_{in,x})\, t_{hit} \\ -t_{hit} v_{in,y} \\ 0 \end{bmatrix}.$$

In general, this position lies outside of the simulation box. A straightforward seeding of particles at the domain border in each time step leads to unphysical density fluctuations. Therefore, it was necessary to implement a generalized particle injection system. This module keeps track of the motion of virtual PIC macroparticles in order to put them into the border of the simulation domain just at the right moment; it also works in the moving frame mode.

We show two of these simulations, where we have injected two beams of test electrons. The first beam of 20 MeV electrons was injected on-axis together with the driving beam. This electron energy roughly corresponded to the minimum wake phase velocity at the tail of the driver. We found that during the linear growing

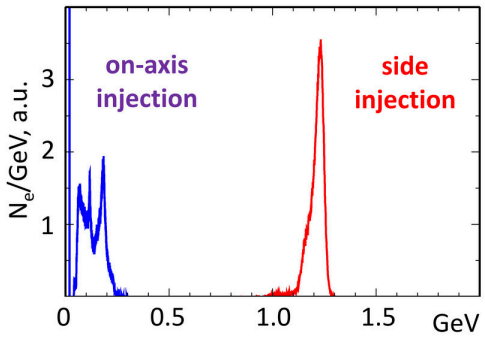

FIGURE 7.5.1. (color online) Electron energy spectra at $z = 10\,\mathrm{m}$. There were two groups of electrons. The one was injected on-axis together with the driving beam. The another was side-injected at the angle of 0.005 radian, the electron beam trajectory should cross the driver axis at $z = 6\,\mathrm{m}$, $\xi = 20\,\mathrm{cm}$ behind the beam head. The on-axis injection lead to a broad spectrum and low energy gain. The side injection resulted in a quasi-monoenergetic beam at 1.2 GeV energy and about 1% energy spread. Initial electron energy was 20 MeV for on-axis injection and 10 MeV for side injection.

instability stage, these electrons did more that one oscillation in the wake ponderomotive bucket. Finally, after 10 meters of propagation, the maximum energy gain was about 200 MeV with a rather broad energy spectrum, as seen in Fig. 7.5.1.

The second electron beam with 10 MeV energy has been side-injected at the angle of 0.005 radian. The electron beam trajectory was designed to cross the driver axis at $z = 6\,\mathrm{m}$, $\xi = 20\,\mathrm{cm}$ behind the beam head. Due to the small injection angle, however, the electrons have been sucked in into the wake much earlier, at the position $z \approx 5\mathrm{m}$. The wake transverse fields have put most of the beam electrons into the focusing and accelerating phase. The electron beam and field configuration just after the electrons entered the wake is shown in Fig. 7.5.2. The electron beam is split into micro-bunches located exactly in the accelerating and focusing phases of the wake. Due to this configuration, the side injected beam resulted in the maximum energy gain of 1.2 GeV and a rather narrow energy spectrum.

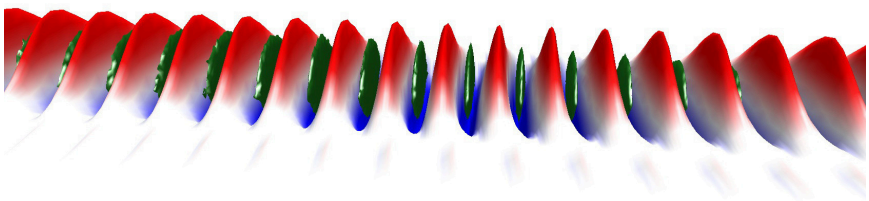

FIGURE 7.5.2. (color online) Test electron beam (dark green discs) and the accelerating field (the red-blue wave) just after the side injection at $z = 5\,\mathrm{m}$. The electron beam is split into micro bunches located exactly in the accelerating and focusing phases of the wake.

The low energy spread and efficient acceleration of the side injected electrons are also due to fast rise in the wake phase velocity just after the injection position, as seen in Fig. 7.4.1(b). The electrons gain energy while staying in the accelerating phase of the wake.

7.6. Phase velocity control

We have seen above that the growing mode (7.3.5) has the low phase velocity (7.3.8). There is a way, however, to manage the phase velocity of the wake by employing a gentle longitudinal plasma density gradient as it has been discussed in [**80**]. To elucidate the effect, we have performed an additional simulation with the same beam parameters, but introducing a positive plasma density gradient:

$$n_e(z) = n_{e0}(1 + z/d),$$

with the characteristic length $d = 200$m. The phase velocity obtained in this simulation is shown in Fig. 7.6.1.

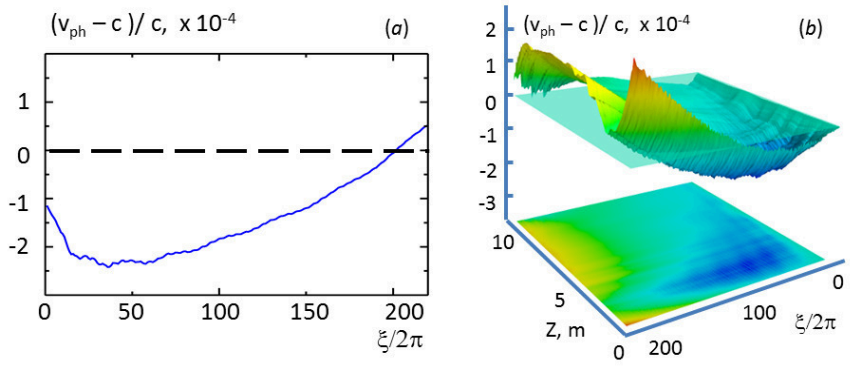

FIGURE 7.6.1. (color online) Phase velocity control by positive plasma density gradient. a) Phase velocity at z=2.5 m. b) Full dynamics picture; the transparent plane marks the speed of light.

The phase velocity at the head of the beam takes a dive as defined by the growing mode dispersion. However, the positive plasma density gradient compensates for the mode dispersion and at the tail of the beam the wake phase velocity becomes equal to the speed of light and even superluminous.

In summary, we have shown that the self-modulational instability of a charged beam in plasma corresponds to a growing mode with a slow phase velocity. The wake velocity is much lower than that of the driver. The wake slowdown is due to the real part of the frequency of the unstable mode. Although this effect limits electron energy gain at the stage of the linear instability growth, the low phase velcoity can be harnessed to inject low energy electrons into the wake of a highly relativistic driver. We also have shown that the side injection of electrons at a small angle with respect to the driver axis may drastically improve the quality of acceleration. The transverse field of the wake sucks in the injected electrons and automatically puts them into the right acceleration phase. Finally, we show that the wake phase velocity can be controlled by a longitudinal plasma density gradient.

7.7. Coherent Transition Radiation for Self-Modulation Measurement

As mentioned above, there is a collaboration for a plasma wake field acceleration experiment based on the SM-PDPWFA effect. It aims at building up an experimental setup at CERN, which utilizes 450 GeV proton bunches from the SPS accelerator. There is a number of open questions concerning the plasma generation, the geometry of the devices and the methods of measurement. One interesting problem is how to detect the state of the driving bunch after it has passed the plasma channel. The self-modulation effect causes the driver to be constricted - however the total current through a plane perpendicular to the propagation direction is not altered. Additionally, the bunch may suffer from the hosing instability, which shifts the bunch periodically in transversal direction. This results in a snake-like shape, being an undesirable outcome. Here, one needs a diagnosis tool for the longitudinal structure of the bunch.

One of the most common techniques for this problem is the Coherent Transition Radiation method[**81, 82, 83, 84, 85**]. It has proven particularly useful in the structural investigation of laser-plasma accelerated electron bunches [**86, 87, 88**]. When a charged particle propagates through a dielectric medium for some time, its surrounding field reaches a steady-state solution. A sharp boundary in the background permittivity causes a different surrounding field; the unmatched field is radiated.

Let us consider a transition radiation emitted by a particle bunch as it traverses normally a conductor plate. The interaction geometry is illustrated in Fig. 7.7.1. When an elementary charge dq exits from the conducting plate in the normal direction with the velocity $\mathbf{v}$, the radiated field is given by the formula (63.8) from the Landau textbook [**89**]:

$$\begin{aligned} d\mathbf{E} &= \frac{dq}{c^2\left(R-\frac{\mathbf{Rv}}{c}\right)^3}\mathbf{R}\times\left[\left(\mathbf{R}-\frac{\mathbf{v}}{c}R\right)\times\frac{d\mathbf{v}}{dt'}\right] \\ &+ \frac{dq}{c^2\left(R+\frac{\mathbf{Rv}}{c}\right)^3}\mathbf{R}\times\left[\left(\mathbf{R}+\frac{\mathbf{v}}{c}R\right)\times\frac{d\mathbf{v}}{dt'}\right] \end{aligned} \tag{7.7.1}$$

where t' is the retarded time so that

$$t' + R(t')/c = t. \tag{7.7.2}$$

The second term in Eq. (7.7.1) is generated by the image of the physical charge in the conducting plate.

For a simple derivation of the radiated fields, we assume the field inside the plate as well as the current, to be zero. Thus, when a charge fraction exits the surface, its current has a jump discontinuity $\mathbf{v}(t') = \mathbf{v}_0\Theta(t'-t_\mathrm{e})$, where t_e is the time the charge exits into vacuum and $\Theta(t)$ is the Heaviside step function. The denominators in (7.7.1) indicate that the strongest radiation can be expected in the angle $\theta \approx 1/\gamma$. However, the radiation on the transverse plane yields more coherent information about the bunch structure, so we will focus on the latter. By setting $\mathbf{v} \perp \mathbf{R}$, we get

$$\begin{aligned} d\mathbf{E} &= -\frac{2}{c^2R}\frac{d\mathbf{v}}{dt'}dq \\ &= -\frac{2}{c^2R}\mathbf{v}_0\delta\left(t'-t_e\right)dq. \end{aligned}$$

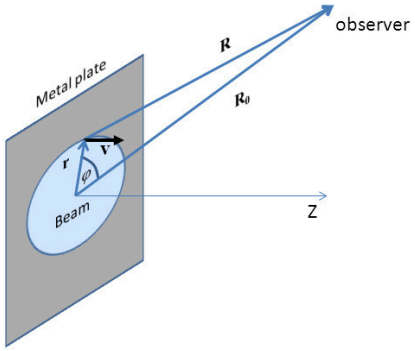

FIGURE 7.7.1. Geometry of the transverse coherent transition radiation. A charged particle bunch exits a conductor plate normally to the surface. The observer looks at the emitted radiation from side to the beam, in the plane of the surface.

For a continuous bunch, the differential form for the charge contribution is

$$dq = en\,(t, \mathbf{r})\, v_0 dS dt = en\,(t, \mathbf{r})\, v_0 r\, dr\, d\varphi\, dt,$$

where $n\,(t, \mathbf{r})$ is the charge density. The field is polarized in the bunch propagation direction and normal to the metal plate surface. The observed radiated field is thus

$$E(t, R_0) = \int dE = -\frac{2ev_0^2}{c^2 R_0} \iint n(t', \mathbf{r}) dS. \tag{7.7.3}$$

Here, we have used the assumption that the observer is far away from the radiation source, thus $R \approx R_0$. The geometry is conveniently expressed in cylindrical coordinates. It will turn out that the modulation of the field is caused by the modulation of its propagation distance. This information is contained in the retarded time

$$t' = t - \frac{R(t')}{c} \approx t - \frac{R_0}{c} + \frac{r}{c}\cos\varphi. \tag{7.7.4}$$

Eq. (7.7.3) can now be applied on different bunch profiles. A transversally constricted or hosed particle bunch may have the same total transverse current

$$I_T = ev_0 \iint n(t', \mathbf{r}) dS$$

as an unaltered bunch. Still, we will see that these effects have clearly different radiation signatures.

7.7.1. TCTR emitted by modulated axially symmetric bunches with constant current. Let there be a Gauss-shaped bunch with a longitudinal radius modulation

$$n(t', \mathbf{r}, z) = n_0 \frac{\sigma_0^2}{\sigma^2(t', z)} e^{-r^2/2\sigma^2(t', z)}, \tag{7.7.5}$$

$$\begin{aligned}\sigma(t', z) &= \sigma_0 \left[1 + \epsilon f\left(k(z - v_0 t')\right)\right] \\ &= \sigma_0 \left[1 + \epsilon f\left(kz - kv_0 t + kR_0 \frac{v_0}{c} - kr\frac{v_0}{c}\cos\varphi\right)\right].\end{aligned}$$

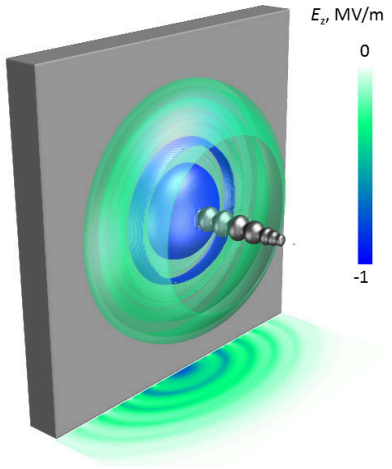

FIGURE 7.7.2. TCTR emitted by a proton bunch exiting from a metallic foil. Only the radius of the proton bunch is modulated, not the current. The colored surfaces show the electric field component normal to the metal foil.

The position of the metal plate surface can be set to $z = -R_0 v_0/c$. To get an analytic expression for the electric field, we shall use some approximations for the density. First, we Taylor-expand with respect to kr:

$$\begin{aligned} f\left(-kv_0 t - kr\frac{v_0}{c}\cos\varphi\right) &= f\left(-kv_0 t\right) - \left(kr\right)\frac{v_0}{c}\cos\left(\varphi\right) f'\left(-kv_0 t\right) \\ &+ \frac{1}{2}\left(kr\right)^2\frac{v_0^2}{c^2}\cos^2\left(\varphi\right) f''\left(-kv_0 t\right) + \mathcal{O}\left(\left(kr\right)^3\right). \end{aligned}$$

Second, we expand the density with respect the relative perturbation amplitudeϵ:

$$\frac{\sigma_0^2}{\sigma^2(t',z)} e^{-r^2/2\sigma^2(t',z)} = e^{-r^2/2\sigma_0(t',z)}\left[1 + \epsilon f\left(...\right)\left(\frac{r^2}{\sigma_0^2} - 2\right)\right] + \mathcal{O}\left(\epsilon^2\right).$$

We obtain

$$n(t,\mathbf{r},z) \approx n_0\left[1 + \epsilon A\left(\frac{r^2}{\sigma_0^2} - 2\right)\right] e^{-r^2/2\sigma_0^2}, \tag{7.7.6}$$

where

$$A := f\left(-kv_0 t\right) - \left(kr\right)\frac{v_0}{c}\cos\left(\varphi\right) f'\left(-kv_0 t\right) + \frac{1}{2}\left(kr\right)^2\frac{v_0^2}{c^2}\cos^2\left(\varphi\right) f''\left(-kv_0 t\right).$$

The second and the third terms in (7.7.6) originate from the time retardation (7.7.2) and are essential for the radiation emission.

The field excited by the axisymmetric particle bunch is then

$$\begin{aligned} E(t,R_0) &= -n_0\frac{2ev_0^2}{c^2 R_0}\int_0^{2\pi} d\varphi \int_0^{\infty} r \times \\ &\left[1 + \epsilon A\left(\frac{r^2}{\sigma_0^2} - 2\right)\right] e^{-r^2/2\sigma_0^2} dr \end{aligned} \tag{7.7.7}$$

The integrand in (7.7.7) contains terms with different powers of kr. The terms independent on kr are not retarded. The oscillatory part of the integral of these

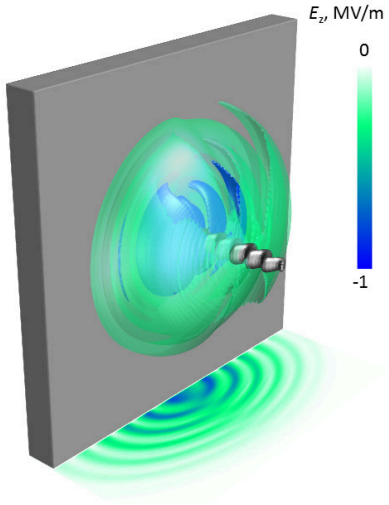

FIGURE 7.7.3. TCTR emitted by a hosed proton bunch exiting from a metallic foil. The radiated field is shaken off anti-symmetrically in the plane of hosing.

terms vanishes because we assumed the total current of the particle bunch being constant. The terms linear in kr contain the factor $\cos\varphi$ and disappear when we integrate in the angle φ over the bunch cross-section. This is due to the axial symmetry of current distribution in the bunch. The first oscillatory terms that do not vanish after the integration are quadratic in kr. Collecting the terms proportional to $(kr)^2$ at the first time harmonic, we get

$$E^{osc}(t,R_0) = \epsilon n_0 f''(kv_0 t)\frac{2ev_0^4}{R_0c^4}\int_0^{2\pi}\cos^2\varphi d\varphi \times$$

$$\times \int_0^{\infty} r(kr)^2\left(1-\frac{r^2}{2\sigma_0^2}\right)e^{-\frac{r^2}{2\sigma_0^2}}dr. \tag{7.7.8}$$

for the first order oscillatory components of the field. We compute this integral and obtain

$$E(t,R_0) = -2\epsilon\frac{J}{cR_0}(k\sigma_0)^2\beta_0^3 f''(-kv_0 t). \tag{7.7.9}$$

where $J = 2\pi\sigma_0^2 en_0 v_0$ is the total bunch current and$\beta_0 = v_0/c$. We can insert the case of a simple cosine modulation, $f(x) := \cos(x)$, getting

$$E(t,R_0) = 2\epsilon\frac{J}{cR_0}(k\sigma_0)^2\beta_0^3\cos\omega_{rad}t. \tag{7.7.10}$$

The radiation frequency is $\omega_{rad} = kv_0$. This expression is valid only for narrow bunches, where $k\sigma_0 \ll 1$. The case present in our previous investigations in chapter (7.4) (with $k\sigma_0 \approx 1$) is difficult to treat analytically.

Still, a simulation clearly showed the presence of the TCTR in this regime.

7.7.2. TCTR emitted by hosed bunches with constant current. The second case we will describe here is that of a hosed proton bunch: The radius remains unaltered, but the transversal center position varies with z. The density is given by

$$n(t', \mathbf{r}, z) = n_0 e^{-\left(\mathbf{r}-\mathbf{r}_c(t',z)\right)^2/2\sigma^2}. \tag{7.7.11}$$

The center position is

$$\begin{aligned} \mathbf{r}_c(t', z) &= \mathbf{r}_{c0} h\left(k(z - v_0 t')\right) \\ &= \mathbf{r}_{c0} h\left(kz - kv_0 t + kR_0 v_0/c - kr(v_0/c)\cos\varphi\right). \end{aligned} \tag{7.7.12}$$

Again, the surface position is assumed to be $z = -R_0 v_0/c$. We use a taylor expansion similar to the one in section 7.7.1. Expanding $h\left(-kv_0 t - kr\frac{v_0}{c}\cos\varphi\right)$ linearly in (kr) and $n\left(t', \mathbf{r}, z\right)$ linearly in r_{c0}, we get

$$n(t, \mathbf{r}, z) \approx n_0 \left(1 + \frac{\mathbf{r}_{c0}\mathbf{r}}{\sigma^2} A_h\right) e^{-r^2/2\sigma_0^2}, \tag{7.7.13}$$

where

$$A_h = h\left(-kv_0 t\right) - kr\frac{v_0}{c} h'\left(-kv_0\right) t\cos\varphi \tag{7.7.14}$$

and

$$\mathbf{r}_{c0}\mathbf{r} = r_{c0} r\cos(\varphi - \varphi_0). \tag{7.7.15}$$

φ_0 is the angle between the plane of hosing and the direction to the observer. The field excited by the axisymmetric particle bunch is then

$$\begin{aligned} E(t, R_0) &= -n_0 \frac{2ev_0^2}{c^2 R_0} \int_0^{2\pi} d\varphi \int_0^{\infty} r\times \\ &\times \left(1 + \frac{r_{c0} r\cos(\varphi - \varphi_0)}{\sigma^2} A_h\right) e^{-\frac{r^2}{2\sigma_0^2}} dr. \end{aligned} \tag{7.7.16}$$

Again, we are only interested in the oscillating part of the field, which is

$$\begin{aligned} E(t, R_0) &= 2\pi\cos\varphi_0 h'\left(kv_0 t\right) \frac{en_0 v_0^3}{R_0 c^3} \sigma^2 kr_0 \\ &= \frac{J}{cR_0} \beta_0^2 kr_0 \cos\varphi_0 h'\left(kv_0 t\right). \end{aligned} \tag{7.7.17}$$

The radiation amplitude is proportional to the hosing amplitude kr_0 and the first derivative of the hosing function $h'\left(\omega_{rad} t\right)$. In the case of a periodic harmonic hosing of the particle bunch radius, $h(kv_0 t) = \cos(kv_0 t)$, the expression (7.7.17) becomes

$$E(t, R_0) = \frac{J}{cR_0} \beta_0^2 kr_0 \cos\varphi_0 \sin\left(kv_0 t\right) \tag{7.7.18}$$

From (7.7.17)-(7.7.18) we see that the hosed bunch radiation is not axially symmetric. The main lobes are located in the hosing plane as described by the factor $\cos\varphi_0$ and are antisymmetric to each other.

7.7.3. Numerical examples. We performed two test numerical simulations to illustrate the effect of TCTR. The simulations have been done with the hybrid code H-VLPL3D [**73, 32**](chap. 5). It can handle plasmas of arbitrary high densities as fluids. In these test simulations, we take a model proton bunch that carries the current of an optimized Super-Proton-Synchrotron (SPS) bunch, $I_0 = 50\text{A}$ and the protons have the longitudinal momentum $p = 450\text{GeV/c}$. The self-modulation wavelength is $\lambda = 1.2\text{mm}$. The length of the model bunch was chosen short, $\sigma_z = 2\lambda = 2.4\text{mm}$, for illustration purposes. The final result does not depend on the bunch length. It was done with the domain

$$\mathcal{D} = [0, 20\lambda] \times [0, 15\lambda] \times [0, 15\lambda]$$

and the grid steps

$$\Delta x = \Delta y = \Delta z = 0.05\lambda,$$

We define the critical density associated with λ, $n_c = \pi c^2 m_e / e^2 \lambda^2$. A short, self-modulated gaussian proton bunch given by 7.7.5 passes through a dense electron plasma with $n_e = 100 n_c = 7 \cdot 10^{16}$. The parameters of the bunch are $n_0 = 0.01$, $n_c = 7{\cdot}10^{12}\text{cm}^{-3}$, $\sigma = 0.17\lambda\,(1 + 0.5\cos(k_p z))$. Here, $k_p$is the plasma wave number. The latter represents the metal foil. The result is shown in fig. 7.7.2. The 2D color plot on the bottom plane as well as the blue and cyan iso surfaces show the E_x field component. The radiation is emitted axisymmetrically in the transverse direction. The radiation field magnitude reaches several 100kV/m values at 1mm distance from the bunch axis.

In the second simulation we used a hosed proton bunch with the model density profile

$$n(t, \mathbf{r}, z) = n_0 e^{-(x - x_0(t,z))^2 / 2\sigma_0^2} e^{-z^2/2\sigma_z^2}. \tag{7.7.19}$$

with $n_0 = 1.4 \cdot 10^{12}\text{cm}^{-3}$,$\sigma_0 = 0.2\text{mm}$ and the time dependent centroid $x_0 = r_0 \cos k_p z$, where the hosing amplitude was $r_0 = 0.2\text{mm}$. The result is shown in fig. 7.7.3. The field is modulated only in the direction of the centroid shift.

7.8. Summary

In this chapter, several investigations on the SM-PDPWFA regime of plasma wake field acceleration have been presented. For the simulations, the novel PIC/fluid hybrid code H-VLPL3D (sec. 6) was used, which performed very well in modeling this difficult setup. By extracting the phase velocity of the wake, it could be shown that the latter, although starting with relatively low values, rises during the non-linear stage of the self-modulation instability. This could be beneficial for electron side injection. Furthermore, the possibility of altering the phase velocity through slight background density gradients was demonstrated. Also, the possible scenario of side injection was investigated via multi-staged simulations; for the right parameters, a great fraction of electrons was 'sucked' into the wake, and accelerated efficiently. These findings further indicate that SM-PDPWFA is a promising candidate for a large-scale plasma-based particle acceleration mechanism, and have been published in [**19**].

CHAPTER 8

Summary

The main focus of this thesis is the development, implementation and application of hybrid modules for the particle-in-cell (PIC) plasma simulation code Virtual Laser Plasma Lab (VLPL). Within this PIC/fluid hybrid concept, a plasma can be modeled either with the PIC method, or via methods of grid-based computational fluid dynamics(CFD).

Based on a linearized fluid model, a Mollified Impulse exponential integrator was developed and implemented in collaboration with the Institute for Applied Mathematics, HHU Düsseldorf. It uses a three-component push-oscillate-splitting scheme, as well as filter functions to avoid unphysical resonances. The stability of this integrator does not depend on the plasma frequency, hence plasmas of arbitrary densities can be simulated. After the implementation, it has been successfully tested using several physical examples.

Another, non-linear, hybrid scheme was designed specially for the simulation of extremely long wake fields. This module uses primitive fluid variables on a staggered grid to avoid interpolations. It was implemented into the VLPL code, forming the H-VLPL3D hybrid code. We demonstrate its superior capabilities in wake field modeling, presenting various physical benchmarks.

This code was then used for the simulation of the self-modulated proton driven plasma wake field acceleration effect (SM-PDPWFA). Within this concept, a long proton bunch as delivered by the Super Proton Synchrotron (SPS) at CERN propagates through plasma. Small wake fields lead to self-modulation of the proton bunch; this causes strong longitudinal electric fields, which can be used for electron acceleration. We show that the phase velocity of the wake depends on, and is strongly connected to the growth rate of the self-modulation instability. Contrasting previous results on the phase velocity, we demonstrate that it rises during the non-linear stage, giving good conditions for electron injection. Using multi-staged simulations, the effectiveness of electron side injection into that wake is shown. Also, the wake phase velocity can be altered via background density gradients; with additional simulations, we demonstrate the significant change in phase velocity achieved by this method.

The detection of self-modulation and/or hosing of the proton bunch can be done using Coherent Transition Radiation. The problem of the total current not being altered by self-modulation is overcome by utilizing Transverse Coherent Transition Radiation (TCTR). We present approximate analytical descriptions for the radiated field, and illustrate the radiation patterns for both beam shapes.

Zusammenfassung

Das Hauptaugenmerk dieser Arbeit ist die Entwicklung, Implementierung und Anwendung von Hybridmodulen für den Particle-in-cell (PIC) Plasma - Simulationscode Virtual Laser Plasma Lab (VLPL). Der PIC/Fluid - Hybridansatz ermöglicht die Modellierung von Plasmen sowohl durch die bekannte PIC - Methode, als auch durch gitterbasierte Fluiddynamik.

Ausgehend von einem linearisierten Fluidmodell wurde in Zusammenarbeit mit dem Institut für angewandte Mathematik der HHU Düsseldorf ein Mollified Impulse-Löser, eine Variante eines exponentiellen Integrators entwickelt und implementiert. Er verwendet ein dreistufiges Push-Oscillate-Splitting-Schema sowie Filterfunktionen, um unphysikalische Resonanzen zu vermeiden. Der bedeutende Vorteil dieses Verfahrens liegt in der Tatsache, daß seine Stabilität nicht mehr von der Fluid-Plasmafrequenz abhängt; somit können Plasmen beliebig hoher Dichte simuliert werden. Nach der Implementierung in den existierenden VLPL - Code wurde das Modul erfolgreich mit Hilfe verschiedener physikalischer Beispiele getestet.

Ein weiteres, nicht-lineares Hybridschema wurde dann speziell für die Simulation extrem langer Plasma-Kielwellenfelder (Wake Fields) entwickelt. Dieses Modul verwendet primitive Fluidvariablen auf einem versetzten Gitter, um Interpolationsfehler zu vermeiden. Es wurde mit dem VLPL-Code zum H-VLPL3D - Hybridcode kombiniert. Seine bei der Kielwellenfeldmodellierung überlegenen Eigenschaften wurden danach an verschiedenen physikalischen Testproblemen nachgewiesen.

Dieser Code wurde dann bei der Simulation der Kielwellenfeldbeschleunigung durch selbstmodulierte Protonenstrahlen (self-modulated proton driven plasma wake field acceleration, SM-PDPWFA) eingesetzt. Bei diesem Mechanismus propagiert ein relativ langer Protonenbunch, wie er durch das Super Proton Synchrotron (SPS) am CERN erzeugt werden kann, durch ein Plasma. Plasmaoszillationen führen zur Selbstmodulation des bunches; dabei werden starke elektrische Felder angeregt, die für die Beschleunigung von Elektronen genutzt werden können. Durch Simulationen mit dem Code H-VLPL3D, sowie theoretische Modelle wurde nachgewiesen, dass die Phasengeschwindigkeit des Wake Fields von der Anstiegsrate der Selbstmodulationsinstabilität abhängt und stark mit ihr verknüpft ist. Im Gegensatz zu früheren Resultaten über diese Phasengeschwindigkeit konnte außerdem gezeigt werden, dass sie während des nichtlinearen Stadiums der Instabilität ansteigt. Das macht den SM-PDPWFA-Effekt im Hinblick auf eine spätere Elektroneninjektion vielversprechend. Mit Hilfe mehrstufiger Simulationen wurde die Effektivität seitlicher Injektion demonstriert. Weiterhin kann die Phasengeschwindigkeit gesteuert werden, indem die Dichte des Hintergrundplasmas leicht variiert wird; dieser Ansatz wurde mit zusätzlichen Simulationen untersucht.

Um die Strahl-Selbstmodulation und auch das sogenannte Hosing zu detektieren, kann der Effekt der kohärenten Übergangsstrahlung (Coherent Transition

Radiation, CTR) verwendet werden. Diese Strahlung entsteht, wenn der Teilchenpuls durch eine leitfähige Oberfläche tritt. Das bekannte Problem, dass sich der transversale Gesamtstrom durch die Selbstmodulation nicht ändert, wird durch die transversale kohärente Übergangsstrahlung (TCTR) umgangen. Für das abgestrahlte Feld wurde eine genäherte analytische Beschreibung angegeben, sowie mit H-VLPL3D-Simulationen verglichen.

Proofs for the FDTD method

LEMMA 5. *For a plane wave (3.5.1), the linear operator S of one FDTD Strang splitting step has the eigenvalues*

$$\lambda_S = [-2\sqrt{\alpha^4 - \alpha^2} - 2\alpha^2 + 1, 2\sqrt{\alpha^4 - \alpha^2} - 2\alpha^2 + 1, 1].$$

Substituting the field vector into (3.4.6) yields

$$\begin{aligned}
& \left(\hat{B}_x^{n+\frac{1}{2}} - \hat{B}_x^n\right) e^{I((i+\frac{1}{2})\Delta x k_x + j\Delta y k_y + k\Delta z k_z)} \\
= \quad & -\frac{\Delta t}{2\Delta y}\left(\hat{E}_z^n e^{I((i+\frac{1}{2})\Delta x k_x + (j+\frac{1}{2})\Delta y k_y + k\Delta z k_z)} - \hat{E}_z^n e^{I((i+\frac{1}{2})\Delta x k_x + (j-\frac{1}{2})\Delta y k_y + k\Delta z k_z)}\right) \\
& +\frac{\Delta t}{2\Delta z}\left(\hat{E}_y^n e^{I((i+\frac{1}{2})\Delta x k_x + j\Delta y k_y + (k+\frac{1}{2})\Delta z k_z)} - \hat{E}_y^n e^{I((i+\frac{1}{2})\Delta x k_x + j\Delta y k_y + (k-\frac{1}{2})\Delta z k_z)}\right) \\
= \quad & -e^{I\mathbf{k}\cdot\mathbf{r}_{i+\frac{1}{2},j,k}} \frac{\Delta t}{2\Delta y}\left(\hat{E}_z^n e^{\frac{1}{2}I\Delta y k_y} - \hat{E}_z^n e^{-\frac{1}{2}I\Delta y k_y}\right) \\
& +e^{I\mathbf{k}\cdot\mathbf{r}_{i+\frac{1}{2},j,k}} \frac{\Delta t}{2\Delta z}\left(\hat{E}_y^n e^{\frac{1}{2}I\Delta z k_k} - \hat{E}_y^n e^{\frac{1}{2}I\Delta z k_k}\right) \\
\Rightarrow & \\
\hat{B}_x^{n+\frac{1}{2}} \quad = \quad & \hat{B}_x^n - \frac{\Delta t}{2\Delta y}\hat{E}_z^n e^{-I\mathbf{k}\cdot}\left(\hat{E}_z^n e^{\frac{1}{2}I\Delta y k_y} - \hat{E}_z^n e^{-\frac{1}{2}I\Delta y k_y}\right) \\
& +\frac{\Delta t}{2\Delta z}\left(\hat{E}_y^n e^{\frac{1}{2}I\Delta z k_z} - \hat{E}_y^n e^{-\frac{1}{2}I\Delta z k_z}\right) \\
= \quad & \hat{B}_x^n - I\sin(\frac{1}{2}\Delta y k_y)\frac{\Delta t}{\Delta y}\hat{E}_z^n + I\sin(\frac{1}{2}\Delta z k_z)\frac{\Delta t}{\Delta z}\hat{E}_y^n,
\end{aligned}$$

where I denotes the imaginary constant.
Likewise, we have

$$\hat{E}_x^{n+1} = \hat{E}_x^n + 2I\sin(\frac{1}{2}\Delta y k_y)\frac{\Delta t}{\Delta y}\hat{B}_z^{n+\frac{1}{2}} - 2I\sin(\frac{1}{2}\Delta z k_z)\frac{\Delta t}{\Delta z}\hat{B}_y^{n+\frac{1}{2}}.$$

Results for the other components are similarly obtained, with cyclically permuted indices. We notice that the substeps of S turns a plane wave with wave vector $\mathbf{k}$ into another plane wave with the same wave vector, but changed coefficients. This means that S can be block-diagonalized this way, making the remaining problem six-dimensional instead of $6n_x n_y n_z$D.

For simplification, we define the quantities $\lambda_x := \Delta t/\Delta x$, $\xi_x := k_x\Delta x$, $\alpha_x := \lambda_x \sin(\frac{\xi_x}{2})$, and $\alpha_y, \alpha_z, \lambda_y ...$ analogously.

Then we have

$$
\begin{aligned}
\hat{B}_x^{n+\frac{1}{2}} &= \hat{B}_x^n - I\sin(\frac{1}{2}\Delta y k_y)\frac{\Delta t}{\Delta y}\hat{E}_z^n + I\sin(\frac{1}{2}\Delta z k_z)\frac{\Delta t}{\Delta z}\hat{E}_y^n \\
&= \hat{B}_x^n - I\alpha_y\hat{E}_z^n + I\alpha_z\hat{E}_y^n \qquad (.0.1) \\
\hat{E}_x^{n+1} &= \hat{E}_x^n + 2I\sin(\frac{1}{2}\Delta y k_y)\frac{\Delta t}{\Delta y}\hat{B}_z^{n+\frac{1}{2}} - 2I\sin(\frac{1}{2}\Delta z k_z)\frac{\Delta t}{\Delta z}\hat{B}_y^{n+\frac{1}{2}} \\
&= \hat{E}_x^n + 2I\sin(\frac{1}{2}\Delta y k_y)\frac{\Delta t}{\Delta y}\left(\hat{B}_z^n - I\sin(\frac{1}{2}\Delta x k_x)\frac{\Delta t}{\Delta x}\hat{E}_y^n + I\sin(\frac{1}{2}\Delta y k_y)\frac{\Delta t}{\Delta y}\hat{E}_x^n\right) \\
&- 2I\sin(\frac{1}{2}\Delta z k_z)\frac{\Delta t}{\Delta z}\left(\hat{B}_y^n - I\sin(\frac{1}{2}\Delta z k_z)\frac{\Delta t}{\Delta z}\hat{E}_x^n + I\sin(\frac{1}{2}\Delta x k_x)\frac{\Delta t}{\Delta x}\hat{E}_z^n\right) \\
&= \hat{E}_x^n + 2I\alpha_y\hat{B}_z^n + 2\alpha_x\alpha_y\hat{E}_y^n - 2\alpha_y^2\hat{E}_x^n - 2I\alpha_z\hat{B}_y^n - 2\alpha_z^2\hat{E}_x^n + 2\alpha_z\alpha_x\hat{E}_z^n \\
&= \left(1 - 2(\alpha_z^2+\alpha_y^2)\right)\hat{E}_x^n + 2I\alpha_y\hat{B}_z^n + 2\alpha_x\alpha_y\hat{E}_y^n - 2I\alpha_z\hat{B}_y^n + 2\alpha_z\alpha_x\hat{E}_z^n \qquad (.0.2)
\end{aligned}
$$

$$
\begin{aligned}
\hat{B}_x^{n+1} &= \hat{B}_x^{n+\frac{1}{2}} - I\sin(\frac{1}{2}\Delta y k_y)\frac{\Delta t}{\Delta y}\hat{E}_z^{n+1} + I\sin(\frac{1}{2}\Delta z k_z)\frac{\Delta t}{\Delta z}\hat{E}_y^{n+1} \\
&= \hat{B}_x^n - I\alpha_y\hat{E}_z^n + I\alpha_z\hat{E}_y^n \\
&- I\alpha_y\left[\left(1 - 2(\alpha_y^2+\alpha_x^2)\right)\hat{E}_z^n + 2I\alpha_x\hat{B}_y^n + 2\alpha_z\alpha_x\hat{E}_x^n - 2I\alpha_y\hat{B}_x^n + 2\alpha_y\alpha_z\hat{E}_y^n\right] \\
&+ I\alpha_z\left[\left(1 - 2(\alpha_x^2+\alpha_z^2)\right)\hat{E}_y^n + 2I\alpha_z\hat{B}_x^n + 2\alpha_y\alpha_z\hat{E}_z^n - 2I\alpha_x\hat{B}_z^n + 2\alpha_x\alpha_y\hat{E}_x^n\right] \\
&= \hat{B}_x^n\left(1 - 2(\alpha_y^2+\alpha_z^2)\right) + 2\alpha_x\alpha_y\hat{B}_y^n + 2\alpha_z\alpha_x\hat{B}_z^n \\
&+ I\alpha_y\left(-2 + 2\alpha_y^2 + 2\alpha_x^2 + 2\alpha_z^2\right)\hat{E}_z^n + I\alpha_z\left(2 - 2(\alpha_x^2+\alpha_y^2+\alpha_z^2)\right)\hat{E}_y^n. \qquad (.0.3)
\end{aligned}
$$

The effect of S on the plane wave can then be expressed as

$$
\begin{bmatrix} \hat{E}_x^{n+1} \\ \hat{E}_y^{n+1} \\ \hat{E}_z^{n+1} \\ \hat{B}_x^{n+1} \\ \hat{B}_y^{n+1} \\ \hat{B}_z^{n+1} \end{bmatrix} = \hat{S} \begin{bmatrix} \hat{E}_x^n \\ \hat{E}_y^n \\ \hat{E}_z^n \\ \hat{B}_x^n \\ \hat{B}_y^n \\ \hat{B}_z^n \end{bmatrix}, \qquad (.0.4)
$$

with

$$
\hat{S} := \begin{bmatrix} \hat{S}_{EE} & \hat{S}_{EB} \\ \hat{S}_{BE} & \hat{S}_{BB} \end{bmatrix}
$$

$$\hat{S}_{EE} := \begin{bmatrix} 1-2\left(\alpha_z^2+\alpha_y^2\right) & 2\,\alpha_x\,\alpha_y & 2\,\alpha_x\,\alpha_z \\ 2\,\alpha_x\,\alpha_y & 1-2\left(\alpha_z^2+\alpha_x^2\right) & 2\,\alpha_y\,\alpha_z \\ 2\,\alpha_x\,\alpha_z & 2\,\alpha_y\,\alpha_z & 1-2\left(\alpha_y^2+\alpha_x^2\right) \end{bmatrix}$$

$$\hat{S}_{EB} := \begin{bmatrix} 0 & -2\,i\,\alpha_z & 2\,i\,\alpha_y \\ 2\,i\,\alpha_z & 0 & -2\,i\,\alpha_x \\ -2\,i\,\alpha_y & 2\,i\,\alpha_x & 0 \end{bmatrix}$$

$$\hat{S}_{BE} := \begin{bmatrix} 0 & 2\,i\,\alpha_z\left(1-\alpha^2\right) & -2\,i\,\alpha_y\left(1-\alpha^2\right) \\ -2\,i\,\alpha_z\left(1-\alpha^2\right) & 0 & 2\,i\,\alpha_x\left(1-\alpha^2\right) \\ 2\,i\,\alpha_y\left(1-\alpha^2\right) & -2\,i\,\alpha_x\left(1-\alpha^2\right) & 0 \end{bmatrix}$$

$$\hat{S}_{BB} := \begin{bmatrix} 1-2\left(\alpha_z^2+\alpha_y^2\right) & 2\,\alpha_x\,\alpha_y & 2\,\alpha_x\,\alpha_z \\ 2\,\alpha_x\,\alpha_y & 1-2\left(\alpha_z^2+\alpha_x^2\right) & 2\,\alpha_y\,\alpha_z \\ 2\,\alpha_x\,\alpha_z & 2\,\alpha_y\,\alpha_z & 1-2\left(\alpha_y^2+\alpha_x^2\right) \end{bmatrix},$$

where $\alpha^2 := \alpha_z^2+\alpha_y^2+\alpha_x^2$.

Computing the eigenvalues of $\hat{S}$, one obtains

$$\begin{aligned}\lambda_s =(&1,\\ &-2\sqrt{\alpha_z^4+\left(2\,\alpha_y^2+2\,\alpha_x^2-1\right)\,\alpha_z^2+\alpha_y^4+\left(2\,\alpha_x^2-1\right)\,\alpha_y^2+\alpha_x^4-\alpha_x^2}-2\,\alpha_z^2-2\,\alpha_y^2-2\,\alpha_x^2+1,\\ &2\sqrt{\alpha_z^4+\left(2\,\alpha_y^2+2\,\alpha_x^2-1\right)\,\alpha_z^2+\alpha_y^4+\left(2\,\alpha_x^2-1\right)\,\alpha_y^2+\alpha_x^4-\alpha_x^2}-2\,\alpha_z^2-2\,\alpha_y^2-2\,\alpha_x^2+1)\end{aligned}$$

with multiplicity 2 for each $\lambda_{S,i}$. We get

$$\lambda_S = [-2\sqrt{\alpha^4-\alpha^2}-2\,\alpha^2+1, 2\sqrt{\alpha^4-\alpha^2}-2\,\alpha^2+1, 1].$$

Bibliography

[1] T. Tajima and J. Dawson. Laser electron accelerator. *Physical Review Letters*, 43(4):267–270, July 1979.

[2] Ian Blumenfeld, Christopher E. Clayton, Franz-Josef Decker, Mark J. Hogan, Chengkun Huang, Rasmus Ischebeck, Richard Iverson, Chandrashekhar Joshi, Thomas Katsouleas, Neil Kirby, Wei Lu, Kenneth A. Marsh, Warren B. Mori, Patric Muggli, Erdem Oz, Robert H. Siemann, Dieter Walz, and Miaomiao Zhou. Energy doubling of 42 GeV electrons in a metre-scale plasma wakefield accelerator. *Nature*, 445(7129):741–744, February 2007.

[3] A. Caldwell, K. Lotov, A. Pukhov, et al. Proton-driven plasma-wakefield acceleration. *Nature Physics*, 5(5):363–367, April 2009.

[4] E. Esarey, P. Sprangle, J. Krall, et al. Overview of plasma-based accelerator concepts. *IEEE Transactions on Plasma Science*, 24(2):252–288, April 1996.

[5] E. Esarey, C. Schroeder, and W. Leemans. Physics of laser-driven plasma-based electron accelerators. *Reviews of Modern Physics*, 81:1229–1285, August 2009.

[6] J. Faure, Y. Glinec, A. Pukhov, S. Kiselev, S. Gordienko, E. Lefebvre, J.-P. Rousseau, F. Burgy, and V. Malka. A laser–plasma accelerator producing monoenergetic electron beams. *Nature*, 431(7008):541–544, September 2004.

[7] C. G. R. Geddes, C. Toth, J. van Tilborg, et al. High-quality electron beams from a laser wakefield accelerator using plasma-channel guiding. *Nature*, 431(7008):538–541, September 2004.

[8] C. Joshi. Plasma accelerators. *Scientific American*, 294(2):40–47, February 2006.

[9] C. Joshi and V. Malka. Focus on laser- and beam-driven plasma accelerators. *New Journal of Physics*, 12:045003, April 2010.

[10] C. Joshi, B. Blue, C. E. Clayton, et al. High energy density plasma science with an ultrarelativistic electron beam. *Physics of Plasmas*, 9(5):1845, 2002.

[11] A. Pukhov and J. Meyer-ter Vehn. Laser wake field acceleration: the highly non-linear broken-wave regime. *Applied Physics B: Lasers and Optics*, 74(4-5):355–361, April 2002.

[12] S. P. D. Mangles, C. D. Murphy, Z. Najmudin, et al. Monoenergetic beams of relativistic electrons from intense laser–plasma interactions. *Nature*, 431(7008):535–538, September 2004.

[13] W. P. Leemans, B. Nagler, A. J. Gonsalves, et al. GeV electron beams from a centimetre-scale accelerator. *Nature Physics*, 2(10):696–699, September 2006.

[14] S. Kneip, S. Nagel, S. Martins, et al. Near-GeV acceleration of electrons by a nonlinear plasma wave driven by a self-guided laser pulse. *Physical Review Letters*, 103(3), July 2009.

[15] D. Strickland and G. Mourou. Compression of amplified chirped optical pulses. *Optics Communications*, 56(3):219–221, 1985.

[16] F. Amiranoff, S. Baton, D. Bernard, et al. Observation of laser wakefield acceleration of electrons. *Physical Review Letters*, 81(5):995–998, August 1998.

[17] P. Chen, A. Spitkovsky, T. Katsouleas, et al. Transformer ratio and pulse shaping in laser wakefield accelerator. *Nuclear Instruments and Methods in Physics Research Section A: Accelerators, Spectrometers, Detectors and Associated Equipment*, 410(3):488–492, June 1998.

[18] K. L. F. Bane, P. Chen, and P. B. Wilson. On collinear wake field acceleration. *IEEE Transactions on Nuclear Science*, 32(5):3524–3526, 1985.

[19] A. Pukhov, N. Kumar, T. Tückmantel, et al. Phase velocity and particle injection in a self-modulated proton-driven plasma wakefield accelerator. *Physical Review Letters*, 107(14):145003, September 2011.

[20] K. V. Lotov. Simulation of proton driven plasma wakefield acceleration. *Physical Review Special Topics - Accelerators and Beams*, 13(4), April 2010.

[21] E. Esarey, J. Krall, and P. Sprangle. Envelope analysis of intense laser pulse self-modulation in plasmas. *Physical Review Letters*, 72(18):2887–2890, 1994.

[22] N. Kumar, A. Pukhov, and K. Lotov. Self-modulation instability of a long proton bunch in plasmas. *Physical Review Letters*, 104, June 2010.

[23] C. Schroeder, C. Benedetti, E. Esarey, et al. Growth and phase velocity of self-modulated beam-driven plasma waves. *Physical Review Letters*, 107(14), September 2011.

[24] A. Caldwell, K. Lotov, A. Pukhov, et al. Plasma wakefield excitation with a 24 GeV proton beam. *Plasma Physics and Controlled Fusion*, 53(1):014003, January 2011.

[25] C. K. Birdsall and A. B. Langdon. *Plasma physics via computer simulation*. McGraw-Hill, New York, 1985.

[26] R. W. Hockney and J. W. Eastwood. *Computer simulation using particles*. A. Hilger, Bristol [England]; Philadelphia, 1988.

[27] R. A. Fonseca, L. O. Silva, F. S. Tsung, et al. OSIRIS: a three-dimensional, fully relativistic particle in cell code for modeling plasma based accelerators. In Peter M. A. Sloot, Alfons G. Hoekstra, C. J. Kenneth Tan, and Jack J. Dongarra, editors, *Computational Science — ICCS 2002*, volume 2331, page 342–351. Springer Berlin Heidelberg, Berlin, Heidelberg, 2002.

[28] J. Verboncoeur. An object-oriented electromagnetic PIC code. *Computer Physics Communications*, 87(1-2):199–211, May 1995.

[29] D. P. Grote, A. Friedman, I. Haber, et al. Three-dimensional simulations of high current beams in induction accelerators with WARP3d. *Fusion Engineering and Design*, 32-33:193–200, November 1996.

[30] C. Nieter. VORPAL: a versatile plasma simulation code. *Journal of Computational Physics*, 196(2):448–473, May 2004.

[31] D. Welch, D. Rose, R. Clark, et al. Implementation of an non-iterative implicit electromagnetic field solver for dense plasma simulation. *Computer Physics Communications*, 164(1-3):183–188, December 2004.

[32] A. Pukhov. Three-dimensional electromagnetic relativistic particle-in-cell code VLPL (Virtual laser plasma lab). *Journal of Plasma Physics*, 61(3):425–433, April 1999.

[33] P. Janardhan, S. Kamath, V. L. Christie, et al. 3-dimensional particle-in-cell modeling of a shadow-gridded electron gun. page 2. IEEE.

[34] L. Gargate, R. Bingham, R. Fonseca, et al. dHybrid: a massively parallel code for hybrid simulations of space plasmas. *Computer Physics Communications*, 176(6):419–425, March 2007.

[35] J. Liljo, A. Karmakar, A. Pukhov, et al. One-dimensional electromagnetic relativistic PIC-hydrodynamic hybrid simulation code h-VLPL (hybrid virtual laser plasma lab). *Computer Physics Communications*, 179(6):371–379, September 2008.

[36] S. C. Wilks, A. B. Langdon, T. E. Cowan, et al. Energetic proton generation in ultra-intense laser–solid interactions. *Physics of Plasmas*, 8(2):542, 2001.

[37] H. Mayer and R. Krechetnikov. Walking with coffee: Why does it spill? *Physical Review E*, 85(4), April 2012.

[38] W. L. Kruer. *The Physics Of Laser Plasma Interactions (Frontiers in Physics)*. Westview Press, 2003.

[39] S. Augst, D. D. Meyerhofer, D. Strickland, et al. Laser ionization of noble gases by coulomb-barrier suppression. *Journal of the Optical Society of America B*, 8(4):858, April 1991.

[40] G. Mainfray and G. Manus. Multiphoton ionization of atoms. *Reports on Progress in Physics*, 54(10):1333–1372, October 1991.

[41] B. Van Leer. Towards the ultimate conservative difference scheme. IV. a new approach to numerical convection. *Journal of Computational Physics*, 23(3):276–299, 1977.

[42] A. Kurganov and E. Tadmor. New high-resolution central schemes for nonlinear conservation laws and Convection–Diffusion equations. *Journal of Computational Physics*, 160(1):241–282, 2000.

[43] H. Nessyahu and E. Tadmor. Non-oscillatory central differencing for hyperbolic conservation laws. *Journal of Computational Physics*, 87(2):408–463, 1990.

[44] S. Zalesak. Fully multidimensional flux-corrected transport algorithms for fluids. *Journal of Computational Physics*, 31(3):335–362, 1979.

[45] P. Colella and P. Woodward. The piecewise parabolic method (PPM) for gas-dynamical simulations1. *Journal of Computational Physics*, 54(1):174–201, 1984.

[46] E. Sonnendrücker, J. Roche, P. Bertrand, et al. The semi-lagrangian method for the numerical resolution of the vlasov equation. *Journal of Computational Physics*, 149(2):201–220, 1999.

[47] K. Yee. Numerical solution of initial boundary value problems involving maxwell's equations in isotropic media. *IEEE Transactions on Antennas and Propagation*, 14(3):302–307, 1966.

[48] E. Hairer, C. Lubich, and G. Wanner. *Geometric numerical integration : structure-preserving algorithms for ordinary differential equations*. Springer, Berlin, 2006.

[49] A. Taflove and S. C. Hagness. *Computational electrodynamics : the finite-difference time-domain method*. Artech House, Boston, 2005.

[50] J. P. Boris. Relativistic plasma simulation-optimization of a hybrid code. *Proceedings of the 4th Conference on Numerical Simulation of Plasmas. Naval Res. Lab.*, page 3–67, 1970.

[51] G. H. Golub and C. F. Van Loan. *Matrix computations*. Johns Hopkins University Press, Baltimore, 1996.

[52] J. Villasenor and O. Buneman. Rigorous charge conservation for local electromagnetic field solvers. *Computer Physics Communications*, 69(2-3):306–316, March 1992.

[53] C.C.-P. Chen, Tae-Woo Lee, N. Murugesan, and S.C. Hagness. Generalized FDTD-ADI: an unconditionally stable full-wave maxwell's equations solver for VLSI interconnect modeling. page 156–163. IEEE.

[54] Jean-Pierre Berenger. A perfectly matched layer for the absorption of electromagnetic waves. *Journal of Computational Physics*, 114(2):185–200, October 1994.

[55] J. A. Roden and S. D. Gedney. Convolution PML (CPML): an efficient FDTD implementation of the CFS-PML for arbitrary media. *Microwave and Optical Technology Letters*, 27(5):334–339, December 2000.

[56] D. an der Brügge and A. Pukhov. Ultrashort focused electromagnetic pulses. *Physical Review E*, 79(1), January 2009.

[57] E. F. Toro. *Riemann solvers and numerical methods for fluid dynamics a practical introduction*. Springer-Verlag, Berlin; New York, 1999.

[58] P. Wesseling. *Principles of computational fluid dynamics*. Springer, Berlin; Heidelberg; New York [etc.], 2001.

[59] M. Tabak, J. Hammer, M. E. Glinsky, et al. Ignition and high gain with ultrapowerful lasers. *Physics of Plasmas*, 1(5):1626, 1994.

[60] D. an der Brügge, N. Kumar, A. Pukhov, et al. Influence of surface waves on plasma high-order harmonic generation. *Physical Review Letters*, 108(12), March 2012.

[61] P. W. Rambo and J. Denavit. Fluid and field algorithms for time-implicit plasma simulation. *Journal of Computational Physics*, 92(1):185–212, January 1991.

[62] P. W. Rambo and J. Denavit. Interpenetration and ion separation in colliding plasmas. *Physics of Plasmas*, 1(12):4050, 1994.

[63] F. Zheng and Z. Chen. Numerical dispersion analysis of the unconditionally stable 3-d ADI-FDTD method. *IEEE Transactions on Microwave Theory and Techniques*, 49(5):1006–1009, 2001.

[64] M. Hochbruck and C. Lubich. A gautschi-type method for oscillatory second-order differential equations. *Numerische Mathematik*, 83(3):403–426, September 1999.

[65] M. Hochbruck and A. Ostermann. Exponential integrators. *Acta Numerica*, 19:209–286, May 2010.

[66] V. Grimm and M. Hochbruck. Error analysis of exponential integrators for oscillatory second-order differential equations. *Journal of Physics A: Mathematical and General*, 39(19):5495–5507, May 2006.

[67] B. Garcia-Archilla, J. M. Sanz-Serna, and R. D. Skeel. Long-time-step methods for oscillatory differential equations. *SIAM Journal on Scientific Computing*, 20(3):930, 1998.

[68] J. Liljo. *Hybride Verfahren zur Simulation der Wechselwirkung relativistischer Kurzpuls-Laser mit hochdichten Plasmen*. PhD thesis, Heinrich-Heine-Universität Düsseldorf.

[69] M. Tuckerman, B. J. Berne, and G. J. Martyna. Reversible multiple time scale molecular dynamics. *The Journal of Chemical Physics*, 97(3):1990, 1992.

[70] H. Grubmüller, H. Heller, A. Windemuth, et al. Generalized verlet algorithm for efficient molecular dynamics simulations with long-range interactions. *Molecular Simulation*, 6(1-3):121–142, March 1991.

[71] J. J. Biesiadecki and R. D. Skeel. Dangers of multiple time step methods. *Journal of Computational Physics*, 109(2):318–328, December 1993.

[72] E. Weibel. Spontaneously growing transverse waves in a plasma due to an anisotropic velocity distribution. *Physical Review Letters*, 2(3):83–84, February 1959.

[73] T. Tückmantel, A. Pukhov, J. Liljo, et al. Three-dimensional relativistic particle-in-cell hybrid code based on an exponential integrator. *IEEE Transactions on Plasma Science*, 38(9):2383–2389, September 2010.

[74] B. P. Leonard. A stable and accurate convective modelling procedure based on quadratic upstream. (19):59–98, 1979.

[75] R. L. Dougherty, A. S. Edelman, and J. M. Hyman. Nonnegativity-, monotonicity-, or convexity-preserving cubic and quintic hermite interpolation. *Mathematics of Computation*, 52(186):471–471, May 1989.

[76] N. E. Andreev, V. I. Kirsanov, L. M. Gorbunov, et al. Linear theory of resonance self-modulation of an intense laser pulse in homogeneous plasma and plasma channels. *IEEE Transactions on Plasma Science*, 24(2):363–369, April 1996.

[77] A. Bers. *Basic plasma physics 1*. North-Holland Publishing Company, 1983.

[78] D. Whittum, W. Sharp, S. Yu, et al. Electron-hose instability in the ion-focused regime. *Physical Review Letters*, 67(8):991–994, August 1991.

[79] S. Y. Kalmykov, L. M. Gorbunov, P. Mora, et al. Injection, trapping, and acceleration of electrons in a three-dimensional nonlinear laser wakefield. *Physics of Plasmas*, 13(11):113102, 2006.

[80] A. Pukhov. Control of laser-wakefield acceleration by the plasma-density profile. *Physical Review E*, 77(2), February 2008.

[81] J. Rosenzweig, G. Travish, and A. Tremaine. Coherent transition radiation diagnosis of electron beam microbunching. *Nuclear Instruments and Methods in Physics Research Section A: Accelerators, Spectrometers, Detectors and Associated Equipment*, 365(1):255–259, November 1995.

[82] U. Happek, A. Sievers, and E. Blum. Observation of coherent transition radiation. *Physical Review Letters*, 67(21):2962–2965, November 1991.

[83] Hung-chi Lihn, Pamela Kung, Chitrlada Settakorn, Helmut Wiedemann, and David Bocek. Measurement of subpicosecond electron pulses. *Physical Review E*, 53(6):6413–6418, June 1996.

[84] R. Lai and A. Sievers. Phase problem associated with the determination of the longitudinal shape of a charged particle bunch from its coherent far-ir spectrum. *Physical Review E*, 52(4):4576–4579, 1995.

[85] Y. Shibata, T. Takahashi, T. Kanai, et al. Diagnostics of an electron beam of a linear accelerator using coherent transition radiation. *Physical Review E*, 50(2):1479–1484, August 1994.

[86] W. Leemans, C. Geddes, J. Faure, et al. Observation of terahertz emission from a laser-plasma accelerated electron bunch crossing a plasma-vacuum boundary. *Physical Review Letters*, 91(7), August 2003.

[87] C. Schroeder, E. Esarey, J. van Tilborg, et al. Theory of coherent transition radiation generated at a plasma-vacuum interface. *Physical Review E*, 69(1), January 2004.

[88] J. van Tilborg, C. Schroeder, C. Filip, et al. Temporal characterization of femtosecond laser-plasma-accelerated electron bunches using terahertz radiation. *Physical Review Letters*, 96(1), January 2006.

[89] L. D. Landau and E. M. Lifshits. *The classical theory of fields*. Butterworth Heinemann, Oxford; Boston, 2000.

Danksagung

Mag auf dem Deckblatt der fertiggestellten Dissertation auch nur ein einziger Name stehen, so wäre diese Arbeit dennoch nicht möglich gewesen ohne die Unterstützung, Hilfe und Kooperation einer großen Zahl von Personen, bei denen ich mich hiermit herzlich bedanken möchte.

Mein besonderer Dank gilt meinem Betreuer Prof. Dr. Alexander Pukhov. Er hatte stets ein offenes Ohr für meine Fragen, stellte seinen Code VLPL und seine Rechnercluster zur Verfügung, gab mir Anleitung und Ratschläge und ermöglichte die Arbeit an seinem Institut.

Ich danke Prof. Dr. Marlis Hochbruck (KIT Karlsruhe) für die gute Zusammenarbeit bei der Entwicklung des in Kapitel 5 vorgestellten Simulationsmoduls und für hilfreiche Diskussionen.

Bei Prof. Dr. Achim Schädle bedanke ich mich für das zweite Gutachten und die Hilfe bei diversen numerischen Fragen.

Außerdem danke ich Prof. Dr. Carsten Müller und Prof. Dr. (i.R.) Karl-Heinz Spatschek, den Leitern des Instituts für Plasmaphysik, für die Gelegenheit, an ihrem Lehrstuhl promovieren zu dürfen.

Ich danke Jalo Liljo und Georg Jansing für die interessante Kooperation; weiterhin Naveen Kumar für analytische Modelle und vor allem seine sympathische und motivierende Art.

Unser Systemadministrator Eugen Bleile sorgte während meiner Promotion stets für funktionierende Computer - ich danke ihm sehr für seine schnelle Hilfe bei Problemen. Unserer Sekretärin Elvira Gröters danke ich für ihre Hilfbereitschaft und freundliche Unterstützung beim schwersten Teil jeder wissenschaftlichen Arbeit (Reiseabrechnungen und sonstige Formulare).

Dankbar ist, wer die Gelegenheit hatte, in einem Institut mit so vielen interessanten, netten und lustigen Menschen zu arbeiten: Oliver Jansen, Daniel an der Brügge, Sebastian Münster, Götz Lehmann, Tongpu Yu, Johannes Thomas, Christoph Karle, Ajit Upadhyay, Anupam Karmakar, Eckehard Zügge, Matthias Dellweg, Min Chen, Alexej Snytnikov, Friedrich Schluck (und alle weiteren, die ich möglicherweise vergessen habe) waren immer angenehme Kollegen für mich.

Allen meinen Freunden, sowohl den Wuppertaler Niveaumetallern als auch allen anderen, möchte ich herzlich danken für die Hilfe, die sie mir durch schieres Ertragen meines promotionsspezifischen Geklages leisteten. Dem Schicksal im Allgemeinen danke ich für meine bezaubernde Freundin Constanze, die mich durch meine Promotion begleitet hat, und für die wunderbare gemeinsame Zeit.

Ein besonderer Dank gilt meinen Eltern Barbara und Erwin Tückmantel, ohne deren Rückhalt und unendliche Unterstützung ein Physikstudium und eine Promotion kaum möglich gewesen wären; außerdem meiner lieben Großmutter Hannelore Vesper, die meine Arbeit mit großer Geduld verfolgte.

Erklärung

Hiermit erkläre ich, die vorliegende Dissertation selbstständig verfaßt, keine anderen als die vorliegenden Quellen und Hilfsmittel benutzt, sowie Zitate kenntlich gemacht zu haben.

Düsseldorf, den